Nano Electro Mechanical Systems and Interactions at the nanoscale

Alessandro Siria

UNIVERSITÉ JOSEPH FOURIER - GRENOBLE

THESE

pour obtenir le titre de

DOCTEUR DE L'UNIVERSITÉ JOSEPH FOURIER (Ph.D.)

IN PHYSIQUE

preparée au *Centre National de la Recherche Scientifique (CNRS)*
et au *Commisariat Energie Atomique (CEA)*

presenté par

Alessandro Siria

Systemes Nano Electro Mechanique et Interactions à l'échelle nanomètrique

Jury de these:

President:	Prof. Frank Hekking
Rapporteur:	Prof. Elisabeth Charlaix
Rapporteur:	Prof. Davide Iannuzzi
	Prof. Khaled Karrai
	Dr. Laurent Duraffourg
Directeur:	Prof. Joël Chevrier
Co-directeur:	Mr. Hubert Grange

UNIVERSITÉ JOSEPH FOURIER - GRENOBLE

THESIS

for obtaining the degree of

DOCTEUR OF UNIVERSITÉ JOSEPH FOURIER (Ph.D.)

IN PHYSICS

prepared at the *Centre National de la Recherche Scientifique (CNRS)* and the *Commisariat Energie Atomique (CEA)*

presented ad sat by

Alessandro Siria

Nano Electro Mechanical Systems and Interactions at the nanoscale

Jury de these:

President:	Prof. Frank Hekking
Referee:	Prof. Elisabeth Charlaix
Referee:	Prof. Davide Iannuzzi
	Prof. Khaled Karrai
	Dr. Laurent Duraffourg
Advisor:	Prof. Joël Chevrier
Co-advisor:	Mr. Hubert Grange

Acknowledgements

This thesis work presents measurements of interaction phenomena acting at the nanoscale. The goal of this thesis was the comprehension of the physics governing Nano Electro Mechanical Systems (NEMS).
The laboratories directly involved in this thesis work are the CNRS-Institut Néel and CEA/LETI/DIHS/LCMS in Grenoble.
I would like to thank the directors of these two laboratories, Alain Fontaine and Philippe Robert, for the great opportunity they gave to me.
A particular acknowledgement is for Serge Huant, director of the *Equipe Champ Proche* at the Institut Néel, group where I have been working as PhD student. His constant support has been foundamental for the achievement of the results here presented.
In this section, I cannot forget Fabio Comin director of the Surface Science Laboratory (SSL) at the European Synchrotron Radiation Facility (ESRF). All the measurements presented have been performed at the SSL. I thank him for his help during these three years.

I would like to thank Khaled Karrai for having accepted to be part of this commitee. I thank as well Elisabeth Charlaix and Davide Iannuzzi for the important and hard work of referee that they have accepted to accomplish. I have to thank also Frank Hekking and Laurent Duraffourg for being part of this commitee.

The thesis advisor, Joël Chevrier, deserves a special aknowledgement. Before helping me to achieve the experimental results discussed in this report, along the three year he helped me to find my way to be young "scientist". His positive attitude during the bad periods (and during a thesis there are too many bad periods) has been crucial to go on untill the end of the thesis. Sometimes I was thinking to never achieve the results, but he was always confident about what i can do. I really appreciate him as advisor even if he was not always on time for the meeting...
I would like to thank Hubert Grange, my co-advisor. During these three

years he was always ready to help me. The Nano Electro Mechanical Systems to analyzed have been developed at the CEA/LETI and Hubert has been foundamental to enter me in the complex burocracy of the CEA. I thank Hubert for all the time he spent to explain me the details about the sample characteristic and their realization process. I would like to thank him also for all the encouragements and support during this work.

During a thesis the bad periods seams to be more than the good ones. During those momentents you can easily think to be alone. I thank Wilfrid Shwartz to have shared with me not only the good days but also the bad ones. I never felt to be alone in the lab.
With Emmanuel Rousseau, I shared some very good moments when, after intense two weeks (almost without stop...), we finally measured a clear near-field contribution in the radiative heat transfer. I would say that Emmanuel shared with only good moments but it is not completely true. I would really thank him for the *one shot* measurement we have performed together.
The list of the persons to remember in this particular section is still long and I fear to forget someone.
Here I cannot miss to thank Guillaume Jourdan. He was Phd student in the group before me and his work has been a reference during all my thesis. Moreover I inherited the experimental set-up he developed for the measurement of the Casimir force. For this reason I would like to thank him twice!
Pascal Dideron cannot be forgotten too. All the experimental set-up components have been *created* by his hands. He was always ready to spend some time for me even when he was busy.

With Antoine and Aurelien C. I spent some very nice periods at conferences, during the every day meals and during the evenings. They have been perfect PhD mates. A thesis is a three year period and being with good friends in the lab is important. I have to thank them for this.
Mario is impossible to forget. This crazy portugues guy was always ready to say that I was wrong. Actually sometimes I was right but other times I was really wrong and for his particular way to help me I have to thank him.
Michal "Buga" Hrouzek was in the lab when I arrived and he is there now that I'm finishing my thesis. He has been a very good mate in the lab. I really enjoyed to speak with him about technical issues and I enjoyed as well the time we spent together outside the lab, trying to climb in the mountains around Grenoble.
I want to thank all the people who was with me during the thesis, at the Institut Néel, CEA or ESRF: Olivier Dhez, Florence Marchi, Nicolas Venant, Julien Lopez, Michele Manfredda, Hua Gao, J-F. Motte, Aurelien Drezet,

Alexis Mosset, Herman Sellier, Sebastien Labarthe, Justine Laurent, Pierre Mallet, Fanny Hiebel, Roberto Felici, Didier Wermeille, Monique Navizet, Irina Snigireva, Isabelle Combe, Philippe Andreucci, Bruno Raig, Valerie Nguyen, Eric Ollier, Sebastien Hentz, Nevine Rochat and Geoffroy Auvert (I am very sorry if I am missing someone!).
A major contribution for this thesis come from a group that is not involved with the science world. I am speaking about all the friends I met at the Ju-Jitsu here in Grenoble. I thank Jacques, Laurent, Thierry, Greg, Cedric, Vincent, Vanessa, Philippe, Denis, Laurent, Olivier and all the others at the Dojo in Sassenage.
A big "thank you" is for the friends in Genova and here in Grenoble:
Alessandro, "magister", and Elf, they have been very nice and kind with me; they were ready to come here in Grenoble to have fun together. They have been always with me when I came back home during holidays;
Giorgio and Giulia to have been always honest with me and to have found time to spent with me all the times I went back in Genova;
G. to have been my mate in all the stupid and dangerous things I have done...
Giovanni and Luca for all the good dinners, for biking and climbing together here in Grenoble;
Carlotta... ok maybe You should thank me again for the 4 month you spent here!!
Mini, Pippo, Patty, Teo, Ilaria, Dani C., Dani M. and Dani G., Enri and all the other friends in Genova;
Gauthier, Ben, Elie, Pierre, Miguel, Camille, Nicolas D., Nicolas P. Helene, Mathilde, Laurent *etc., etc., etc.* for the good time in Grenoble.
A very particular acknowledgement is for Simon and Lise. They have been very good friends here in Grenoble from the very beginning of this experience. Without them the permanence in Grenoble would have been hard. I thank them very much for the good times we spent together.
Finally I thank "Cuiche"; she came with me from Genova and since I am here in Grenoble she has been with me and she has supported me every day.

Contents

List of Figures

Systèmes Nano Électro Mécaniques et interactions à l'échele nanomètrique

Les Systèmes Nano et Micro Électro Mécaniques intègrent des fonctionalités électrique et mécanique à l'échelle nano- et micrométriques. Même si on peut imaginer les MEMS et NEMS comme des machine miniatures trés soophistiqués, elles sont aujourd'hui de simples oscillateurs mécaniques.
Le comportement de ces oscillateurs dépend de leur environnement de travail. Si ils fonctionnent dans le vide et/ou à température cryogénique, leur propriétés dynamiques différent sensiblement par rapport à leur fonctionnement à température et pression ambiante. Si ces oscillateurs vibrent proche d'un échantillon, l'apparition des forces d'interaction entre l'échantillon et les oscillateurs, induit un changement des paramétres caractéristiques d'oscillation.
L'utilisation de ces structures est aujourd'hui largement répandue et couvre nombre d'applications différentes, allant de la topographie de surface ou analyse chimique à la mesure des forces d'interaction à l'échelle nanométrique.
Malgré la variété des formes complexes des MEMS et NEMS, ils partagent tous le même schéma de base. Une partie mobile est suspendue au dessus d'un substrat par une série de ressorts. Dans une configuration standard, la partie mobile et le substrat sont dans une géométrie plan.
La partie mobile oscille autour de sa position d'équilibre avec une fréquence de résonance propre donnée par sa masse et la raideur des ressorts. L'écart entre la partie mobile et le substrat peut varier entre dix nanomètres et quelques microns. Lorsque cet écart est inférieur au micron, le comportement du système mécanique est dominé par les forces d'interactions entre le substrat et la partie mobile.
La compréhension des forces d'interaction à l'échelle nanométrique est cruciale pour le fonctionnement et le développement des NEMS.
Poursuivant le travail de Gauthier Torricelli et de Guillaume Jourdan, dans cette thèse nous traitons les interactions entre surfaces lorsque l'écart en-

tre elles est de l'ordre de dix nanomètres à quelques microns. Toutes les expériences présentées ici ont été réalisées soit dans le vide soit dans l'air; nous ne traiterons pas le problème des interaction en liquide.
Dans le chapitre 2, nous analyserons l'amortissement d'un micro-oscillateur lorsqu'il est graduellemnt approché d'un substrat dans une géométrie plan-plan. Nous étudierons le comportement du système mécanique en fonction de la distance de confinement montrant ainsi que l'amortissement effectif, due à l'air, dépend de cette distance. Une explication du comportement observé peut être obtenue en résolvant l'équation de Navier-Stokes.
Dans le chapitre 3 nous nous pencherons sur l'effet de la lumiére synchrotron agissant sur un NEMS. Nous montrerons comment l'interaction entre le faisceau de rayons X et le système mécanique peut potentiellement ouvrir une nouvelle famille d'outils pour la manipulation de rayons X.
La radiation thermique entre une surface plane et une sphère micrométrique sera le sujet du chapitre 4. Après avoir présenté le traitement électromagnétique de la radiation thermique, nous comparerons les résultats expérimentaux avec le modèle théorique.
En conclusion, nous introduirons le probèlme des mesures de forces en géométrie plan-plan.

Chapter 1

Interactions at nanoscale

Contents

1.1 Micro and Nano Electromechanical Systems (MEMS and NEMS)

Micro and Nano Electro Mechanical Systems are devices integrating electrical and mechanical functionalities at the micro- and nanoscale. Even though we can imagine MEMS or NEMS as very sophisticate miniaturized machine, today they are usually simple mechanical oscillators.
The behavior of such oscillators depends on the environment they work into. If the oscillators are working in vacuum and/or cryogenic temperature, their dynamical properties slightly differ from those at ambient temperature and pressure. If the oscillators are vibrating close to a sample, the arising interaction forces between the sample and the oscillators, induce a change in the oscillation characteristic parameters of the system.
The use of these structures is nowadays widespread and it covers a number of different applications, ranging from the surface topography or chemical analysis to measurement of interaction forces at the nanoscale [1, 2, 3, 4, 5, 6, 7, 8]. The real power of this emerging technology is that many of such devices can be built at the same time across the surface of a wafer without any required

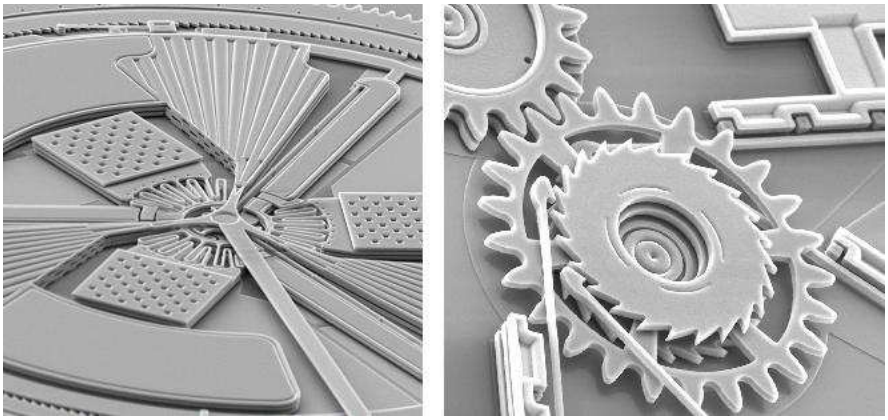

Figure 1.1: SEM image of Micro Electro Mechanical Systems.

assembly procedure. Since the production process is like a photographic process, it is just as easy to build a million of system on the wafer as it would be to build one. This is clearly a very interesting aspect for microelectronic applications that require the repetition of the same action a huge amount of time.
We see how these system can be realized. Microsystems involve dimensions that vary from 1 to 100 μm, while nanosystems involve dimensions that varies from 1 to 100 nm.
Usually MEMS and NEMS are made on Silicon since it is standardly used in microelectronic manufacturing process. From a flat wafer of single crystal silicon the systems are realized through chemical processes.

Photolitography

Lithography in MEMS context is typically the transfer of a pattern into a photosensitive material by selective exposure to a radiation source such as light.
If a photosensitive material is selectively exposed to radiation (e.g. by masking some of the radiation) the pattern of the radiation on the material is transferred to the material exposed, as the properties of the exposed and unexposed regions differs.
The wafer is covered with photo resist by spin coating, to produce a uniformly thick layer between 0.5 and 2.5 micrometres thick. The spin coating process results in a uniform thin layer, usually with uniformity of within 5 to 10 nanometres. This uniformity can be explained by detailed fluid-mechanical modeling, which shows that essentially the resist moves much faster at the top of the layer than at the bottom, where viscous forces bind the resist to

the wafer surface. The top resist is then removed by the spinning, while the bottom resist stays on the surface.
The photoresist is then exposed to a pattern of intense light. Optical lithography typically uses ultraviolet light. Positive photoresist, the most common type, becomes soluble in the basic (chemical) developer when exposed; negative photoresist becomes insoluble in the developer. The use of developers removes a part of the resist allowing to realize a mask with the suitable geometry.
The wafer covered with the resist mask is then chemically etched.

Etching

Etching is used in micro- and nanofabrication to remove layers from the surface of a wafer during manufacturing, using a chemical etcher.
If the etch is intended to make a cavity in a material, the depth of the cavity may be controlled approximately using the etching time and the known etching rate. More often etching must entirely remove the top layer of a multilayer structure without damaging the underlying or masking layers. The effectivness of the process depends on the ratio of etching rates in the two materials.
Some etches undercut the masking layer and form cavities with sloping sidewalls. The undercutting distance is called bias. Etchants with large bias are called isotropic, because they erode the substrate equally in all directions. Modern processes prefer anisotropic etches, since they produce sharp, well-controlled features.
There are two basic categories of etching processes: wet and dry etching. In the former, the material is dissolved when immersed in a chemical solution. In the latter, the material is sputtered or dissolved using reactive ions or a vapor phase etchant.

Wet etching
Wet chemical etching consists in a selective removal of material by dipping a substrate into a solution that can dissolve it. Since the chemical nature of the etching process, it is possible to choose the etching solution so that the etching rate of the target material is considerably higher than that of the mask material. This turns into a good selectivity.
Wet etchants are usually isotropic, which leads to large bias when etching thick films. However some wet etchants etch crystalline materials at very different rates depending upon which crystal face is exposed. In single-crystal materials (e.g. silicon wafers), this effect can allow very high anisotropy.
Dry etching

A good alternative to the wet etching is the so-called dry etching which involves plasma etchers instead of liquid ones. Normally the dry etching is performed in vacuum, and it mainly consists in etcher ions impinging on the wafer surface with suitable angle and energy. Since impinging ions is highly directionale, the dry etching is extremely anisotropic.
The biggest advantage compared with the wet etching is the lack of toxic waste, making the dry etching suitable for the preparation of very large scale systems.

Surface micromachining

A typical Surface Micromachining process is a repetitive sequence made up of depositing thin films on a wafer, photopatterning the films, and then etching the patterns into the films. In order to create movable parts, structural layers (typically silicon) are alterned with sacrificial layers (typically silicon dioxide). The structural material will form the mechanical elements, and the sacrificial material creates the gaps and spaces between the mechanical elements. At the end of the process, the sacrificial material is removed and the structural elements are let to freely move and function.
For the case of the structural level being silicon, and the sacrificial material being silicon dioxide, the final *release* process is performed by placing the wafer in Hydrofluoric Acid. The Hydrofluoric Acid quickly etches away the silicon dioxide, leaving the silicon undisturbed.
The wafers are typically then sawn into individual chips, which are packaged in an appropriate manner for the given application.

1.2 Interactions between surfaces at nanoscale

Despite the variety of complicated shapes MEMS and NEMS might come in, they all share a common underlying schema, presented in figure 1.2. A mobile part is suspended over a substrate thanks to a series of restoring springs. In a standard configuration both mobile part and substrate are in plane geometry.
The mobile part oscillates around the equilibrium position with a typical resonance frequency given by the mass of the mobile part and the stiffness of the restoring springs.
The gap between the mobile part and the substrate can vary from tens of nanometers up to several micrometers. When the gap is in the sub-micron range the interaction forces between the substrate and the mobile part can dominate the behavior of the mechanical systems. The comprehension of the

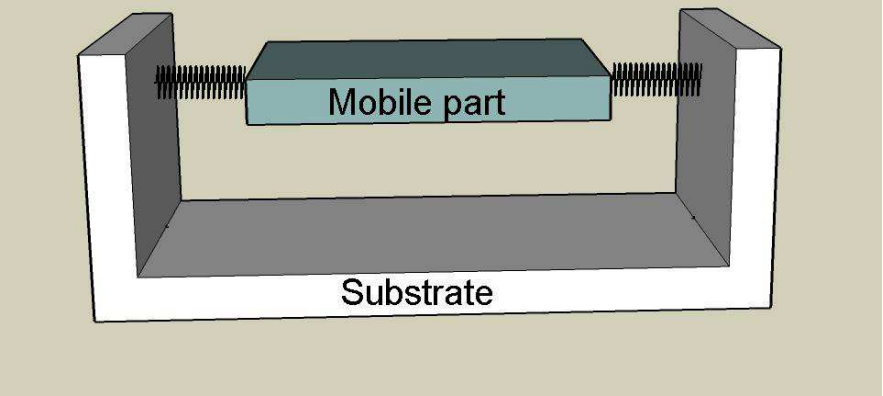

Figure 1.2: Schema of Micro and Nano Electro Mechanical Systems.

interaction forces at the nanoscale is crucial for the functioning and further development of Nano Electro Mechanical Systems.
The interactions between the surfaces that can play a major role in the NEMS functioning are:

Van der Waals and Casimir forces

Van der Waals force (VdW) originates from transient dipoles created between molecules without any permanent bi-pole moment. Transient dipoles result in uneven distribution of electrons around a nucleus, which result in a weak positive charge on one side of the molecule and a negative one on the other side. This transient behavior occurs in all molecules of given object. If two materials are brought in close proximity it results as an attractive force between these two objects. Van der Waals force appears between all neutral atoms and molecules independent on this kind. This force typically extend up to the tens nanometers of distance.
When the distance between two objects increases the retardation effect due the finite speed of light has to be taken into account in the formulation of the Van der Waals force.
Such a retarded force names after the Dutch scientist H. Casimir, who first described it. In his first formulation, Casimir related the retarded force to the quantum fluctuation of the electromagnetic field inside the cavity formed between the two surfaces. In particular, Casimir (1948) calculated the attractive force between two ideal mirrors in vacuum. Since then, this effect has attracted much interest in many areas such as micro- and nano mechanical systems, quantum field theory and gravitation. With up-to-date technique in force measurements at sub-micron scale, the Casimir force has

been precisely measured [9, 10, 11, 12, 13].
In this thesis work we are interested in gap ranges where the VdW force are negligible compared to other interaction forces.
The precise measurement of the Casimir force has been subject of the thesis of Gauthier Torricelli [9] and Guillaume Jourdan [10]. They have performed measurements between two gold surfaces in a sphere-plane geometry.

Chemical forces

The atomic bonds hold together by sharing or exchanging electrons. Strong chemical bonds are found in molecules, crystals or in solid metals and they organize the atoms in ordered structures. Weak chemical bonds are classically explained to be consequence of polarity between molecules which contain strong polar bonds.
The molecular bonding between flat surfaces, based on chemical forces, found important industrial application. The Silicon On Insulator (SOI) technique realizes wafer for microtechnology using the strong interaction forces due to the chemical interactions between a flat surface of Silicon and a flat surface of Silicon Oxide.
In this thesis work we are interested in gap ranges where the chemical forces are negligible compared to other interaction forces.

Electrostatic forces

When a voltage difference is applied to two approached surfaces, an attractive force is applied to the surfaces, due to the electrostatic field. This force depends by the geometry and the materials in analysis.
Even if the applied voltage difference is zero, when two objects are approached at close separations, the electrostatic forces arising from trapped charges and patch potentials at the surfaces give rise to forces that can easily dominate the interaction.
The precise measurement of the electrostatic forces has been subject of the thesis of Gauthier Torricelli [9] and Guillaume Jourdan [10]. They have performed measurements between two gold surfaces in a sphere-plane geometry.

Magnetic forces

Magnetic forces arise when the probe and the sample are based on magnetic material. The interaction between the magnetic dipoles generates a force acting on the micro cantilever. This kind of technique can be extremely sensible to the measurement of magnetic dipole and allowes the measurement the spin of a single electron [2].

This kind of interaction forces have not been subject of analysis in this thesis work. Interesting experimental studies can be found in [1, 2].

Hydrodynamic forces

When the mechanical system oscillates in a viscous environment its dynamical behavior is modified by fluid resistance. If the oscillator is closed to a surface the behavior of the fluid is modified by its confinement, which results in the modification of the system mechanical properties.
The way the oscillator is consequently affected, depends by the particular boundary conditions for the fluid at the solid-fluid interface.
The hydrodynamic forces can mediate the interaction between two approached surfaces if the cavity gap is smaller then the hydrodynamic characteristic length scale, which depends on the fluid viscosity and on the dynamical properties of the oscillator. For Micro and Nano Electro Mechanical Systems working in air, this characteristic length scale can be up to several tens of micrometers.
This kind of interaction forces will be the subject of chapter 2. We will analyze the damping of a micro-oscillator as it is gradually approached to a substrate, in a plane-plane geometry. We will study the evolution of the mechanical system behavior as a function of the confinement gap showing that the effective damping, due to the air, is depending on the gap size. An explanation of the observed behavior will be obtained solving the Navier-Stokes equations for the case in analysis.

Optical forces

Considering the schema of the NEMS presented in figure 1.2, from an optical point of view the system is like a Fabry-Perot cavity, being its properties determined by reflection and transmission coefficients of the two boundary surfaces. Optical forces can be then applied to the two surfaces; they may originate radiation pressure effect or thermal switch effect acting on the materials [14, 15, 16, 17, 18, 19, 20].
The effect of optical forces has been addressed also in the thesis of Guillaume Jourdan [10]. In particular he has studied the optical cooling of a microlever induced by a laser beam.
In chapter 3 we will address the effect of synchrotron light acting on a mechanical system. The biggest advantage of using X-ray beam is the possibility to be completely quantitative in the analysis since the radiation-matter interaction at X-wavelenghts is well described in literature. We will show how the interaction X-ray with the mechanical system can potentially offer a new

family of tools for the X-ray beam manipulation. We will show how a X-ray chopper can be realized coupling the mechanical and optical properties of a silicon cantilever, offering the possibility to shape and tune an X-ray beam wave-front.

Near field thermal radiation

The thermal transfer at micro- and nanoscale does not follow the textbook law for the energy transfer. When two surfaces are kept at sub-micron separation, in fact, the contribution of the near field components, which can be neglected for larger gaps, gives rise to important contributions that cannot be neglected. Although the presence of this near field component has been already experimentally verified, a comparison between the theory and the experience is still lacking.
The thermal radiation between a plane surface and a micrometric sphere will be the subject of chapter 4. After having presented the electromagnetic treatment of the thermal radiation, we will show a comparison between the experimental results and the theoretical model.

Following the work of Gauthier Torricelli [9] and Guillaume Jourdan [10], in this thesis work we will address the physical interactions between surfaces when the gap is in the range from tens of nanometers up to several micrometers. The working condition of all the experiments here shown will be vacuum or air; we will not address the problem of interactions in liquid.

1.3 Towards a reliable measurement of plane-plane interaction forces

In the gap range studied in this thesis work the interaction forces that can dominate the behavior of a NEMS are: hydrodynamic forces, electrostatic forces, near-field thermal radiation and Casimir forces. In the standard plane-plane geometry we can define the dependency of the interactions on the distance.

- Hydrodynamic force (perfect slip boundary conditions):

$$F = -\gamma \cdot v = -\frac{2\eta A v}{d} \Rightarrow \; F \to 1/d; \tag{1.1}$$

  (see page 30) Chapter 2
  Characteristic length given by fluid layer around oscillator: $d_c \approx 20\ \mu m$ determines an upper limit for the behavior in (1.1)

- Electrostatic force between two conductors:

$$F = -\frac{1}{2}\frac{\varepsilon V^2 A}{d^2} \Rightarrow \; F \to 1/d^2; \tag{1.2}$$

No characteristic length as expected for unscreened electrostatic interaction.

- Radiative heat transfer between dielectric materials:

$$\phi \to 1/d^2; \tag{1.3}$$

(see page 74) Chapter 4
Characteristic length given by radiation wavelength: $d_c \approx 1\ \mu m$ at $T = 300\ K$

- Hydrodynamic force (no slip boundary conditions):

$$F = -\gamma \cdot v = -\frac{\eta w L^3}{d^3} \Rightarrow \; F \to 1/d^3; \tag{1.4}$$

(see page 28) Chapter 2
Characteristic length given by fluid layer around oscillator: $d_c \approx 20\ \mu m$ determines an upper limit for the behavior in (1.4)

- Casimir force between two perfect mirrors (dielectric constant $\epsilon = -\infty$):

$$F = \frac{\hbar c \pi^2 A}{240 d^4} \Rightarrow \; F \to 1/d^4. \tag{1.5}$$

Characteristic length given by plasmon wavelength: $d_c \approx 150\ nm$
Casimir regime holds in the limit $d >> d_c$, VdW regime holds in the limit $d << d_c$

Although the plane-plane geometry is the easiest configuration for the theoretical description, from an experimental point of view a measurement of interaction forces is very hard.
All the interaction forces listed above are depending on the gap between the two surfaces. If the two surfaces are not perfectly parallel, the misalignment can modify the measured interaction. This is more delicate, stronger is the dependency on the distance.
This is precisely the reason why Gauthier Torricelli and Guillaume Jourdan, together with scientists of other groups [11, 12, 13], have performed measurement in a sphere-plane geometry, since in this case the problem of the parallelism is removed.

Working in the sphere-plane geometry induces two major issues. First of all, the exact theory for the interaction forces is usually developed for the plane-plane geometry. The treatment of a sphere-plane configuration is based on the Derjaguin approximation [21], also called Proximity Force Approximation (PFA). In this approximation the sphere is modeled as a series of infinitesimal planes parallel to the second plane surface. The total interaction force is calculated as the summation of forces between infinitesimal planes and the plane surface.
In sphere-plane geometry the problem of the parallelism is removed; but the one of the surface roughness is introduced. In fact, if, thanks to the lithography and etching processes, it is possible to obtain a plane surface with a nanomete sized roughness, this is not possible for micrometric spheres. The average roughness for a micrometric sphere is in the order of tens of nanometers. To be able to perform a reliable plane-plane interactions measurement is a real challenge.
In this thesis we will enter the problem of plane-plane geometry. We will show how it is possible to measure the hydrodynamic forces (with perfect slip boundary conditions) in the demanding plane-plane geometry, thanks to the weak dependency of the interaction on the distance (chapter 2). In the case of hydrodynamic forces studied the dependecy of the force is like the inverse of the gap size. The experimental set-up developed has not the possibility to tune the misalignement angle between the surfaces. However a static set-up can allow an alignement better then 1 deg. We will se that this will be enough for a precise measurement of this interaction force.
We performed measurement of radiative heat transfer between two surfaces in the sphere-plane geometry, providing a very precise measurement of energy transfer at nanoscale (chapter 4).
We have tried a measurement of near-field thermal radiation in the plane-plane geometry with a full dedicated experimental set-up (chapter 5). As we will discuss in chapter 5, for a reliable measurement of the radiative heat transfer in the demanding plane-plane geometry a parallelism much better than 0.1 deg is needed. In this case a static set-up cannot achieve such a precision and a tuning of the misalignement angle has to be implemented. We will propose then a new experimental set-up based on micro-goniometers able to control the angle with a precision of $\approx 10^{-4}$ deg.
All the other interaction forces listed above presents a dependency on the distance that is equal to, or stronger than the radiative heat transfer. A static experimental set-up is then not enough for a measurement in the plane-plane geometry. The experimental set-up that we propose will be shown to be accurate enough to allow measurements also for the strongest dependency force, the Casimir force .

Micro-oscillator dans un fluide simple

Un simple levier oscillant est l'exemple le plus représentatif de MEMS ou NEMS. En effet les micro et nano-leviers ont été utilisés dans de nombreuses études fondamentales ou applicatives. Parmi les résultats les plus spectaculaires obtenus avec ces leviers oscillants, on trouve la mesure de masse à l'échelle du zeptogramme, la mesure de force à l'échelle sub-atonewton et le refroidissement optique d'un oscillateur. Ces résultats se basent sur l'extraordinaire facteur de qualité des leviers fonctionnant dans le vide ou à température cryogénique. Le comportement de ces systèmes est différent si ils fonctionnent dans l'air ou en liquide à cause de la dissipation dans le fluide lui-même. Dans ce chapitre on décrira la dynamique d'un micro-oscillateur dans l'air, on montrera que le confinement du fluide change le couplage avec le bain thermique autant en terme de fluctuation que de dissipation. On verra que le confinement peut sensiblement modifié le comportement du levier et éventuellement supprimer l'oscillation mécanique

Chapter 2

Micro Electro Mechanical System in a simple fluid

Contents

2.1 Introduction

The most representative example of Micro or Nano Electro Mechanical Systems (MEMS or NEMS) is a simple tiny oscillating silicon cantilever. Indeed micro- and nano-scale mechanical levers are used as sensors and actuators in a large variety of fundamental studies and applications. Mass detection at the zeptogram scale [3, 4, 5], sub-attonewton force detection [1, 2, 6, 7, 8] and optical cooling of microlevers [14, 15, 16, 17, 18, 19] are among the most spectacular achievements of oscillating cantilevers (CLs). These realizations mainly rely upon the extraordinary high quality (Q) factors of oscillating

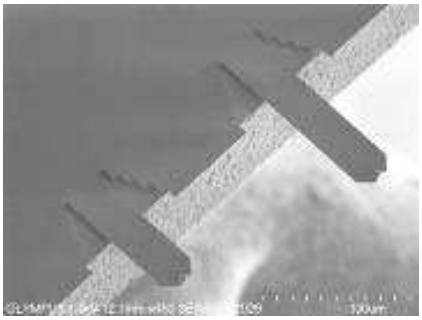

Figure 2.1: SEM image of AFM cantilevers for liquid imaging (from Biosensor web-site).

CLs in vacuum and/or cryogenic temperatures where values exceeding 100 000 are attainable.
The behavior of these systems is different if they are working in air or liquid, since the damping in the surrounding fluid dramatically degrades the quality factor. This has been partially circumvented by using ultrasmall self-sensing nano-electromechanical systems actuated mechanical devices made from submicron mechanical components facing each other operating in ambient conditions of temperature and pressure [22].
Oscillating CLs are used in viscous environments on many occasions [23, 24, 25, 26]. In Atomic Force Microscopy (AFM) for example, a resonant CL is used to measure surface topography and physico-chemical properties of various materials not only in air [27] but also in liquids for, *e.g.*, identifying the supramolecular assemblies and functional conformation of native membrane proteins in biological specimens [27, 28].
The interaction between an AFM CL and a surrounding liquid has been used for a distance calibration in a Casimir force measurement [29, 30] and has led very recently to the spectacular demonstration of a repulsive Casimir force [31].
In this chapter we describe the dynamics of a micro-oscillator in a simple fluid, the air. When a CL beam vibrates in a viscous fluid, the fluid offers resistance to the beam displacement [32, 33]. If the CL is vibrating close to a solid surface, the behavior of the fluid and, consequently, that of the lever are modified by the surface due to confinement. The Navier-Stokes (NS) equation gives a complete description of the fluid behavior taking into account the particular environment under analysis. However an analytical solution of the NS equation is possible only for a restricted number of geometries and comparison of theory with experimentally relevant configurations is in general a complex matter or is even lacking, especially at the deep micron and

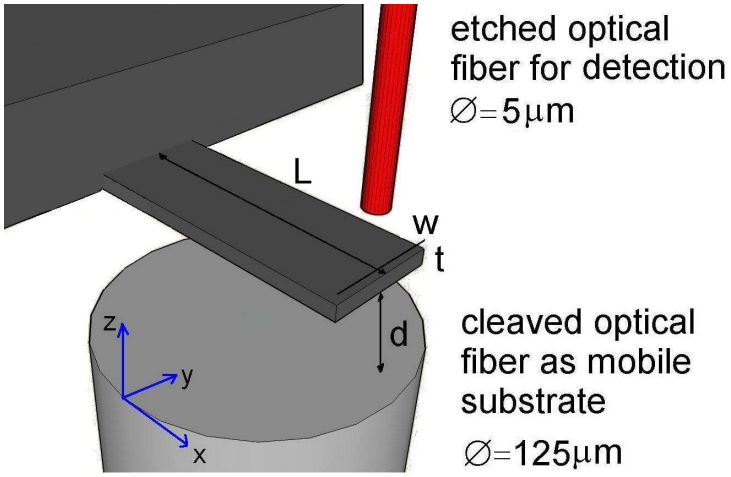

Figure 2.2: Scheme of the experimental setup (not to scale). The analyzed mechanical system is a standard AFM CL. A cleaved optical fiber (bottom) is used as mobile substrate forming a cavity with the CL. An etched optical fiber (top) is used for the interferometric detection of the CL Brownian motion. The main geometrical parameters used in the text are identified, the z origin is taken on the flat cleaved-fiber surface.

submicron scales [34, 35, 36, 37, 38, 39, 40, 41]. We focus on the dynamical behavior of a microlever close to a planar rigid surface in the air. The NS equation can be solved analytically for this plane-plane model geometry that mimics a basic part of a MEMS device operating in the air.
We will show how the confinement of the fluid changes the coupling to thermal bath, both in terms of fluctuation and dissipation and how this can significantly modify the lever behavior and eventually freeze out the mechanical oscillation.

2.2 Experimental set-up

The experimental setup developed for the study of the micro lever dynamics in a simple fluid is shown schematically in Fig. 2.2.
The cantilever is a thin silicon AFM CL for liquid imaging with dimensions $L \times w \times t = 107 \times 30 \times 0.18\ \mu m^3$ with $\approx 30\ nm$ of gold coating (see AFM cantilever presented in fig. 2.1). The tip has been removed using a Focus Ion Beam. The lever is not externally driven but is actuated by the stochastic thermal noise only. This induces sub-Angstrom oscillations at the CL resonance frequency ($\approx 50\ kHz$). Here we are interested in the effect of the geometry on the damping of the oscillator and in particular on the fluid

confinement effect. A planar rigid surface facing the CL forming a parallel-plate cavity is then approached to the lever. This second surface is made of a cleaved optical fiber with a diameter of 125 μm that is mounted over a three-axis inertial motor so as to be able to *adjust the cavity gap*. This positioning system offers a large displacement range (8 mm each axis full range) with a good accuracy (40 nm per step). The advantage of using a cleaved optical fiber as movable plate is that it is possible to inject a laser beam into it for the purpose of calibrating with high accuracy (better than 1 nm) its displacement towards the CL. This was extracted from the evolution of the interference pattern formed between the cleaved fiber end and the CL (see section 2.2.1). Finally, the CL motion is measured by means of a *non invasive* interferometric detection based on the use of a very thin optical fiber facing the CL at a 2 μm distance. This fiber has been chemically etched so as to reduce its diameter to 5 μm. This corresponds basically to the fiber core diameter plus a residual amount of the optical cladding for better light guidance. The large ratio in excess of 600 between the areas of the cleaved and detection fibers insures that only the cleaved one induces air confinement, not the etched one, which is used for detection purpose only. Therefore, no additional uncontrolled confinement and damping are produced by the detection fiber.

2.2.1 Fiber optics based interferometer

The cantilever position, and consequently its displacement, has been measured using a fibered optical interferometer. In figure 2.3 the device is schematically presented.
The main components are a stabilized laser source, a beam coupler for the injection of the laser in the optical fiber, a beam divider, called *Coupler X*, working as a cube separator, and a photodiode to convert the optical signal in an electric one.
Analyzing the experimental configuration as shown in figure 2.3, a laser beam is injected in a Silicon optic fiber. The laser beam passes through the coupler X and it arrives to extremity P_0. A part is reflected (S1 beam in the inset) by the fiber end while the other part reaches the lever surface before to be reflected back into the fiber (S2 beam in the inset).
The two beams together pass again through the coupler X to get finally the photodiode. The intensity detected at the level of the photodiode is modulated by the path difference of the beam S1 and S2 equal to $2d$, where d is the distance between the fiber end and the lever surface.
Considering the reflection coefficient of the interface silicon oxide-air ($\approx$ 4%), with good accuracy we can consider that the photodiode detect a two weaves

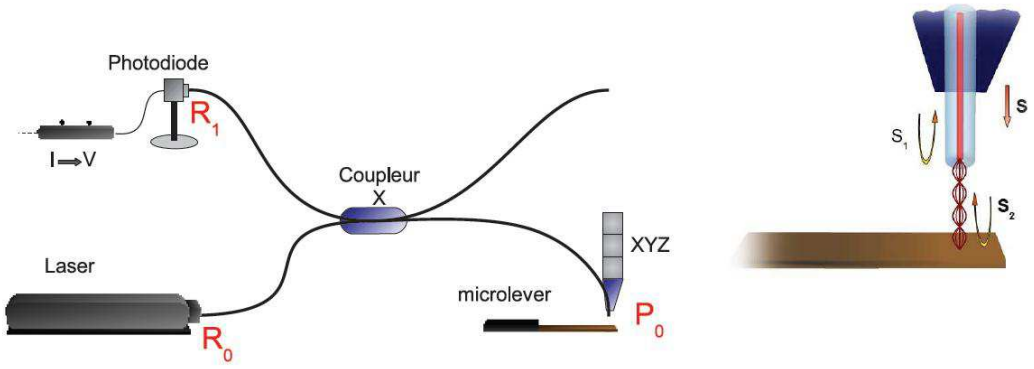

Figure 2.3: Schema of the optical interferometer (Courtesy of Guillaume Jourdan)

interference pattern:

$$I(d) = I_0 + \Delta I_0 \sin\left(\frac{4\pi}{\lambda}d + \phi\right) \tag{2.1}$$

where $\lambda = 635\ nm$ is the laser wavelength. The cantilever displacement δd is translated in a variation of intensity δI detected by the photodiode. The maximum of the sensibility is obtained for a set-point d_0 so that the measured intensity is equal to I_0, corresponding to the flex of the sinusoid (fig. 2.4). In first approximation the conversion factor between δd and δI is given by the first order development of the equation for the intensity:

$$\delta d = \frac{\lambda}{4\pi\Delta I_0}\delta I \tag{2.2}$$

2.3 Cantilever Dynamics

An AFM CL vibrating in a viscous fluid may be viewed as a driven and damped 1D harmonic oscillator (fig. 2.5) whose equation of motion reads

$$m\ddot{z}(t) + \gamma\dot{z}(t) + k_{lev}z(t) = F_{ext} \tag{2.3}$$

(m, $z(t)$, k_{lev} are the CL effective mass, time-dependent position, and stiffness, respectively, γ is the damping factor and F_{ext} the external driving force). If the cantilever is driven by a periodic external force $F_{ext}(t) = F_{ext}e^{i\omega_{ext}t}$, the solution of equation 2.3 has a form $z(t) = \hat{z}e^{i\omega_{ext}t}$ that reads:

$$\left[(i\omega_{ext})^2\,\hat{z} + i\omega_{ext}\frac{\gamma}{m}\hat{z} + \omega_0\hat{z}\right]e^{i\omega_{ext}t} = \frac{F_{ext}}{m}e^{i\omega_{ext}t} \tag{2.4}$$

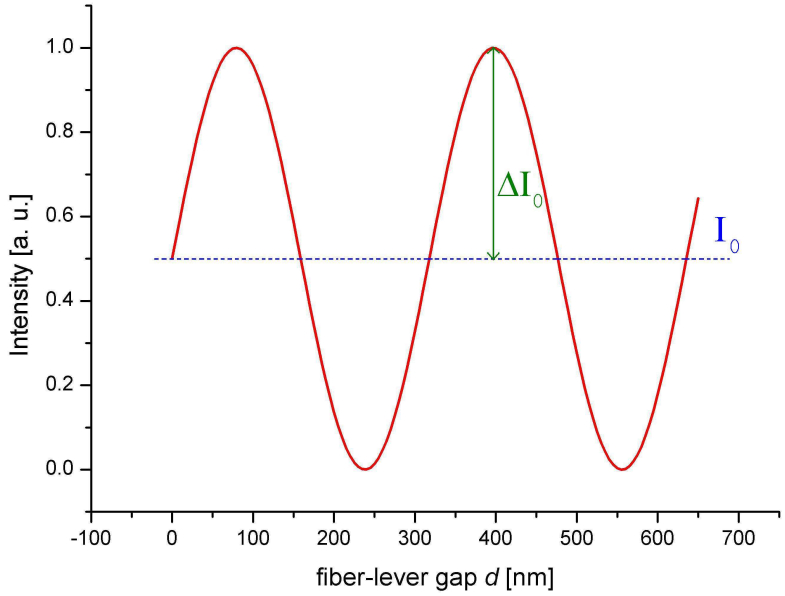

Figure 2.4: Optical interferometer response as function of the gap between the lever and the fiber end.

so that

$$\hat{z} = \frac{F_{ext}}{m(\omega_0^2 - \omega_{ext}^2) + i\gamma\omega_{ext}} = \chi(\omega_{ext}) \cdot F_{ext} \tag{2.5}$$

where $\omega_0 = 2\pi f_0 = \sqrt{\frac{k}{m}}$ is the CL natural frequency and

$$\chi(\omega) = \frac{1}{m(\omega_0^2 - \omega^2) + i\gamma\omega} \tag{2.6}$$

the cantilever transfer function. This shows that, if the driving force has a form $F_{ext}(t) = F_{ext} \cdot \cos(\omega_{ext}t)$, the movement of the cantilever is

$$z(t) = z_0 \cos(\omega_{ext}t) + \phi) \tag{2.7}$$

where z_0 is the vibration amplitude ad ϕ is the phase shift to the driving signal in the settle state of the oscillator. The vibration amplitude z_0 can be written as

$$z_0 = \frac{F_{ext}}{\sqrt{m^2(\omega_0^2 - \omega_{ext}^2)^2 + \gamma^2\omega_{ext}^2}} \tag{2.8}$$

and the phase shift

$$\phi = arctan\left(\frac{\gamma\omega_{ext}}{m(\omega_0^2 - \omega_{ext}^2)}\right). \tag{2.9}$$

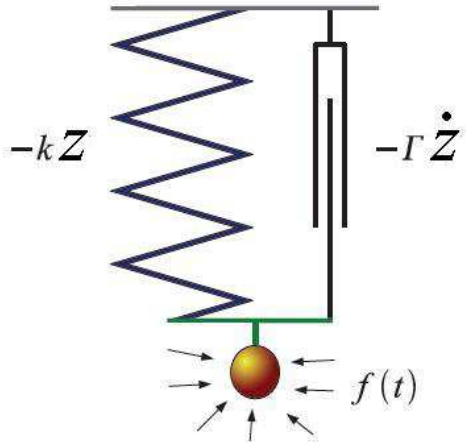

Figure 2.5: The driven damped harmonic oscillator represented as a mechanical system with spring k and a damping γ

The amplitude and phase diagrams for such a driven damped oscillator are shown in figure 2.6.
The oscillator has a resonance for a frequency

$$\omega' = \sqrt{\omega_0^2 - \frac{1}{2}\left(\frac{\gamma}{m}\right)^2} \tag{2.10}$$

that for the limit of small damping, *i.e.* $\frac{\gamma}{m} << \omega_0$, coincides with the CL natural frequency ω_0.
The model here presented describes the cantilever as a single mode oscillator where only the first and most significant harmonic mode has been taken into account. This model is actually very useful in describing the behavior of a CL working around the first resonance frequency, as done during this thesis. However to describe the cantilever behavior as accurately as possible and to consider higher harmonic modes, more complex models have to be introduced, describing the cantilever as a flexible beam. In such a model, the cantilever is described as a beam clamped at one end and freely oscillating at the other end. This description includes different modes of vibration with their specific resonant frequencies. Here we do not develop longer this aspect but a complete treatment of the cantilever behavior can been found in [10].

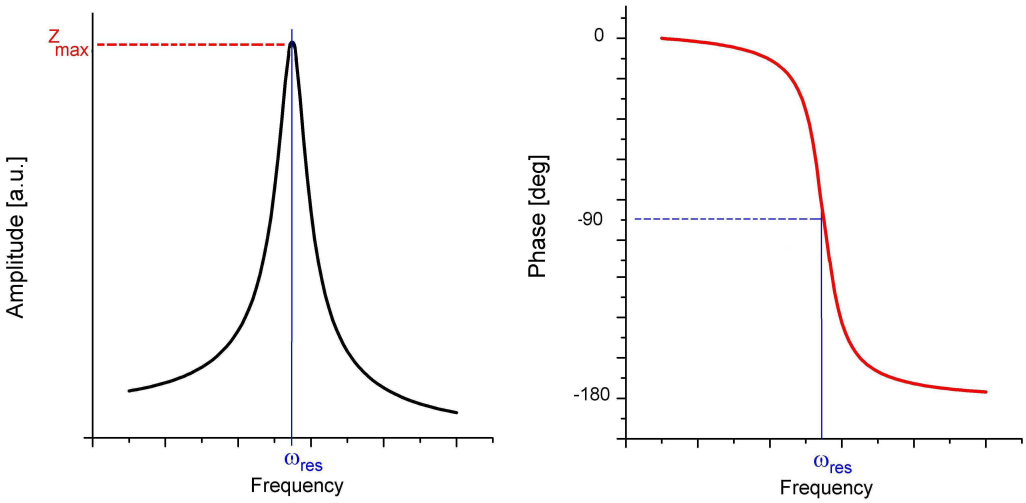

Figure 2.6: Amplitude and phase shift for a driven and damped oscillator

Spatial profile of the cantilever resonant modes

The spatial profile of an AFM cantilever can be obtained solving the Euler-Bernoulli equation [42, 43]

$$\rho(x)\frac{\partial^2 U(x,t)}{\partial t^2} + EI\frac{\partial^4 U(x,t)}{\partial x^4} = f(x,t) \tag{2.11}$$

where $U(x,t)$ is the cantilever profile as function of time and position, $\rho(x)$ is the material density, E the Young's modulus and $I = \frac{t^3 w}{12}$ the inertia momentum of the cantilever. General solution for the $n-th$ mode profile is [42, 43]

$$\begin{aligned} U_n(x) &= C_n\left[(\cos(k_n \cdot x) - \cosh(k_n \cdot x))\right] + \\ &+ G_n\left[(\sin(k_n \cdot x) - \sinh(k_n \cdot x))\right] \end{aligned} \tag{2.12}$$

where the $n-th$ mode vector k_n is linked with the $n-th$ mode resonant frequency by the relation $k_n^4 = \frac{\rho A}{EI}\omega_n^2$.
Applying the boundary condition, relation between coefficient C and G is found to be

$$\frac{C_n}{G_n} = -\frac{\cos(k_n \cdot L) + \cosh(k_n \cdot L)}{\sin(k_n \cdot L) + \sinh(k_n \cdot L)}. \tag{2.13}$$

In figure 2.7 the spatial profile of the first three resonant modes for a simple cantilever are shematically represented.

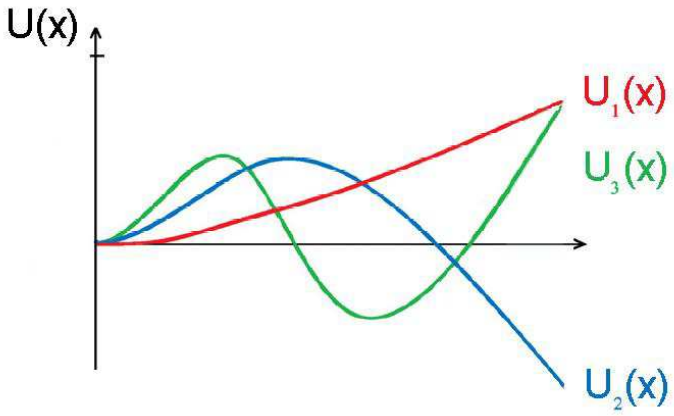

Figure 2.7: Spatial profile of the first 3 resonant modes for a simple cantilever.

2.3.1 Cantilever thermal noise

Figure 2.8 shows the response of a Cl in air at room temperature, when no external driving force has been applied. As it is clear the CL displacement power spectrum presents a resonance, meaning that actually even if we do not apply any force the oscillator is still excited.
The origin of this excitation is already well known and it is due to a random force induced by the coupling of the CL with the thermal bath. The behavior of a cantilever under a random excitation is well described by the displacement power spectral density

$$S_{zz}(\omega) =< \hat{z}^2(\omega) >= \int_{-\infty}^{\infty} C_{zz}(\tau) e^{-i\omega\tau} d\tau \tag{2.14}$$

defined as the Fourier transform of the cantilever position autocorrelation function

$$C_{zz}(\tau) = \langle z(t) \cdot z(t-\tau) \rangle. \tag{2.15}$$

The power spectral density is extremely useful in the description of Linear Time Invariant (LTI) dynamic systems with a complex response function $\chi(\omega)$ and a random input signal of power spectral density $S_{FF}\omega$, as in the case of a cantilever coupled with a thermal bath. The output power spectrum can be written as

$$S_{zz}(\omega) = S_{FF}(\omega)|\chi(\omega)|^2 \tag{2.16}$$

where $\chi(\omega)$ for the case in analysis is the cantilever transfer function.
According to the fluctuation-dissipation theorem, the random thermal excitation of the thermal bath at temperature T is described by a frequency

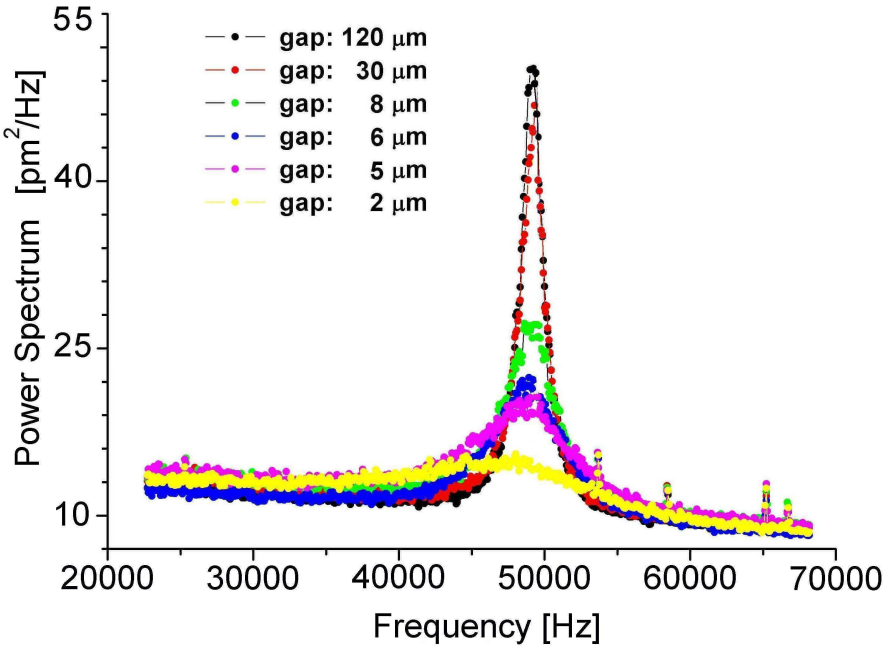

Figure 2.8: The experimental Brownian oscillation power spectrum of the microlever for different cavity gaps.

independent force power spectrum given by the Nyquist theorem:

$$S_{FF}(\omega) = 2k_B T\gamma \tag{2.17}$$

where k_B is the Boltzmann constant.
The position dispersion of the oscillator induced by the thermal excitation then is given by:

$$< z_T^2(t) >= \int_0^\infty S_{FF}(f)|\chi(f)|^2 df \tag{2.18}$$

with $f = \frac{\omega}{2\pi}$ At the thermal equilibrium the equipartition theorem set the position dispersion of the oscillator[1]

$$\frac{1}{2}k_{lev} < z_T^2(t) >= \frac{1}{2}k_B T. \tag{2.19}$$

In Fig. 2.8, the experimental thermal excited power spectrum is presented for different cavity gaps. It is clearly seen that the resonance peak dramatically broadens and softens to lower frequencies with decreasing gap. This is represented in figure 2.9 where the oscillator quality factor and resonant frequency are shown as function of the cavity gap.

[1] we have then a relation for the cantilever stiffness that give us for the case in analysis $k_{lev} = 0.0396\ N/m$

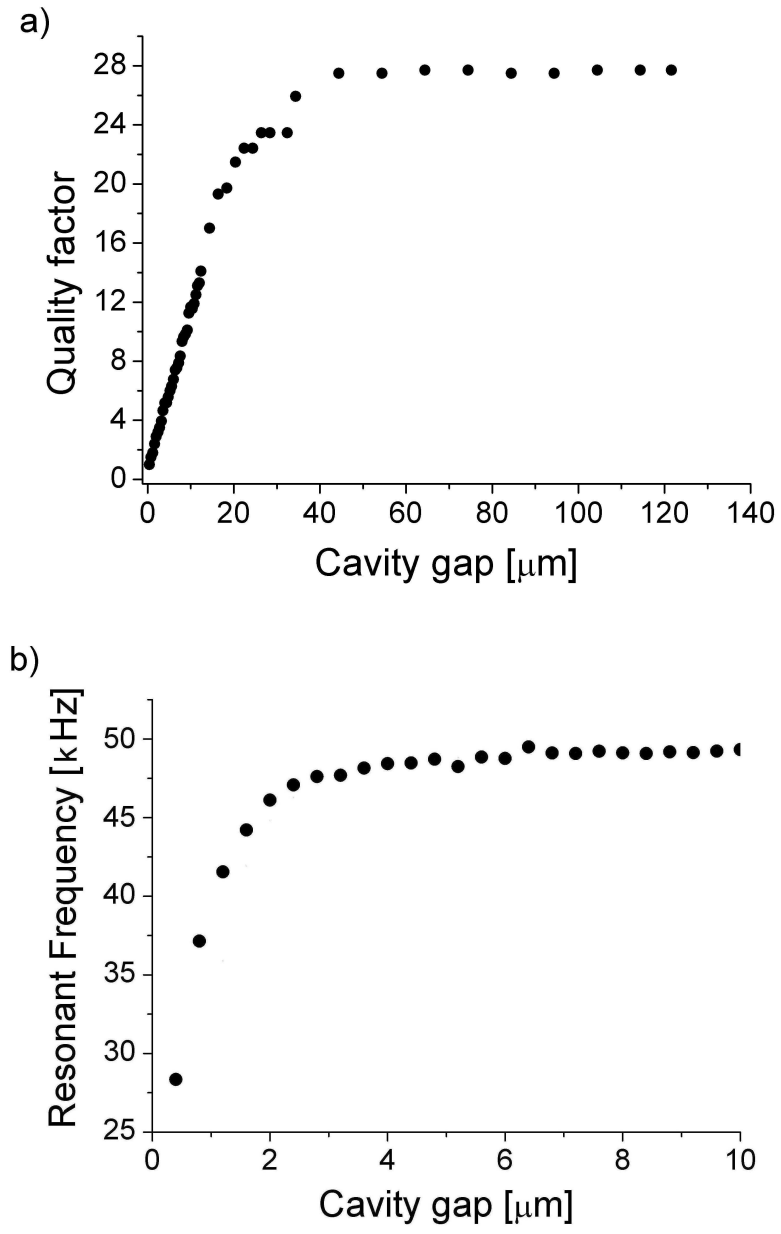

Figure 2.9: Experimental results: a) Evolution of the quality factor as function of the cavity gap. b) Evolution of the resonance frequency as function of the cavity gap

Within the experimental accuracy, the area under the resonance curves in Fig.2.8 remains constant and always equal to the thermal energy. This shows that the CL damping increases with decreasing gap.
Quantitative information on the damping factor can be obtained from the analysis of the CL quality factor, defined as $\frac{f_0}{\Delta f_{FWHM}}$, where Δf_{FWHM} is the full-width at half-maximum of the resonance curve (see Fig.2.8). This is because the two quantities are linked together by the relation $Q = \frac{k}{\omega_0 \gamma}$.
We expect that the damping factor γ is function of the fluid viscosity η, the cantilever surface A and, of course, the cavity gap d:

$$\gamma = C \cdot \eta \cdot A^{\alpha} \cdot d^{\beta} \tag{2.20}$$

where C is an adimensional constant. From the experimental evidence presented in figure 2.9 a), where the quality factor evolves linearly with the distance, we have $\beta = -1$. For dimensional reasons, then, $\alpha = 1$. The numerical constant is set to be very close to 2 leading to an expression of the damping factor

$$\gamma = \frac{2\eta A}{d}. \tag{2.21}$$

In figure 2.10 and 2.11, we can see how the expression of the damping factor as expressed in equation 2.21 is consistent with the experimental evidence.

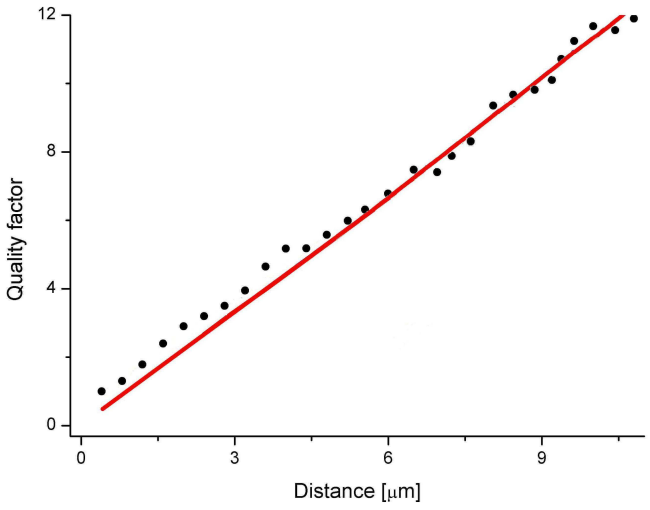

Figure 2.10: Quality factor evolution with the distance for the small gap regime. The red line represents the expression of the quality factor as in equation 2.21.

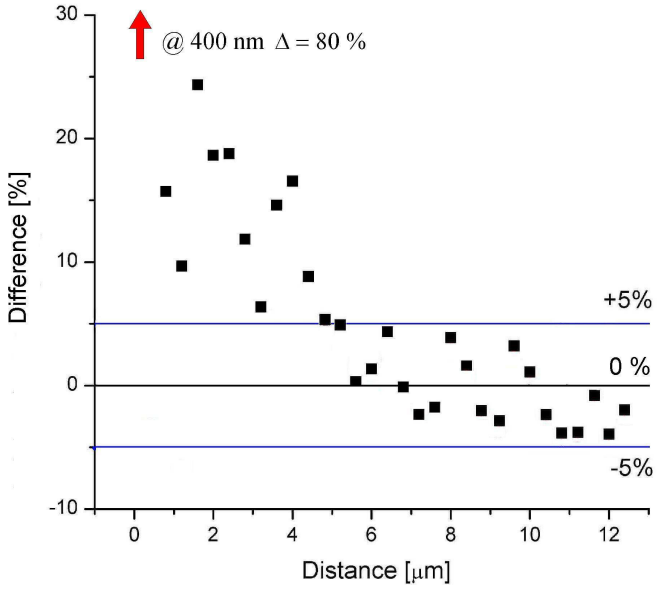

Figure 2.11: Difference between the experimental datas and the value obtained by equation 2.21.

2.4 Navier Stokes equation

A theoretical prediction of the damping factor should be obtained solving the Navier-Stokes equation with appropriate boundary conditions. Choosing the appropriate boudary conditions it is not a simple task. However only those leading to a theoretical expression consistent with eq. 2.21 can be considered valid to describe our system.
The fluid responsible for the CL damping is the air confined between the CL and the mobile fiber. The behavior of such a confined fluid can be described by the generalized Navier-Stokes equation:

$$\rho\left[\frac{\partial\vec{v}}{\partial t}+\vec{v}\cdot\nabla\vec{v}\right]=\eta\nabla^2\vec{v}-\nabla p \tag{2.22}$$

where $\vec{v}$ is the fluid velocity, ρ its density, η its viscosity and p the pressure. In the limit of small Reynolds numbers (here $Re := \frac{v\ d\ \rho}{\eta} < 0.001$ for $d = 50\ \mu m$) the fluid is in its laminar regime and equation 2.22 is slightly simplified in

$$\eta\nabla^2\vec{v}=\nabla p \tag{2.23}$$

The solution of eq. 2.23 implies a full knowledge of the boundary conditions existing at the fluid-solid interface. While for macroscopic hydrodynamic

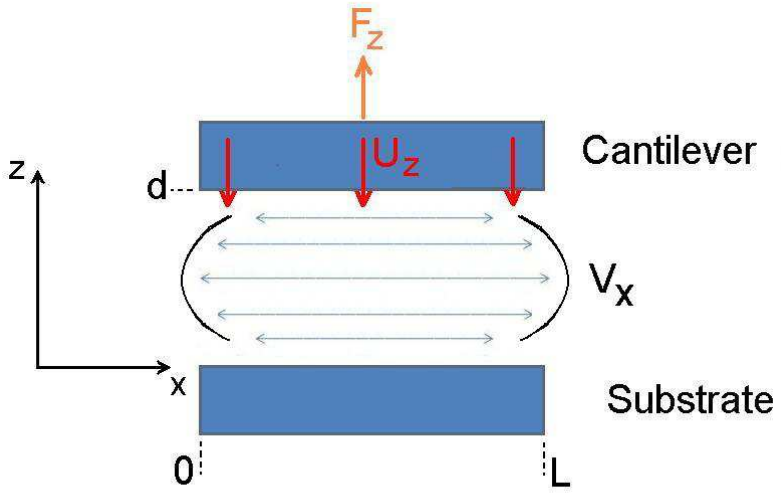

Figure 2.12: Scheme of the confinement of the fluid. The mobile plate represents the cantilever moving in the z direction with velocity U_z. The fluid motion is shown as v_x, the larger component of the fluid velocity

applications we can accept that the fluid do not slip against solid wall, this is not generally true for microfluidic problem involving MEMS or NEMS. The critical parameter in this respect is the Knudsen number $K_n = \lambda/d$ which depends on the gas mean free path λ. For air at ambient conditions $\lambda \approx 60\ nm$, leading here to $K_n \approx 0.001 - 0.06$. In this range of values it is already known that fluid slip can occur over a solid interface [44, 40, 41].
The theoretical model has to be consistent with the experimental evidence as presented in fig. 2.9, i.e. a damping factor with a dependecy over the distance as in equation 2.21

2.4.1 No slip boundary conditions (Couette problem)

We try now to solve the problem using the standard no slip boundary condition (see [44]). This is the well known Couette problem as presented in figure 2.12 In the hypothesis of Couette like problem, for the fluid velocity components we have $v_z << v_x$ and $\frac{\partial v_x}{\partial x} << \frac{\partial v_x}{\partial z}$.
Equation 2.23 becomes:

$$\eta \partial_z^2 v_x = \partial_x p. \tag{2.24}$$

Since at the lever extremity $x = 0$ and $x = L$, $p = p_0$ for all the z value, p is only a function of x, then

$$v_x(x,z) = \frac{1}{2\eta}p'(x)z^2 + \alpha(x)z + \beta(x). \tag{2.25}$$

From the no slip boundary conditions, $v_x(x, z = 0) = v_x(x, z = d) = 0$, we have

$$v_x(x,z) = \frac{1}{2\eta}p'(x)\left(z^2 - zd\right). \tag{2.26}$$

The fluid incompressibility condition $\partial_x v_x + \partial_z v_z = 0$ gives the expression of v_z:

$$v_z(x,z) = \frac{1}{2\eta}p''(x)\left(\frac{z^3}{3} - \frac{z^2}{2}d\right). \tag{2.27}$$

For $z = d$ the fluid vertical velocity v_z is equal to the cantilever speed U_z. This gives a condition for the pressure p expression

$$p(x) = p_0 + \frac{6\eta}{d^3}U_z(xL - x^2). \tag{2.28}$$

The viscous force along z direction (per surface unit) acting on the cantilever moving plate is given by:

$$f_z = \sigma_{zz} = \eta(\partial_z v_z + \partial_z v_z)(z = d), \tag{2.29}$$

where σ_{zz} is the fluid deformation tensor along the z direction. The fluid velocity component in eq. 2.27 leads to a null viscous force acting to the lever.
The only non null force acting on the lever is a pressure force induced by the squeezing of the fluid:

$$F = \int_0^w dy \int_0^L dx(p_{ext} - p_{int}) = \int_0^w dy \int_0^L dx \left[-\frac{6\eta}{d^3}U_z(xL - x^2)\right] = -\frac{\eta L^3 w}{d^3}U_z. \tag{2.30}$$

Therefore the damping factor takes the simple form:

$$\gamma = \frac{F}{U_z} = \frac{\eta L^3 w}{d^3} \tag{2.31}$$

This relation is not consistent and it cannot be compared with the experimental evidence as presented in figures 2.8, 2.9 a) and b).
The no slip boundary conditions cannot be applied to the system here in analysis. Such boundary conditions, generally accepted for macroscopic system, seem to fail when applied to fluid confined in sub micron cavities.

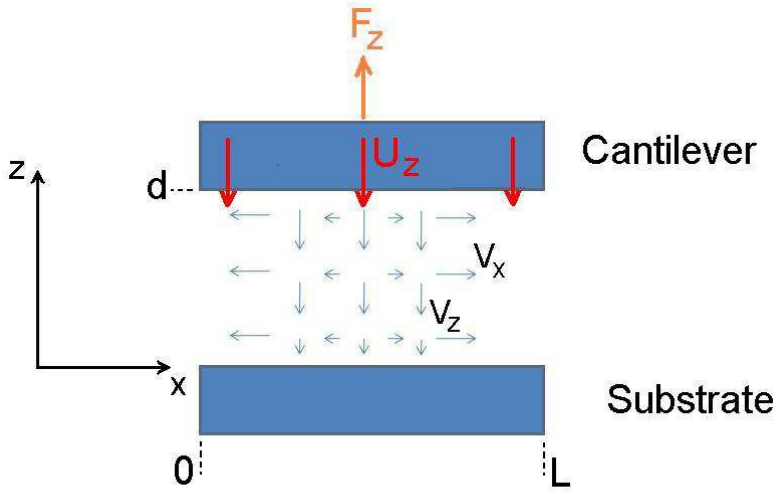

Figure 2.13: Scheme of the confinement of the fluid. The mobile plate represents the cantilever moving in the z direction with velocity U_z. The fluid motion is shown as a two components velocity vector $\vec{v} = v_x, v_z$. F_z is the dissipating force acting on the mobile plate

2.4.2 Perfect slip boundary conditions

To solve the Navier-Stokes equation as simplified in eq. 2.23 we now can suppose that $v_x = f(x)$. This is a very demanding hypothesis as it formally leads to assume a slip boundary condition. From the fluid incompressibility condition $\partial_x v_x + \partial_z v_z = 0$ we have another condition on the fluid velocity component $v_z = g(z)$.
The linearized Navier-Stokes equations become then:

$$\begin{aligned} \frac{\partial p}{\partial x} &= \eta \frac{d^2 v_x}{dx^2} \\ \frac{\partial p}{\partial z} &= \eta \frac{d^2 v_z}{dz^2} \end{aligned} \tag{2.32}$$

This implies $\frac{\partial p}{\partial x} = a(x)$ and $\frac{\partial p}{\partial z} = b(z)$ or

$$p(x,z) = \int_0^L a(x)dx + \int_0^d b(z)dz = A(x) + B(z). \tag{2.33}$$

However the only solution possible is here $p(x,z) = p(x) = A(x)$ since at the lever extremity $x = 0$ and $x = L$ we have $p = p_0$ for all the z value.

Equation 2.32 then reads:

$$\eta \frac{d^2 v_x}{dx^2} = \frac{\partial p}{\partial x} \tag{2.34}$$

$$\frac{d^2 v_z}{dz^2} = 0. \tag{2.35}$$

The second equation leads to

$$v_z(z) = \alpha z + \beta. \tag{2.36}$$

Since $v_z(z = 0) = 0$ and $v_z(z = d) = U_z$ we deduce:

$$v_z(z) = \frac{U_z}{d} z. \tag{2.37}$$

Such expression of the fluid component leads to a viscous force along z acting on the plate (per surface unit)

$$f_z = \sigma_{zz} = \eta(\partial_z v_z + \partial_z v_z)(z = d) = -\frac{2\eta U_z}{d}, \tag{2.38}$$

where σ_{zz} is the fluid deformation tensor along the z direction. Therefore the damping factor takes the simple form:

$$\gamma = \frac{F_z}{U_z} = \frac{\int_A f_z dS}{U_z} = \frac{2\eta A}{d} \tag{2.39}$$

Equation 2.39 gives a relation of the damping factor with the cavity gap. This relation is consistent and it can be compared with the experimental evidence as presented in figures 2.8, 2.9 a) and 2.9 b).
Such boundary conditions, generally not applied to macroscopic systems, well reproduce the experimental evidence for fluid confined sub micron cavities.

Slip conditions

We can now come back to definition of the slip condition. As precedently reminded the slip condition formally coincides to $\partial_z v_x = 0$. From eq. 2.37 we can now deduce the expression of the velocity component v_x. From the incompressibility condition $\partial_x v_x + \partial_z v_z = 0$

$$v_x(x) = -\frac{U_z}{d} x + \delta \tag{2.40}$$

which indeed satisfies eq. 2.34 and implies $\frac{dp}{dx} = 0$ and $p = p_0$.
At $x = 0$ we have $v_x = v_0$ and at $x = L$, for symmetry we have $v_x = -v_0$, meaning $v_0 = \delta = \frac{U_z L}{2d}$ that gives:

$$v_x(x) = \frac{U_z}{d}\left(\frac{L}{2} - x\right). \tag{2.41}$$

Clearly from eq. 2.37 we have $v_x = f(x)$ coinciding with the previously defined slip conditions. This reminds the old Navier boundary conditions which has been subject of controversy since the 19^{th} century.

Energy conservation

As a further check we can verify the energy conservation during the process. From the Navier-Stokes equation, considering a plate that is moving at the velocity U_z, we have [44]:

$$\frac{dE_f}{dt} = \frac{d}{dt}\int_{fluid} \frac{\rho v^2}{2} d^3x =$$

$$= -\frac{1}{2\eta}\int_{fluid} \sum_{i,j} \sigma_{i,j}^2 d^3x - \oint \left[(v_j - U_j)\,\rho v^2/2 + v_j p - v_i \sigma_{i,j}\right] dS_j \tag{2.42}$$

with $\sigma_{i,j} = \eta(\partial_i v_j + \partial_j v_i)$. In the stationary regime, $\frac{dE_f}{dt} = 0$, we have:

$$-\frac{1}{2\eta}\int_{fluid} \sum_{i,j} \sigma_{i,j}^2 d^3x = \oint \left[(v_j - U_j)\,\rho v^2/2 + v_j p - v_i \sigma_{i,j}\right] dS_j \tag{2.43}$$

The right side of eq. 2.43, *i. e.* the loss term, is

$$-\frac{1}{2\eta}\int_{fluid} \sum_{i,j} \sigma_{i,j}^2 d^3x = -\frac{1}{2\eta}\left(\sigma_{xx}^2 + \sigma_{zz}^2\right) \cdot A \cdot d = -\frac{4\eta U_z^2}{d} A. \tag{2.44}$$

The surface integral is divided into 4 integrals. The integral along the moving plate reads:

$$\int_{z=d} \left[-\left(v_z + U_z\right)\rho v^2/2 - v_z p + v_z p \sigma_{zz}\right] dS_z = \frac{2\eta U_z^2}{d} A + U_z p_0 A. \tag{2.45}$$

The integral along the static plate is formally equal to that of the moving plate and vanishes. The other two integrals are:

$$\int_{x=L} \left[-v_x p + v_x p \sigma_{xx}\right] dS_x = \frac{\eta U_z^2}{d} A - \frac{U_z p_0 A}{2} \tag{2.46}$$

and

$$-\int_{x=0} \left[-v_x p + v_x p \sigma_{xx}\right] dS_x = \frac{\eta U_z^2}{d} A - \frac{U_z p_0 A}{2}. \tag{2.47}$$

Consequently the equation 2.43 for the energy conservation is verified.

2.5 Cavity damping of the cantilever

Starting from equation 2.39, we obtain a theoretical expression for the cantilever quality factor, in the small gap regime:

$$Q = \frac{k}{2\omega_0 \eta A} d. \tag{2.48}$$

Eq. 2.48 predicts a linear dependence of the quality factor with the gap width and provides us with the opportunity of comparing theory and experiment without including any adjustable parameter whatsoever since all physical parameters are known [2].

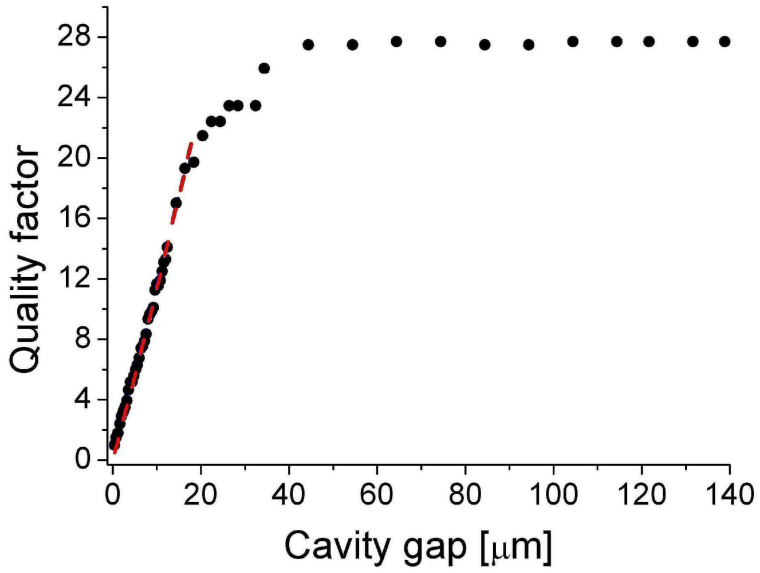

Figure 2.14: The quality factor as a function of the cavity gap. Black dots represent the experimental data. The red curve exhibits the theoretical prediction based on eq. 2.48.

Fig. 2.14 depicts the quality factor as function of the cavity gap. Two different regimes can be distinguished. For large gaps above 40 μm, the quality factor remains constant. This is the unconfined fluid regime where no additional damping can take place with decreasing gap. For smaller gaps however, the quality factor tends to decrease with a decreasing gap. We will focus below on the small gap regime where the hypothesis of infinite planes

[2]The CL dimensions have been measured by electron microscopy. The air viscosity was taken as $1.8 \times 10^{-5} kg/ms$. The CL stiffness $k = 0.0396 N/m$ has been experimentally determined from Fig. 2.8 using the energy equipartition theorem.

is physically justified. From fig. 2.14 we clearly see that $d_{lim} \approx 20\mu m$.

2.5.1 Plane misalignment correction

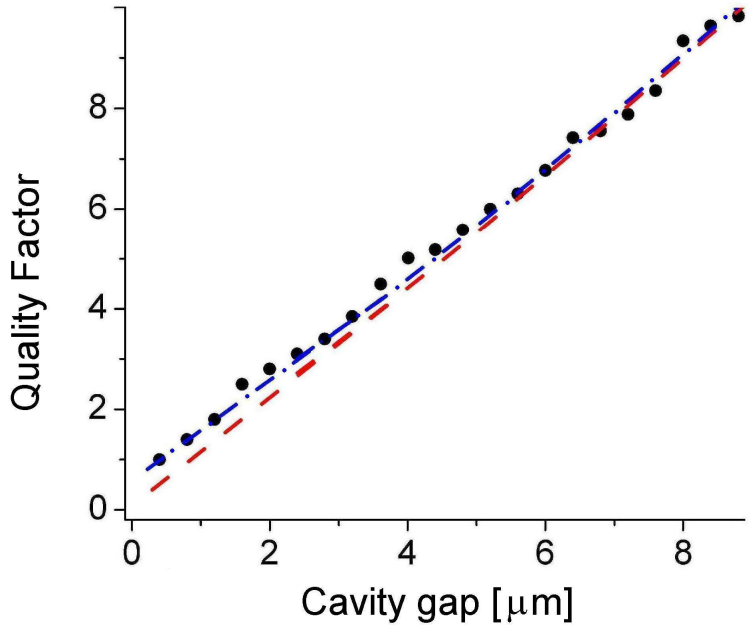

Figure 2.15: The quality factor as a function of the cavity gap. Black dots represent the experimental data. The red curve exhibits the theoretical prediction based on eq. 2.48. The blue dotted curve exhibits the theoretical prediction based on eq. 2.48 when the misalignment between the planes has taken into account

As shown in fig. 2.15 the experimental results and the theoretical prediction of Eq. 2.48 coincide to within 5% for gaps larger than 5 μm but for smaller separations, the agreement worsens, to reach 100% at the smallest gap, 400 nm. We argue now that this increasing disagreement is not due to a failure of our approach, but that it originates from a residual small misalignment of the two facing parallel plates.
In the hypothesis of a small angular misalignment, the problem can be treated within an approximation similar to the Proximity Force Approximation (PFA) used, for instance, for the Casimir force formulation in the sphere-plane geometry [21]. Using this approximation, we compute the cor-

rected damping factor to be:

$$\gamma = \int_0^L \int_0^w 2\eta \frac{dx \cdot dy}{d_0 + x\tan\alpha + y\tan\beta} \tag{2.49}$$

where d_0 is the shortest distance from the inclined CL to the substrate, α (respectfully β) is the lateral tilt angle of the CL with the mobile surface in the x (respectfully y) direction. The angle values that permit to reproduce the evolution of the disagreement between experiment and theory, as presented in Fig. 2.15, are $\alpha \approx \beta \approx 10\ mrad$. Considering these misalignment angles, the good agreement between theory and experiment can now be extended down to the smallest gap range that we have measured as can be seen in Fig. 2.15. Over the entire range $400\ nm - 20\ \mu m$, the remaining disagreement is $\approx 5\%$.

2.6 Cavity freezing of a cantilever

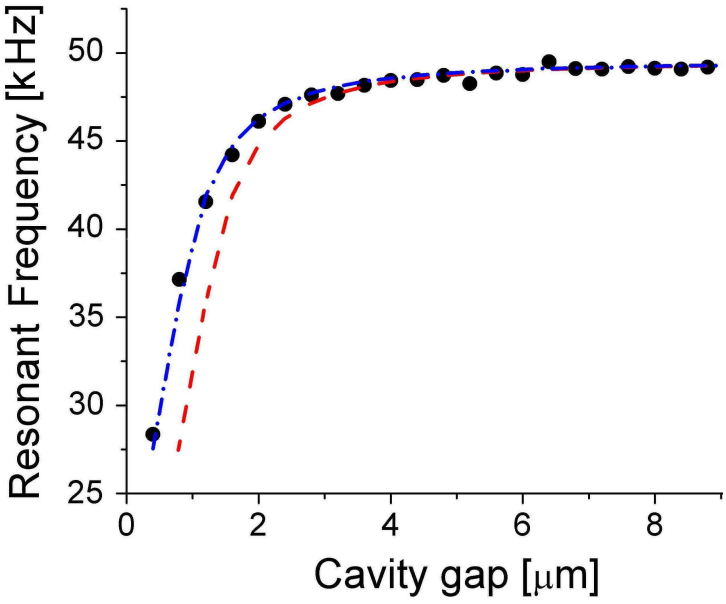

Figure 2.16: The resonance frequency as function of the cavity gap in the small gap regime. Like in Fig.2.14, the red dashed, respectively blue dash-dotted curves is the prediction of the NS model for the perfectly aligned, respectively slightly misaligned, cavity.

We now discuss the frequency softening of the CL oscillation, the other salient experimental fact revealed by Fig. 2.8.
In the limit of large damping, *i.e.* the approximation $\frac{\gamma}{m} << \omega_0$ no longer holds, the power spectrum has a down-shifted resonance frequency ω' given by equation 2.10. Fig. 2.16 shows that the resonance frequency shift $\omega' - \omega_0$ can be extremely large. We can see that actually if the cavity gap is small enough the resonant frequency value tends to zero.
Considering the damping factor expression in eq. 2.39 we can then define another characteristic length which is the gap width canceling the resonance frequency in Eq. 2.10. This characteristic length is determined by the CL dynamics and the fluid viscosity and is given by:

$$d_{crit} = \frac{\sqrt{2}\eta}{m}\frac{A}{\omega_0} = \frac{\sqrt{2}\eta}{\rho t \omega_0}. \tag{2.50}$$

with ρ the lever material density and t its thickness. From equation 2.50 we would expect a critical gap of about 500 nm, however experimentally it has been impossible to achieve the complete freezing because of the residual angular misalignment discussed above that prevents any step further below $400nm$.
Taking into account for data analysis of the misalignment obtained from Fig. 2.14, we can quantitatively model the measurements in Fig. 2.16 using equation 2.10.

2.7 MEMS and NEMS application

Along this chapter we have presented measurements of the damping of a thermally driven CL in a simple fluid confined in a microcavity formed by this CL facing an infinite wall. As the cavity length decreases, the fluid confinement induces a dramatic damping of the CL Brownian motion which can lead to its complete freezing at small gaps. A consequence of what here revealed, is that micro- or nano-oscillators can either present high Q factors or be overdamped systems depending on their actual geometry, resonance frequency, oscillator substrate gap and, of course, on the ambient viscosity. What is worth to note is the gap size involved. For example we have seen that for the lever in analysis the complete freezing happens for cavities smaller than 500 nm. These values are indeed closed to the standard application of NEMS and MEMS.
The definition of the critical gap as in equation 2.50 shows a dependency by the dynamical and material properties of the oscillator.
In fig. 2.17 it is shown an example of MEMS realized at the CEA-LETI in

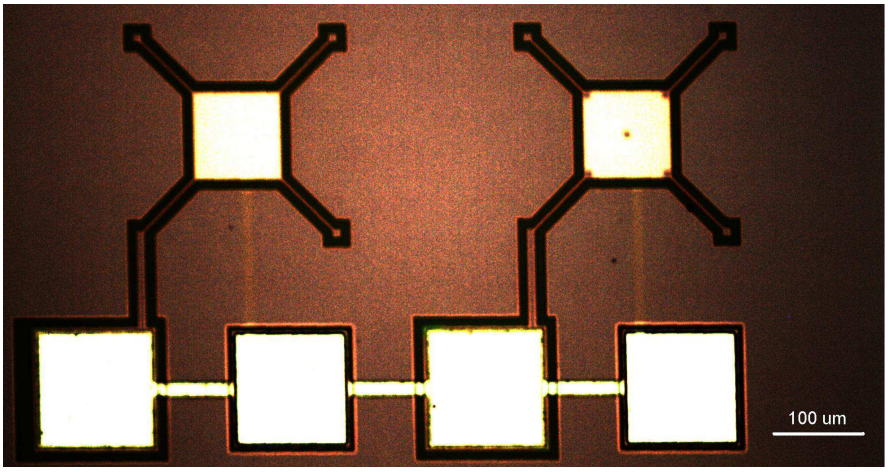

Figure 2.17: Optical microscope image of 10G-100-100 MEMS realized at the CEA-LETI in Grenoble.

Grenoble. This kind of MEMS is a silicon membrane oscillating out of plane. The lateral size varies from 10×10 μm^2 to 100×100 μm^2 (as presented in figure 2.17). while the thickness is constant at 200 nm, The gap with the substrate is 400 nm. The membrane is suspended using four beams. This is the most interesting aspect of such kind of structure. In fact even if the lateral size is kept constant, only modifying the size of the four beams, it is possible to change the resonant frequency (see table 2.1).
Since the membrane surface is much bigger than the the beams surface the cavity formed with the substrate can be considered constant.
Fig. 2.18 shows the variations of d_c as a function of $f_0 = \omega_0/(2\pi)$ for a thin oscillator with $t = 180$ nm and for different commonly used materials.
For low frequencies in the 10 kHz range and below, the overdamping regime appears already at large separation distance $d_c \geq$ 0.1-1 μm. Oppositely, for very high oscillator frequencies in the 100 kHz range and beyond we have $d_c \leq 10 - 100$ nm and the overdamping regime becomes a fundamental issue only at the nanoscale.
For comparison we show on the same graph the experimental data points taken from figure 2.8 and corresponding to working distances d which are decreasing until the overdamped regime at d_c is reached. Additionally, we show also the physical characteristics recorded (i.e., internal resonance frequency f_0, and fixed distance gap $d = 400$ nm with the substrate) of typical Si made NEMS realized at the LETI. These NEMS can be with a good approximation described by the simple geometry considered here.
Clearly, working with such NEMS in a gaseous environment may strongly af-

MEMS	Membrane size	Beam width	Beam length	Resonance
XG-10-1	10 μm	3 μm	1 μm	18.7 MHz
XG-10-10	10 μm	3 μm	10 μm	2.4 MHz
XG-10-50	10 μm	3 μm	50 μm	217.5 kHz
XG-50-1	50 μm	3 μm	1 μm	4.8 MHz
XG-50-10	50 μm	3 μm	10 μm	482.8 kHz
XG-50-50	50 μm	3 μm	50 μm	43.5 kHz
10G-100-50	100 μm	3 μm	50 μm	10.7 kHz
10G-100-100	100 μm	3 μm	100 μm	26.5 kHz
50G-100-50	100 μm	10 μm	50 μm	19.5 kHz
50G-100-100	100 μm	10 μm	100 μm	48.3 kHz

Table 2.1: CEA-LETI mechanical system characteristics. For all these structures the cavity gap with the substrate is 400 nm

fect their dynamics and only for very high f_0 could the overdamping regime actually be overcome. This is indeed confirmed for those NEMS annexed by a red cross in Fig. 2.18 which we studied experimentally. The experiment showed that NEMS with such gaps do not resonate in air at room temperature confirming therefore the role played by overdamping. For the NEMS indicated by a red circle, *i.e.*, with frequency in the 100 kHz and MHz range we were out of the detection sensibility of our setup and no data were available.

Reminding that for the simple mechanical system here analysed we have $\omega_0 = \sqrt{\frac{E}{12\rho}} r_0^2 \cdot \frac{t}{L^2}$, (where r_0 gives informations about the geometry of the oscillator) as a complementary analysis, we show in fig. 2.19 the explicit dependence of d_c on the aspect ratio t/L for different materials. In the typical range of aspect ratio considered the overdamping regime covers distance gaps d going from the micrometer range to the nanoscale and, therefore, cannot be neglected. Again, this fact is confirmed by comparing these graphs with available experimental data (see Fig. 2.19 and compare with Fig. 2.18). It is evident that the confinement effect cannot be neglected while speaking of NEMS and MEMS operating in viscous environments. Interesting extensions of the present work include the study of even smaller gaps and of damping as function of air pressure to link the viscous and the molecular regimes [22].

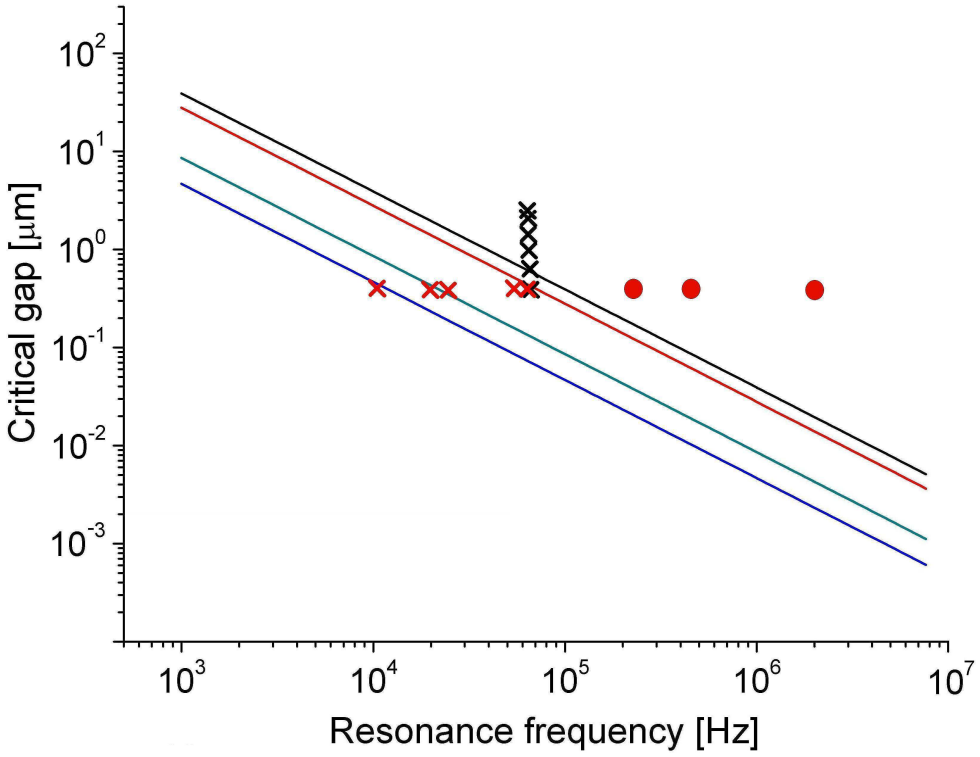

Figure 2.18: Evolution of critical gap as a function of frequency for a Si (black line), SiC (red line), GaAs (green line), and Au (blue line), respectively. Experimental data points for the lever studied in previuos paragraph are also shown for distances d close to the overdamping regime (black crosses). Red crosses and circles correspond to NEMS with a distance to the substrate $d = 400nm$.

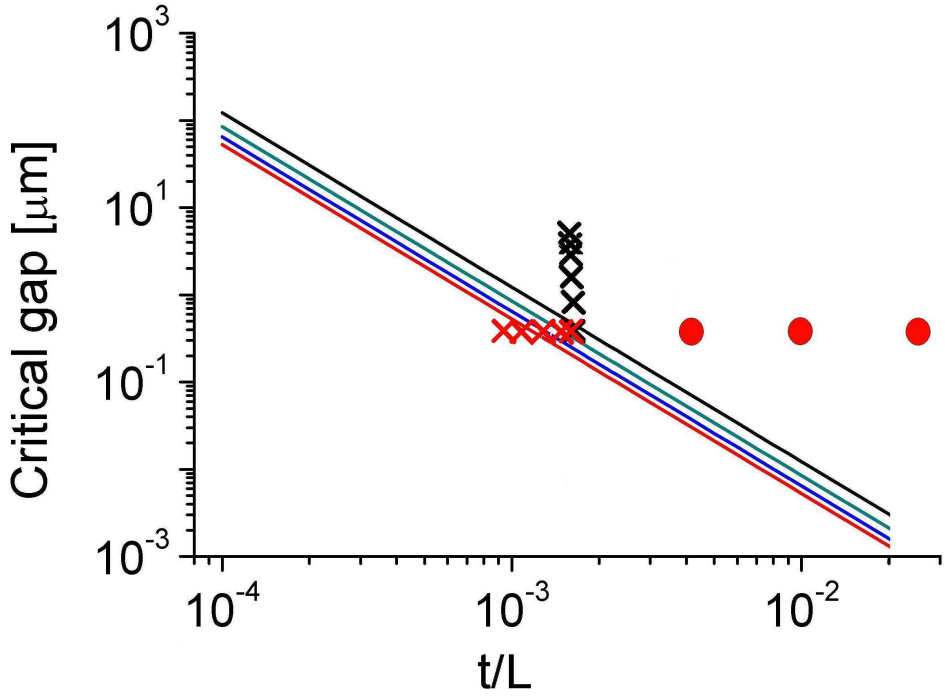

Figure 2.19: Evolution of the critical gap as a function of the ratio t/L for the same lever materials as in Fig. 2.18. Colors lines and data points have the same meaning as in Fig. 2.18.

Interactions entre rayons X et oscillateur mécanique

Les MEMS et NEMS sont souvent utilisés pour mesurer les interactions et les accélérations à l'échelle nanométrique. Les NEMS sont d'excellents détecteurs de forces. Ainsi de petits effets comme les propriétés mécaniques de la lumière ont éte étudier grâce à ces systémes. En effet la pression de radiation et le switch thermique ont été utilisés comme moyen d'actionnement pour les systèmes mécaniques. Dans ce chapitre nous nous pencherons sur l'effet de la lumière synchrotron agissant sur un MEMS. Nous montrerons comment l'interaction entre le faisceau de rayons X et le système mécanique peut potentiellement ouvrir une nouvelle famille d'outils pour la manipulation de rayons X.

Chapter 3

X-ray interactions with Micro Electro Mechanical Systems

Contents

3.1 Introduction

Nanoelectromechanical Systems are frequently used to measure interactions and accelerations at nanoscale [3, 4, 5], especially when resonating oscillators are used with high quality factor [6, 7, 8].
NEMS are excellent force detectors and even small effects as the mechanical properties of the light have been addressed thanks to them. Indeed radiation pressure and thermal switch effects in the lever [14, 15, 16, 17, 18, 19, 20]

have been shown as actuation mechanisms for mechanical systems.
In chapter 2 we have seen that nano oscillating cantilevers can be used for the study of fluid behavior at micron and sub-micron scale.
In this chapter that Micro and possibly Nano Electro Mechanical Systems can be considered suitable for developing new tools in the domain of Synchrotron light techniques.
Typical X-ray beam spot size was in the millimeter or sub-millimeter scale. Nowadays it is in the micron and it will reach the sub-micron regime. At the European Synchrotron Radiation Facility, the recently started upgrade program should bring at X-ray beams with a size in the tens of nanometers. Power transported by these X-ray beams, with 10^{12} ph/sec at 10 keV is $W = 1$ mW; the force in case of full absorption is $W/c = 10$ pN. These numbers are the classical ones when opto-mechanical effects are studied using visible light.
It then appears that effects usually observed using visible laser should also be observed using X-ray beams, with a clear advantage that light-matter interaction can be made quantitavive as we shall see using both absorption and diffraction instead of reflection and refraction. A drawback is, however, that the wavelenght is not so easily precisely defined. Effect such as optical cooling will be very hard to produce using X-ray.
The first part of this chapter will be dedicated to the study of the interaction between X-rays and MEMS and how it can be actually controlled.
We shall also enter the use of MEMS to shape in real time the X-ray beams. Nowadays many experiments in physics, biology, chemistry and material science require irradiation of a sample by a short burst of X-ray radiation to study in details the time response of the sample under a particular excitation [45, 46, 47]. X-ray techniques are extremely important to investigate the chemistry and structure of materials [48, 49]. In a typical experiment the system to be analyzed is excited by a short X-ray burst and information about the response is obtained studying the fluorescence emitted during the system's de-excitation [50, 51].
In a pump-probe experiment, the sample is pumped in a metastable state by laser excitation and a delayed X-ray pulse is used to monitor the time evolution of the system [52, 53, 54]. A common aspect of these two kinds of experiment is the required duration of the X-ray pulse. Since the time scale involved can be smaller than microsecond, X-ray pulses with duration less than a microsecond are then required [55, 56, 57]. Today, short duration X-ray burst are typically produced when a continuous X-ray beam passes through a mechanical shutter that is open for a short time [58]. The major limitations of rotating mechanical shutters are the size and the operation environment required. They actually need to work under vacuum condition

especially if a very short X-ray pulse has to be realized.
Considering the characteritic parameters of nano- and micro-oscillator it would be envisagable to show that it is possible to shape a beam with a MEMS or NEMS. For this reason in the second part of the chapter we will focus the attention on this particular application for a MEMS and we will show how it is possible to realize a fast X-ray chopper using a standard AFM silicon microcantilever.

3.2 European Synchrotron Radiation Facility (ESRF)

The experiments presented in this chapter have been performed at the European Synchrotron Radiation Facility in Grenoble. The ESRF is a joint facility supported by almost 20 european coutries, employing 600 people and hosting more then 5000 researchers over the year.
As can be seen in official web-site, it operates the most powerful synchrotron radiation source in Europe and one the three most powerful in the world (together with APS in USA and Spring8 in Japan).

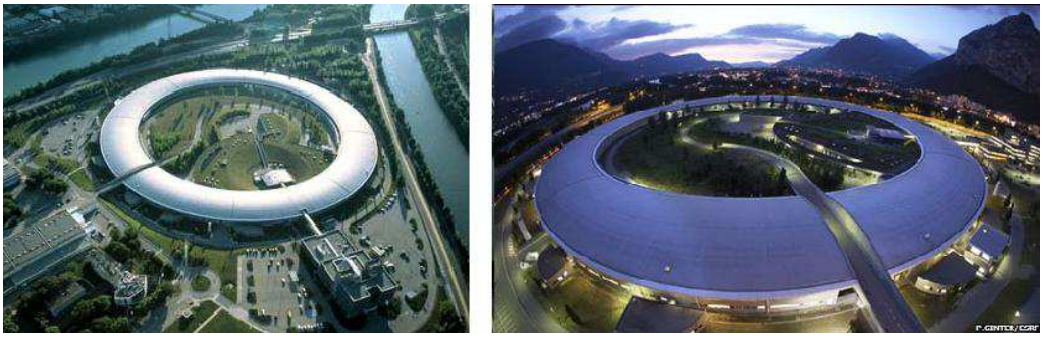

Figure 3.1: The European Synchrotron Radiation Facility (ESRF) in Grenoble (from ESRF web-site).

The European Synchtron Radiation Facility can be seen as a 800 m diameter microscope. The size is not that of a conventional microspope and also the perfomances are not the same. Any other conventional laboratory X-ray source can be compared to facility like ESRF for flux, energy range and resolution of X-ray radiation.
The actual size of the inner ring diameter is 844 m and the electrons inside have an energy of 6 GeV. Around the inner ring, forty tangential beamlines have been constructed, helping researchers in fields as diverse as protein crystallography, earth science, material science, chemistry and physics.

Along this chapter we will see two different types of experiment that can be performed in a Synchrotron facility: the first one will be a simple example of X-ray absorption, while the second one will be an example of diffraction. Before entering in the analysis of the experiments is then opportune to make a short introduction to these two standard synchrotron techniques.

3.2.1 X-ray absorption

When an X-ray beam impacts onto a material body, a part of the incident photons is absorbed by the matter. The amount of the absorption depends on the particular material. The Lambert-Beer's law gives the intensity $I(\omega)$ after a beam with incident intensity $I_0(\omega)$ has passed through a slab of thickness d:

$$I(\omega) = I_0(\omega)e^{-\mu(\omega)d} \tag{3.1}$$

where $\mu(\omega)$ is the absorption cross section, strongly dependent on the sample's composition. $\mu(\omega)$ presents sharp steps denominated absorption edges for incident photon energy close to the energy of an electron binded to a specific shell. The energy position of the steps depends on the chemical arrangment of the particular atom being studied, and it is very different from element to element. Furthermore it may present oscillations after the edge which are the result of the interaction between differently scattered electron waves. This richness of in fine structure makes X-ray absorption an important tool for the characteristization and study of any type of material i.e. atoms, molecules, surface solids or liquids.
A particular absorption technique we will discuss in the chapter, is the so called Extended X-ray Absorption Fine Structure (EXAFS). When a photon is absorbed by an atom above an absorption edge, the excess energy takes the form of a photoelectron leaving the atom in an excited state. Since electron are wave like particle they can interfere with the wave reflected back, changing the final state, increasing or decreasing then the probability of absorbing the incoming photon. The condition for constructive or destructive interference depends on the path traveled by the elecron waves, i.e. the position of the atom respect with the others, and on the photoelectron wavelength. This results in oscillations of the absorption probability as a function of incident photon energy. They are visible few eV up to thousands eV after the edge. From the oscillation periodicity one can calculate the distances between different atom shells.

3.2.2 X-ray diffraction

Diffraction involves the illumination of a crystal sample, or an ensemble of crystals. Every atoms of the material can interact with incoming X-ray beam. If the material is ordered the diffusion of the X-ray beam can present conditions for constructive or destructive interference. The Bragg's law give a satifactory description of this intereference pattern:

$$2d \sin\theta \left(1 - \frac{\delta}{\sin^2\theta}\right) = n\lambda_n \tag{3.2}$$

where λ is the wavelength of the incoming radiation, $(1-\delta)$ the real part of the refraction index. The factor $\left(1 - \frac{\delta}{\sin^2\theta}\right)$ is usually considered equal to one, leading to an approximate relationship; d here is the distance between diffracting planes and θ is the incidence angle of the X-ray beam.. For a certain set of planes there is a characteristic angle that fulfils the diffraction condition for a given energy

3.3 Mechanical effects of an X-ray beam on a MEMS

In this paragraph we focus the attention onto the interaction between an intensity modulated X-ray beam and a simple micro-oscillator. In this particular experiment the MEMS is a microswing constituted by a Ge microcrystal attached to a Si microcantilever. The X-ray beam is impinging on the Ge block and force the cantilever to oscillate. Understanding and controlling the oscillation amplitude require to be able to control and tune the interaction MEMS/X-rays.

The experimental set-up is presented in fig. 3.2. SEM images of the microswings used are shown in fig. 3.2(b) and 3.2(c). The first Ge microcrystal in fig. 3.2(b) has been directly cut to Ge wafer by a Focus Ion Beam (FIB). In order to fabricate the micro-oscillator, a cubic like germanium crystal has been etched from a germanium wafer using the FIB Strata400 from FEI. The cube was welded to the cantilever, in a symmetrical position, using localized FIB deposition of metal. The cubic Ge crystal is 43 μm thick. The lever is a standard Silicon AFM cantilever whose dimensions are 350x35x2 μm^3. This lever has no metallic coating. The second Ge microcrystal is about 23 μm thick (fig. 3.2(c)). It has been manually glued on the side of the cantilever in a very asymmetrical position. For asymmetrically mounted crystals, two types of levers have been used: one without metallic coating and another with metallic coating.

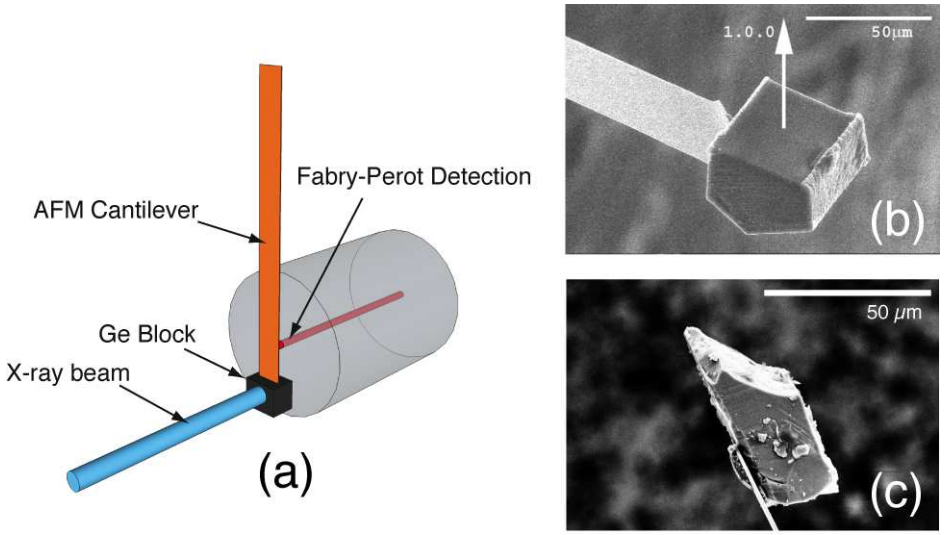

Figure 3.2: (a) Experimental setup. Blue ray is the X-ray beam on the Ge micro-crystal at orange Si lever end. Grey cylinder represents the optical fiber and the red ray is the laser beam used to detect the lever position with sub-Angstrom precision. (b and c) SEM image of the Ge cubes glued on Si levers. In (b) the cut and soldered Ge crystal using a Focus Ion Beam, has been positioned at the end of the lever in a symmetrical position. In (c) a Ge crystal has been manually glued on the side in a very asymmetrical position.

The microswing position is measured through the interference between the light reflected from the back of the lever and from a cleaved fiber end, as presented in chapter 2.
The beamlines involved for this experiment were the Anomalous Scattering Beamline (ID01) and Surface Science X-Ray Diffraction (SXRD) Beamline (ID03). In ID01 the radiation from the undulators can be tuned from 2.5 to 40 keV with a Si(111) double crystal monochromator. Focusing is achieved by using beryllium Compound Refractive Lenses (CRLs) [59]. The effective focus size is $\approx 4 \times 6\,\mu m^2$ with $\approx 10^{10}$ photons/second on the focal spot.
At the SXRD beamline the photons were tuned at the Ge K edge using a liquid nitrogen cooled monolithic double crystal Si (111) monochromator. The beam was focused at the sample by a Kirkpatrick-Baez (KB) mirror system located 43 m from the photon source. The beam size at the sample, 1 m from the KB system, is $\approx 3 \times 5\,\mu m^2$ with $\approx 10^{12}$ photons/second on the focal spot.

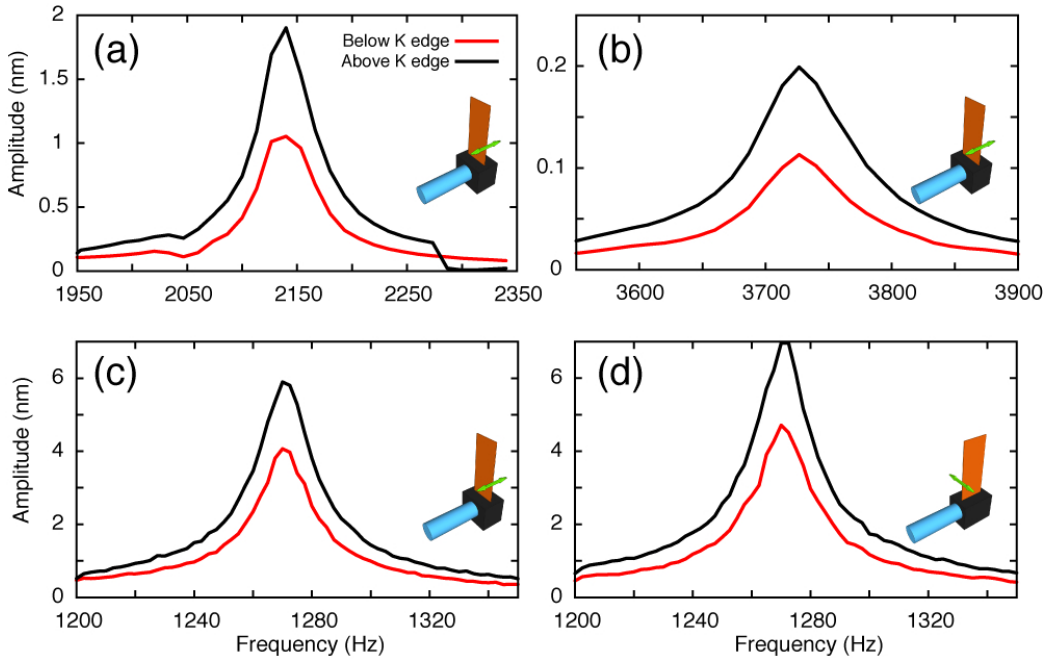

Figure 3.3: Measured resonance curve of the first oscillating mode for all levers. In red the X-ray beam energy is set below the K1s edge (E_{ph} = 11.07keV), in black it is set at the K1s edge (E_{ph} = 11.103keV). (a) Uncoated cantilever ($k = 0.025$ N/m, $Q = 86$, $I_0 = 7.4\,10^{10}$ ph/s) with Ge block glued on the side and X-ray beam parallel to the oscillation direction. (b) Coated cantilever ($k = 0.027$ N/m, $Q = 60$, $I_0 = 3.5\,10^{10}$ ph/s) with Ge block glued on the side and X-ray beam parallel to the oscillation direction. (c) Uncoated cantilever ($k = 0.135$ N/m, $Q = 75$, $I_0 = 2.4\,10^{12}$ ph/s) with Ge block glued below and X-ray beam parallel to the oscillation direction. (d) Same than (c) with X-ray beam perpendicular to the oscillation direction.

3.3.1 X-ray induced mechanical oscillation

Figure 3.3 presents the mechanical response measured around the first resonance frequency ω_0 for different geometries and experimental setups.
In fig 3.3 the intensity of the X-ray beam impacting onto the Ge crystal is modulated at a frequency ω sweeping through the lever resonant frequency ω_0. For X-ray energies below the absorption edge, the lever is already forced to oscillate with amplitudes larger than the thermally induced noise. For energies above the absorption edge we observe an increase of oscillation amplitude for all the geometries.
On the basis of the experimental evidence presented in fig. 3.3, we can identify the oscillation driving force.

Radiation pressure can be ruled out as the oscillation is the same whatever the direction of the beam (figure 3.3(c) and 3.3(d)) with respect to the oscillation direction.
From fig. 3.3 it is evident that the oscillation amplitude is a function of the absorption of the photons by the germanium block. We explored then the hypothesis that the absorbed energy is promptly turned into heat leading to a temperature increase dependent on how the heat is evacuated. Consequently the driving force acting on the microswing should have a thermal origin.

3.3.2 X-ray photons absorbed processes

As a first approximation, the number of photons that contributes to a temperature increase, is the difference between the number of absorbed photons and fluorescence photons that escape from the sample, considering that the fluorescence emission can be photoelectrically reabsorbed. Neglecting the reflectivity, the overall number of photons I_h that induce the temperature increase is then:

$$I_h = I_0(1 - T_{Ge}^E)(1 - w_{Ge}^E T_{w_{Ge}}^{E_f}) \tag{3.3}$$

where I_0 is the incoming intensity, T_{Ge}^E the Ge transmission coefficient, function of the photon energy and sample thickness, and w_{Ge}^E the fluorescence yield. $T_{w_{Ge}}^{E_f}$ is the rate of fluorence at energy E_f which escape from the sample. This last coefficient is dependent on sample thickness.
At energies below the Ge-K edge, the main process is the Auger electron production [60]. Most of the absorbed photons contribute then to the heating because of short mean free path (few nanometer) of the Auger electrons and their cascades. At energies higher than the Ge K edge the absorbed photons generate fluorescence, Coster-Kronig and Auger electrons.
In table 3.1 the absorbed photon flux I_h is calculated for two lever/crystal configurations, for two X-ray beam directions, and for coated and uncoated levers. The ratio of the measured oscillation amplitudes $x(\omega_0)$ above and below K-edge energy is consistent with the ratio of calculated absorbed photons.
This says that the hypothesis of a thermal origin of the interaction X-ray beam - microoscillator is valid.

		$l_0 = 23\mu$m			Uncoated	Coated
E_{ph}	T_{Ge}	w_{Ge}	$T_{w_{Ge}}$	I_h	$x(\omega_0)$ $[nm]$	$x(\omega_0)$ $[nm]$
11.07	0.72	0	-	0.28 I_0	1.053	0.113
11.103	0.083	0.535	0.83	0.51 I_0	1.902	0.199
			Ratio	**1.82**	**1.81**	**1.76**

		$l_0 = 43\mu$m			Paral.	Perp.
E_{ph}	T_{Ge}	w_{Ge}	$T_{w_{Ge}}$	I_h	$x(\omega_0)$	$x(\omega_0)$
11.07	0.54	0	-	0.47 I_0	4.066	4.713
11.103	0.009	0.535	0.33	0.63 I_0	5.898	6.959
			Ratio	**1.34**	**1.47**	**1.48**

Table 3.1: Correspondance between absorbed photon and oscillation amplitude for different levers and geometries. The ratio of the calculated ratio between absorbed photons I_h, in bold in the fifth column, has to be compared with the ratio of the measured oscillation amplitude x_0, in bold in the sixth and seventh columns.

3.3.3 Thermal actuation mechanism: Center Of Mass induced deformation

We want now identify the driving force acting on the cantilever. The first step is the evaluation of the temparature increase induced by the photons absorption. ΔT can be calculated taking into account the overall energy deposited in the crystal and the heat flow through the lever. The absorbed power W is then:

$$W = C\dot{T}(t) + G(T(t) - T_0) \tag{3.4}$$

$$T(t) = T_0 + \frac{W}{G}\left(1 - e^{-\frac{G}{C}t}\right) \tag{3.5}$$

where T_0 is the ambient temperature and $T(t)$ the block temperature as function of time. $\Delta T(\omega)$ is then

$$\Delta T(\omega) = \frac{W}{G}\frac{1}{(1+\omega\tau)} \tag{3.6}$$

$$\tau = \frac{C}{G} \tag{3.7}$$

ω is the beam chopper frequency, τ is the ratio between C, the thermal capacity of the Ge block, and G, the thermal conductivity of the Si lever.

For the uncoated and the coated lever of (fig. 3.3(a) and 3.3(b)) the experimental conditions are nearly identical whereas the oscillation amplitude is 10 times larger in 3.3(a) than in 3.3(b). This difference can be described using those last equations when considering the good values of thermal conductivity (Silicon for the first case and Silicon with a small coating of gold in the second one) and X-ray beam intensity.
However this description cannot explain the difference of the amplitude of oscillation between the (fig. 3.3(a) and 3.3(c)). The oscillation amplitude in fig. 3.3(c) is 3 times larger than in 3.3(a) against a photon flux 40 times bigger and an absorption rate 25% higher because of the difference in Ge-crystal dimensions. The difference in the mechanical properties of the cantilever (3.3(a) $k = 0.025$ N/m, 3.3(c) $k = 0.135$ N/m) cannot explain such a large descrepancy.
So far we have considered only the absorption effect on the temperature of the microswing but we have neglected the MEMS geometry. The position of the Ge crystal and this symmetry with respect to the lever has not been analyzed.
The absorption of the photons in the Germanium block induces an increasing in the Ge crystal size.
In the hypothesis of uniform temperature in the Ge block the displacement of the center of mass (COM) with respect to the lever axis can be calculated using

$$\Delta l(\omega) \quad = \quad l_0 \alpha \Delta T(\omega). \tag{3.8}$$

l_0 is the distance between the block COM and the lever axis and α the linear thermal expansion coefficient.
If the absorption of photons is modulated in frequency, the COM motion is consenquentely modulated at the same frequency. Following the description of the cantilever presented in chapter 2 we have that the cantilever oscillation amplitude is given by

$$x(\omega) = \Delta l(\omega) \sqrt{\frac{\omega_0^2 Q^2}{\frac{Q^2}{\omega_0^2}(\omega^2 - \omega_0^2)^2 + \omega^2}}. \tag{3.9}$$

As it is described in fig 3.4, when the Ge cube is glued on the side of the lever, the thermal expansion induces a COM displacement along the cantilever oscillation direction. This is no more true when the block is welded below the lever in a symmetric configuration; in this case the effective COM desplacement along the lever oscillation direction is negligible. As a consequence, from the expression presented in Eq. 3.9, the oscillation amplitude

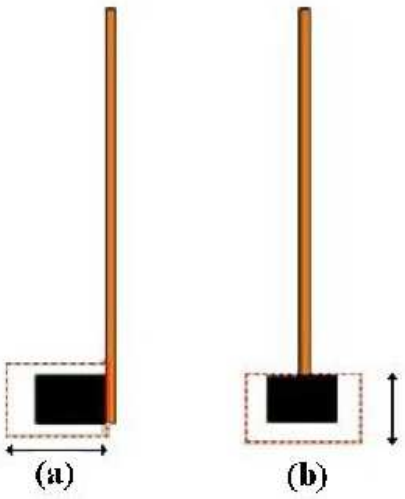

Figure 3.4: Schema of the actuation mechanism. In (a) is presented the very asymmetric configuration and in (b) a symmetric geometry. The dotted squares represent the Ge crystal thermal expansion and the black arrows indicate direction of the effective displacement of the Ge crystal COM.

in the asymmetric configuration is expected to be much more important than in the symmetric one.
For the system in fig. 3.2(c), $l_0 = 13\mu m$ close to half the Ge crystal thickness. For an intensity $I_0 = 7.4\ 10^{10}$ ph/s the temperature increase is found to be $\Delta T(\omega_0) = 0.24\,\mathrm{K}$. Using $\alpha_{Ge} = 5.9\,10^{-6}\,\mathrm{K}^{-1}$, according to equation 3.8, the induced COM displacement is $\Delta l(\omega_0) = 19\,\mathrm{pm}$. Using equation 3.9, with the measured quality factor of 86 and the amplitude at the resonance of 1.9 nm, the COM displacement is found to be $\Delta l(\omega_0) = 22$ pm which is consistent with the value calculated from equation 3.8. The error bar on the measured lever position is determined by the thermal fluctuations of the lever position and is $x_i(k_BT) = 1.6\,\mathrm{pm}$.
The system in fig. 3.2(b) presents a much more symmetrical geometry. l_0 value in this case must be smaller than the one in the case of fig. 3.2(c), but it is not easily measurable. A rough estimate of the residual misalignment between the COM of Ge microcrystal and the Si lever axis is the incertitude in the FIB positioning device that is about 1 μm.
The distance l_0 that best fits the data while all other parameters are known is 1.5 μm which is indeed close to the precision of the FIB motor.
The comparison between the model (equation 3.9) and the measured oscillation is presented in figure 3.5 as the excitation frequency is swept from 100 Hz to 2500 Hz. The agreement further establishes that the thermally

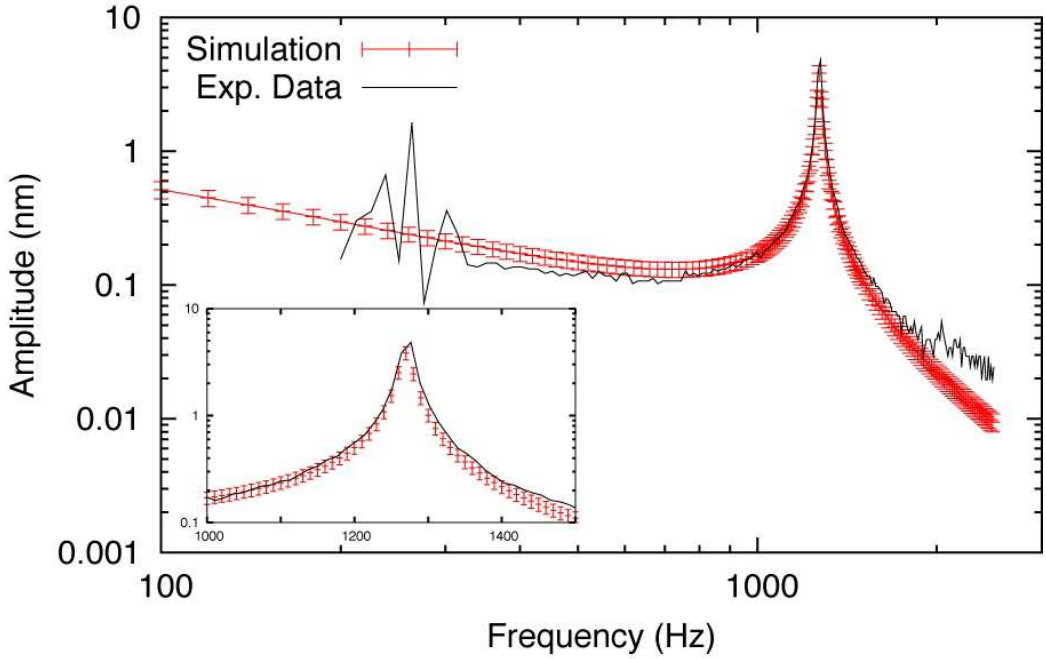

Figure 3.5: Response function of the lever shown in figure 3.2(b). Black curve is the measured amplitude of the lever oscillation as the beam intensity is modulated from 100 to 2500 Hz . Red curve is the calculated expression using experimental parameters. The error bar in red curve has been determined using the Brownian motion. Red curve calculation involves the misalignement of the Ge microcrystal on the Si lever as the single adjustable parameter. In the inset a zoom on the resonant peak is presented.

forced displacement of the COM is at the origin of the observed lever oscillation equiped with the Ge crystal. Results for all configurations are then consistently explained using this single actuation mechanism.

3.3.4 Mechanical detection of germanium EXAFS spectrum

Figure 3.6 reports the mechanical response of the cantilever at the resonance, when the X-ray energy is scanned through the germanium K-edge energy. The mechanical response of the microswing matches well the XAS reference spectrum of germanium [61] . The two curves have been normalised below the edge and in the continuum atomic part above the edge. Even though a mechanical detection of EXAFS has already been shown [62], this is the first time utilising a MEMS.

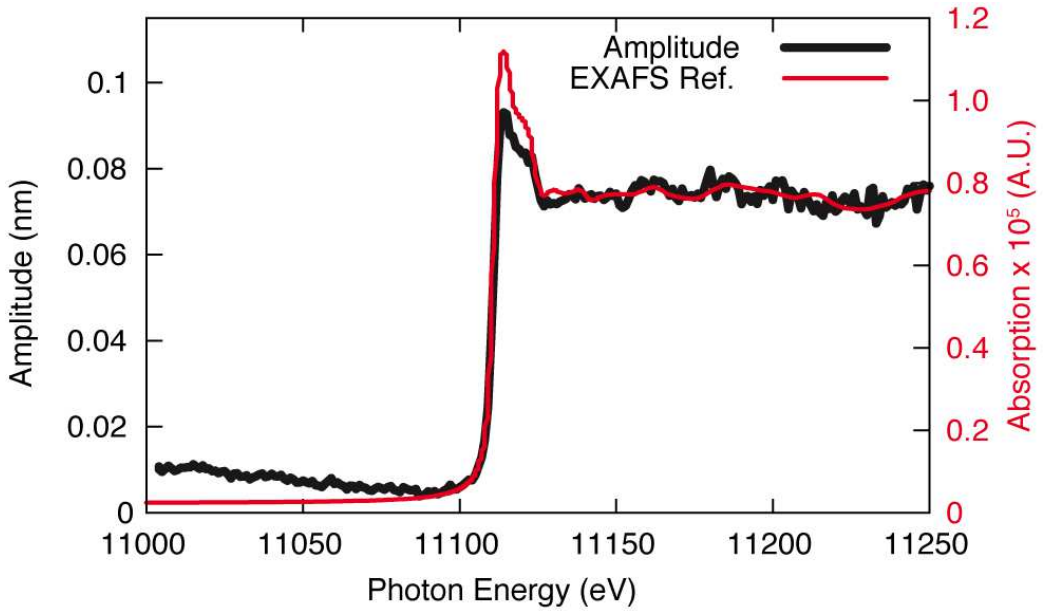

Figure 3.6: Cantilever oscillation amplitude in function of beam energy. We show in black, our experimental data and in red, the handbook reference EXAFS spectrum at Ge K edge.

The decreased amplitude of the XAFS peak and oscillations after the K-edge with respect to the reference spectra are due to the intrinsic self-absorption effect analyzed along the paragraph.
Tuning the energy of the X-ray beam allows to modify in a fully controlled way the oscillation of the cantilever showing that it is possible to tune the interaction between the X-rays and the MEMS as envisaged at the beginning of the chapter.

3.4 MEMS based high frequency X-ray chopper

In this section we show that the interaction MEMS/X-rays can be used to shape a beam. In particular coupling the optical and mechanical properties of a silicon cantilever we show that it is possible to realize a X-ray chopper.
Figure 3.7 shows schematically the experimental set-up. The mechanical system used during the experiment is a standard Si (100) AFM cantilever with dimensions $300 \times 35 \times 2\ \mu m^3$. The cantilever displacement is measured by the interference between the light reflected from the end of a cleaved optical

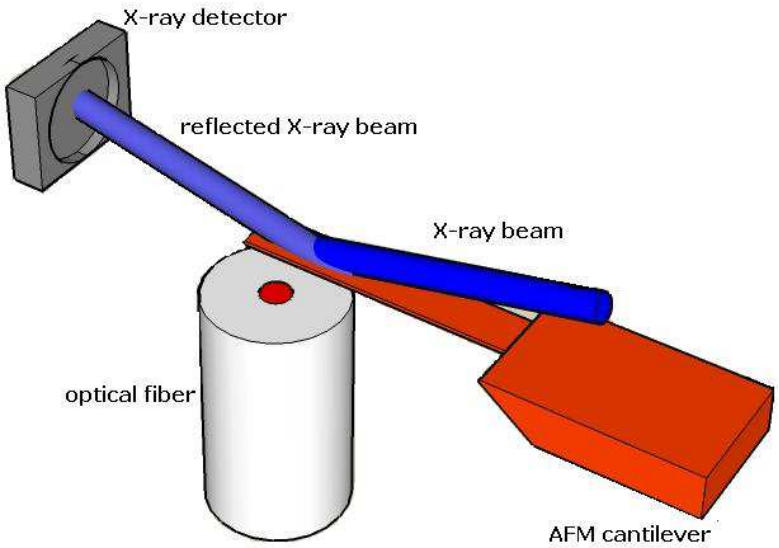

Figure 3.7: Experimental set up. In orange is represented the AFM cantilever used to stop or transmit the dark blue X-ray beam impacting around the Bragg angle. The reflection of the X-ray beam is detected with a photodiode. The white cylinder represents the optical fiber for the interferometric detection of the lever position with sub-Angstrom precision.

fiber and the beam reflected by the back of the lever.
For this particular experiment the beamline involved was the Surface X-Ray Diffraction (SXRD) beamline (ID03). The incoming X-ray beam set at 18.98 keV is impinging on the cantilever at rest at Bragg condition and the X-ray photo detector is positioned at the corresponding 2Θ angle. At the SXRD beamline the photons are tuned in energy with a resolution $\frac{\Delta E}{E} \approx 10^{-4}$. To maintain the photons parallel, in this experiment no lenses have been positioned between the monochromator and the sample. The direct beam from the monochromator at the sample, located 44 m from the photon source, has a size $\approx 50 \times 50\ \mu m^2$ with $\approx 10^{10}\ ph/s$; the beam divergence is $\approx 10^{-4}$ degrees.

3.4.1 Diffracted beam oscillation induced by cantilever periodic motion

When the cantilever is at rest in Bragg conditions , the photodiode detects a constant flux of photon. When the AFM lever is periodically excited by a piezo-electric ceramic, the X-ray incidence angle is consequently modified by the lever motion. If the lever oscillation amplitude is larger than the Bragg

peak width, the cantilever will periodically sweep through the Bragg conditions. A periodically modulated current will be measured at the output of the photodiode.
Fig 3.8 presents the theoretical Bragg peak for a Si (400) reflection, calculated in the hypothesis of perfect $2\mu m$ thick single crystal in kinematic approximation [63, 64]. It is worth to note that due to the small thickness ($2\mu m$) of the Si cantilever with respect to the extintion lenght of the Silicon, the Bragg (400) reflection is very broad. In the case in analysis the Bragg width is $\approx$ 100 times larger than the incoming X-ray beam divergence (10 μrad for divergence Vs 10^3 μrad for Bragg width). The oscillating cantilever is operating as a mechanical chopper on the incoming beam. On the contrary, in the case of Bragg peak sharper than the beam divergence the oscillating cantilever would act more as a monochromator than as a chopper.

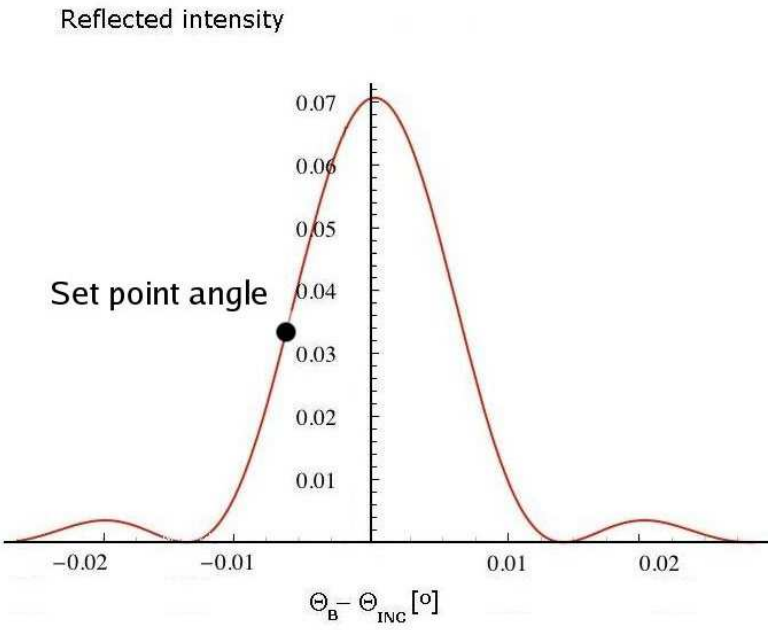

Figure 3.8: Theoretical Si (400) Bragg profile for a 2 μm thick perfect Si crystal in the kinematic approximation. The black dot indicates the flex point used as the reference position of silicon cantilever.

Considering the shape of the Bragg peak, the X-ray intensity modulation is maximum when the set-point angle of the X-rays on the lever is set in correspondence of the flex point of the Bragg peak (see black point in fig. 3.8); in this condition, moreover, the diffracted signal, when the cantilever is oscillating with modulation ω, is modulated at ω and not at 2 ω as it would

be if the set-point is at the maximum of the curve.
The amplitude of the photon flux oscillation is thus directly constrained by the oscillation amplitude of the cantilever.
Reminding what done in chapter 2, we can approximate the lever with a 1D harmonic oscillator whose response to a modulated applied force is given by

$$x(\omega) = \frac{F(\omega)}{\sqrt{m^2\left(\omega_0^2 - \omega^2\right)^2 + \gamma^2\omega^2}} \tag{3.10}$$

$$\tan\phi = \frac{\gamma\omega}{m(\omega_0^2 - \omega^2)} \tag{3.11}$$

where ω is the applied force frequency, ω_0 the oscillator resonant frequency, m the effective mass and γ the system damping factor.
Equation 3.10 gives the lever oscillation amplitude when a modulated force $F(\omega)$ is applied; equation 3.11 gives the phase lag of the cantilever oscillation respect with the applied force.
In fig 3.9(a) are shown the cantilever oscillation amplitude (black) and phase lag (red) as a function of frequency when the mechanical system is mechanically excited at the resonance. This is measured using the optical fiber as shown in fig 3.7.
Fig 3.9 (b) shows the current (amplitude and phase) at the output of the X-ray photodiode as a function of the frequency. For the specific chosen case the current has the same functional shape of the cantilever mechanical response presented in 3.9(a).
This validates the concept of chopper realized with an oscillating microlever. The mechanical oscillation is directly translated in an oscillating X-ray beam detected by the photodiode.

Cantilever profile effect on the diffracted beam oscillations

Figure 3.10 presents the phodiode output as a function of the excitation frequency for different excitation amplitudes. The non linear behavior for the largest cantilever excitation amplitude is due to the cantilever bending induced by the oscillation. In other words, at any given time the X-ray beam does not find a specific incidence angle but an angle gradient over the cantilever.
The angle shift $\Delta\Theta(x)$ induced by the lever deformation at a position x on the lever is

$$\Delta\Theta(x) = \arctan\left(\frac{\partial U_0(x)}{\partial x}\right) \tag{3.12}$$

where $U_0(x)$ is the cantilever first mode profile described in chapter 2.
The calculated diffracted flux of photons is then obtained integrating the

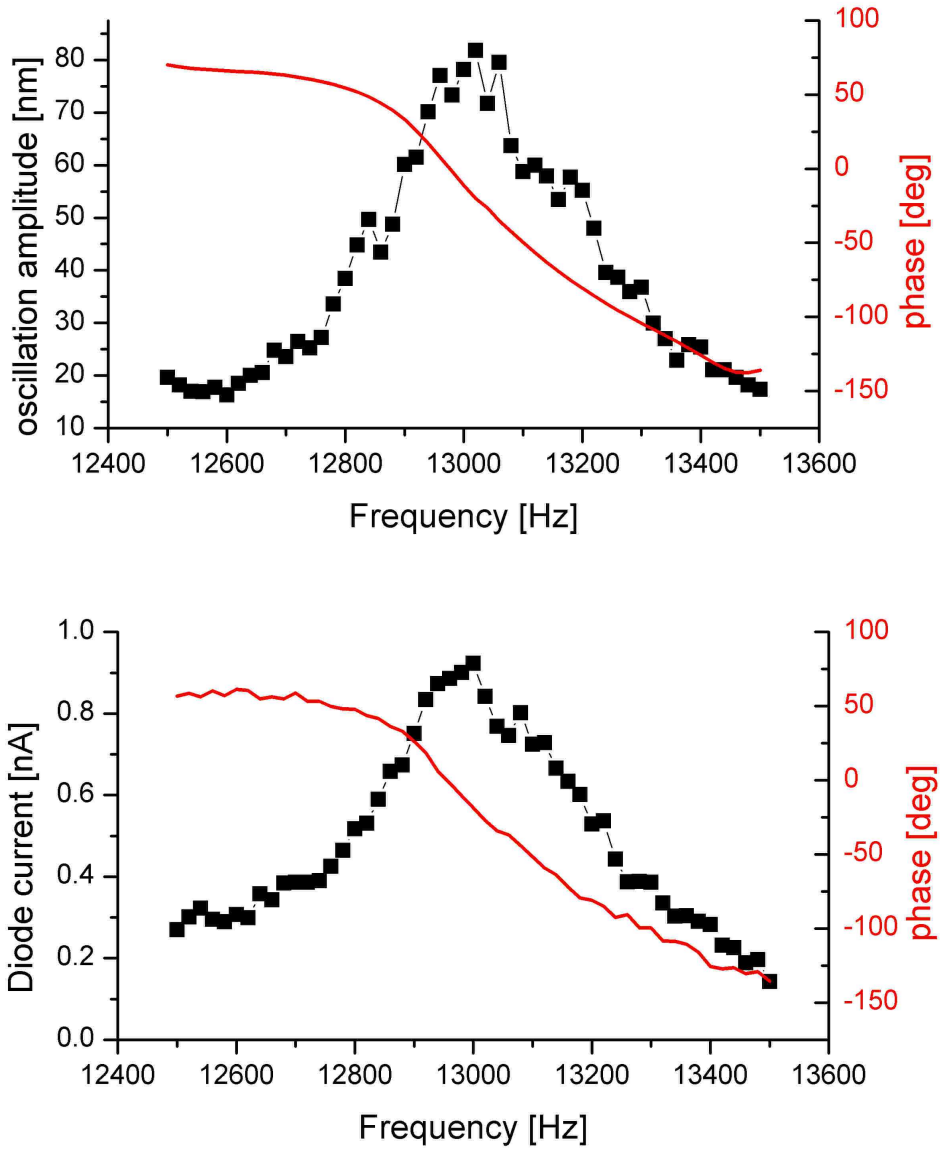

Figure 3.9: (a) Optically measured mechanical response of the AFM cantilever when it is mechanically excited around its first resonant frequency of 13 kHz. (b) Diode photo-current measured by the photodiode at the 2 θ Bragg position. In (a) and (b) the black curve represents the oscillation amplitude and the red curve the phase lag.

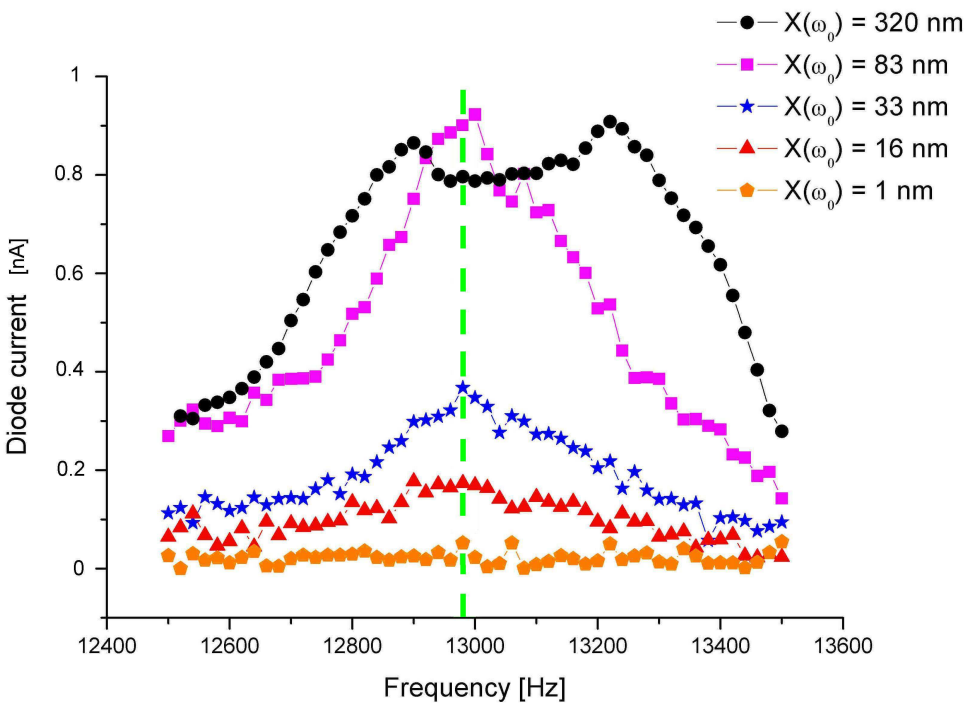

Figure 3.10: Measured photodiode signal as a function of lever's excitation frequency. The different curves refer to different excitation amplitudes as specified by the color code.

Bragg peak profile $B(\Theta(x))$ over all the X-ray effective beam spot size.

$$I_{calc} = \int_0^{L_B} B\left[\Theta_{SP} + \arctan\left(\frac{\partial U_0(x)}{\partial x}\right)\right] dx. \tag{3.13}$$

where Θ_{SP} is the setpoint angle as defined in figure 3.3. The origin, that is the zero position, is experimentally for this specific case the clamped part of the lever. L_B is the irradiated portion of the lever, smaller than the full lever lenght.
The expression $B(\Theta(x))$ used for this calculation leads to the Rocking curve for (400) reflection of a perfect silicon single crystal with 2 μm thickness in kinematic approximation [63, 64]. This theoretical Rocking curve is presented in fig 3.8.
The theoretical estimation of the diffracted signal emitted by the Si lever when it oscillated can be obtained from equation 3.13. Considering the periodic motion of the cantilever around the set-point angle, the expected mod-

ulation of the diffracted beam is given by

$$\begin{aligned} \Delta I_{mod} &= \int_0^{L_B} B\left[\Theta_{SP} + \arctan\left(\frac{\partial U_0(x)}{\partial x}\right)\right] dx \\ &- \int_0^{L_B} B\left[\Theta_{SP} - \arctan\left(\frac{\partial U_0(x)}{\partial x}\right)\right] dx. \end{aligned} \tag{3.14}$$

ΔI_{mod} represents the change in intensity between the two extreme positions of the oscillating lever.
In fig. 3.11 we present the photodiode current as a function of the cantilever oscillation amplitude. This photodiode current measures the full amplitude variation of X-ray intensity produced by the oscillating cantilever excited at the resonance. This photodiode current is in fact the output of the lock-in amplifier that demodulates the instantaneous current variation at the lever resonance frequency.
The mechanical oscillation amplitude is separately measured at the free end through interferometric detection. The blue points represent the photocurrent amplitude measured at the resonant frequency (intersection of the different curves with the green dotted straight line in fig 3.10); the continuous curve is a normalized theoretical prediction from eq. 3.14.
It is interesting to note the shape of the black curve in fig 3.10, representing the measured diffracted amplitude for the largest cantilever oscillation amplitude ($\approx$ 320 nm). This peculiar shape presents two measured symmetric maxima as a function of cantilever oscillation frequency.
This shape is easily explained considering that at resonance the oscillation amplitude reaches the maximum, that given the functional shape of fig. 3.11 gives indeed a local minimum in the lock in output.
The functional shape of the curves (experimental and theoretical) in fig. 3.11, reflects the fact that the modulation of the diffracted signal increases when the mechanical oscillation of the AFM cantilever extends from the set-point at the flex (see definition of flex point in fig 3.8) to include the maximum of the Bragg peak and beyond. For increasing deflections, however the *active* footprint actually diffracting the beam is progressively decreasing, leading to the slow decay of the modulated intensity.

3.5 Conclusions

In the first part of the chapter we have shown that the interactions between MEMS and X-rays can be controlled and tuned. Using the absorption of

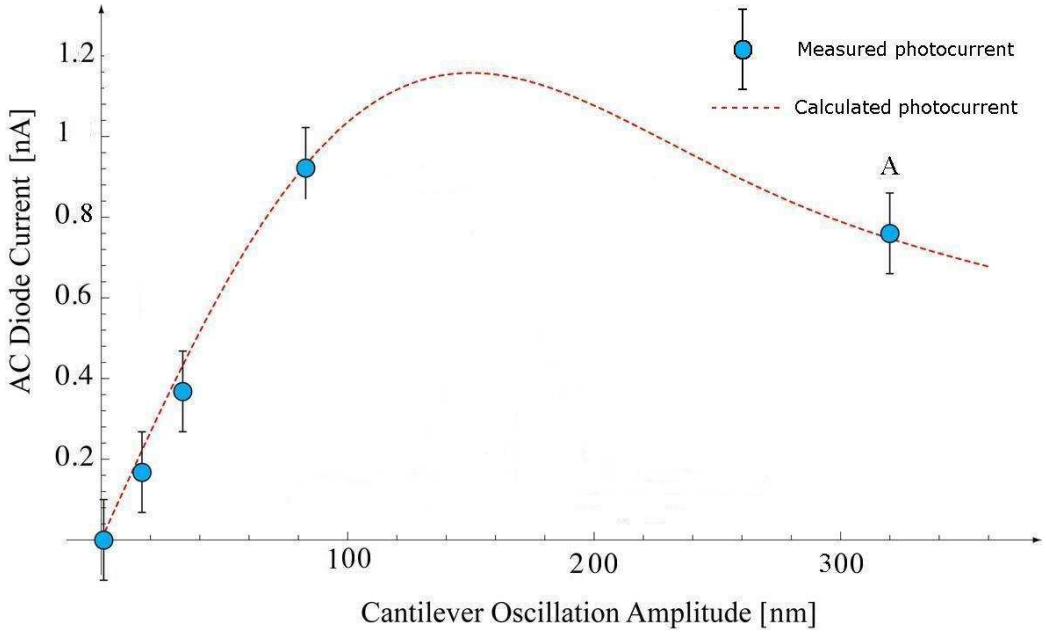

Figure 3.11: Photodiode signal as a function of different cantilever excitation amplitudes. The continuous curve is from equation 3.14 (normalized), while the points represent the experimental data with their error.

an intesity modulated X-ray micro-beam a mechanical oscillator has been excited around the resonant frequency. The actuation mechanism for the MEMS, it has been shown to be the periodic displacement of the center of mass around the equilibrium position.
The MEMS actuation mechanism based on light absorption could be certainly applyed to a NEMS. Considering a Si lever of $1 \times 0.1 \times 0.1$ μm and a Ge block of $100 \times 100 \times 100$ nm with thermal conductivity of $G = 3.7 \cdot 10^{-8}$ W/K and thermal capacity of $C = 1.7 \cdot 10^{-15}$ J/K [65] leads, according to Eq. 3.6, to a substantial temperature increase at a frequency in the MHz regime, typical for the resonance of such a NEMS. If a 1 μW beam is absorbed in this nanometric Ge block, the induced thermal expansion will be several pm. As NEMS with lateral size close to 100 nm can exhibit quality factors of 1000, a forced COM oscillation with amplitude of several pm can result at resonance in a nanometric NEMS oscillation amplitude. This is far above the thermally induced fluctuations of NEMS position. The interaction origin would be a strain-free thermally induced change in mass spatial distribution in asymmetric structure.
In the second part of the chapter we have seen that, using diffraction, Si

single crystal MEMS appear as a good candidate for the high frequency manipulation of X-ray microbeam. This could offer new tools either to change X-ray wavefront, or to rapidly modulate the intensity of X-ray beams that is so important for real time studies of fast dynamical processes in chemistry and in biology [66].
In this chapter we have seen that a standard Si lever can be a fast X-ray chopper. However the curved shape of the lever has been shown to be a limit for an intensity modulation in this set-up. Moreover, during this experiment the X-ray beam spot size was larger than the cantilever width and the diffracted beam detected by the photodiode was consequently less intense than the incoming beam. Rigid silicon single crystal tiles inserted in MEMS would not present these limitations and would maximize the diffracted intensity.
In this experiment the X-ray beam has been chopped at 13 kHz. This moderate operating frequency is related to the resonance frequency of the AFM lever in this proof of concept experiment. The resonance frequency can be easily increased to values much higher then 100 kHz by using others types of cantilever. Specific set-up based on MEMS could be certainly designed so that efficient X-ray choppers could operate at frequency in MHz regime. Considering a simple torsional rigid membrane, ultrafast burst can be realized. A single crystal Silicon square membrane with $10 \times 10 \times 2$ μm^3 can easily achieve a resonant frequency of several hundreds MHz.
The burst duration would be defined as the time that the membrane takes to cover the Bragg peak that is a time much shorter than the full time for a complete oscillation. If the MEMS system is combined with a multilayer deposition technology, the effective reflectivity can be improved and a Bragg peak hundred times sharper than what have been shown in this paper can be produced. A nanometric MEMS oscillation at the resonant frequency (e.g. 400 MHz as shown for a MEMS in [67]) is then translated in a less than a picosecond burst. Furthermore, as already mentioned, the rigid geometry will remove the efficiency limitation discussed in the chapter and the chopped beam will be characterized by pulse with the same shape of the Bragg peak. Therefore the combination of MEMS and NEMS technologies with intense X-ray microbeam, can potentially open a wealth of new experiments based on X-ray examination of time dependent processes requiring high repetition speed.

Transfer thermique radiative à l'échelle nanométrique

La chaleur peut être échangée entre deux surfaces par conduction ou par radiation. Le transfert thermique à l'échelle micro et nano-métrique ne suit pas les lois classiques du transfert radiatif. Quand deux surfaces sont séparées de quelques dizaines à quelques centaines de nanométres, la contribution des effets champ proche ne peut plus être négligée. Dans ce chapitre on analyse le transfert thermique radiatif entre deux surfaces de verre. Pour éviter les problèmes de parrallélisme dans la géométrie plan-plan, on utilise une géométrie sphère-plan. Un modèle théorique couplant la description électromagnétique du transfert thermique avec l'approximation de Derjaguin pour la géométrie sphère-plan a été développée. A la fin du chapitre nous montrerons une comparaison entre les données expérimentales et le modèle théorique.

Chapter 4

Radiative heat transfer at the nanoscale

Contents

4.1 Introduction

Heat can be exchanged between two surfaces through conduction in the separating medium and radiation.
We shall experimentally demonstrate that the thermal transfer at micron and nanoscale does not follow the textbook laws for the energy transfer. When two surfaces are kept at sub-micron separation, in fact, the contribution of the near field components gives rise to important contributions that cannot be neglected.
In the late sixties, the near field contribution to radiative heat transfer between flat metallic surfaces was reported by Domoto at cryogenic temperatures and by Hargreaves at room temperature [68]. In both cases, an increase

of the flux was measured for separation gaps in the micrometer range. A theoretical explanation was given by Polder and Van Hove [69] in the framework of stochastic electrodynamics introduced by Rytov [70] few years before.
The proposed theory accounts for electromagnetic fluctuations, both quantum and thermodynamic, and it has been successfully applied also to model Casimir forces [71].
Although significant progresses have been made in the past on the precise measurement of the Casimir force [9, 10, 11, 12, 13], a detailed quantitative comparison between theory and experiments in the nanometer regime is still lacking when speaking about heat transfer. The first attempt to detect quantitatively the heat transfer for sub-micron gaps was reported by Xu et al. [72] but was inconclusive. More recently, it has been demonstrated unambiguously that heat transfer increases as the distance decreases in the sub-micron range [73, 74]. The heat transfer has been studied between a gold coated scanning tunneling microscope (STM) and a plate of gold or GaN. Unfortunately, the geometry of the experiment was too complex to allow a quantitative comparison with theory.
In this chapter we analyze the radiative heat transfer betwen two surfaces of glass. After a description of radiative transfer in the framework of stochastic electrodynamics, we present measurements of heat transfer between surfaces at the nanometer scale.
To avoid parallelism difficulties in the plane-plane geometry, we use a sphere-plane geometry as for recent Casimir force measurement [10, 11, 12, 13]. A theoretical model for the sphere-plane geometry have been developed starting from the Derjaguin approximation [21], as used for the Casimir force formulation in sphere-plane geometry. Justification of this procedure will be shown here to be somewhat delicate.

4.2 Radiative heat transfer

For a standard macroscopic system the thermal radiation can be treated using Planck's law and Stefan's law. These two fundamental laws allow the evaluation of the intensity emitted by a body at temperature T.
For the case of a black body (*i. e.* object that absorbs all the incidence radiation, no matter the radiation wavelength, incidence angle or polarization), the Planck's law gives the monochromatic emitted intensity as a function of the body temperature T:

$$I_\omega^0(T) = \frac{\hbar\omega^3}{4\pi^3 c^2} \frac{1}{e^{\frac{\hbar\omega}{k_B T}} - 1} \tag{4.1}$$

where $\hbar = 1.054 \cdot 10^{-34}\ J \cdot s$ is the Planck's constant, $c = 2.99 \cdot 10^{8} m/s$ the speed of light and $k_B = 1.38 \cdot 10^{-23}\ J/K$ the Boltzmann's constant.
The Stefan's law gives the total intensity emitted by a black body at the temperature T:

$$I^0(T) = \frac{\sigma T^4}{\pi} \tag{4.2}$$

where $\sigma = 5.67 \cdot 10^{-8}\ W \cdot m^{-2} \cdot sr{-}1 \cdot K^{-4}$ is the Stefan's constant.
The evaluation for real body can be obtained taking into account the directional monochromatic emissivity of the body $\varepsilon(T, \omega, \theta, \phi, polarization)$. The monochromatic emitted intensity is then given by

$$I_\omega^{real}(T) = \varepsilon(T, \omega, \theta, \phi, polarization) I_\omega^0(T). \tag{4.3}$$

This formalism is good for the analysis of a macroscopic system but it fails in the description of micro and sub-micro systems. In the second case, a reliable theory can be obtained in the framework of the classical electrodynamics. It will be possible to calculate the energy density emitted by a thermal source and consequently the heat transfer between two surfaces, in the general case only knowing the material dielectric constant.

4.2.1 Electromagnetic treatment of the problem

Let us consider a material body at temperature $T > 0\ K$. The temperature fluctuations around the equilibrium induce a movement of the constituent electrons, creating, as a consequence, an electric current that irradiates an electromagnetic field. If we consider a volume element of the body dV around the position $\vec{r}$, we can write the fluctuating current at the frequency ω as $\vec{j}^f(\vec{r}, \omega)$. Introducing such fluctuating sources in the problem and in the Maxwell equations, allows to study the thermal radiation in the framework of the classical electromagnetism.

Electromagnetic field generated by fluctuating sources

The fluctuating currents have a zero first order momentum. The second order momentum, formally equal to the correlation function of the currents, is not null and it is given by the fluctuation dissipation theorem.
We consider now a non-magnetic material described, from an electromagnetic point of view, by its complex dielectric constant $\epsilon(\omega) = \epsilon'(\omega) + i\epsilon''(\omega)$. The material is supposed to be in a local thermodynamic equilibrium, *i. e.* it is possible to define a local equilibrium temperature T. In this approximation

we consider two current elements $\vec{j}^f(\vec{r},\omega)$ and $\vec{j}^f(\vec{r'},\omega')$. According to the fluctuation-dissipation theorem the correlation function of the two elements is given by [75]:

$$\langle j_m^f(\vec{r},\omega) j_n^f(\vec{r'},\omega')^* \rangle = \frac{2\omega\epsilon_0}{\pi}\epsilon''\Theta(\omega,T)\delta_{m,n}\delta(\vec{r}-\vec{r'})\delta(\omega-\omega') \tag{4.4}$$

where the index $m,n = x,y,z$ are the different spatial components of the currents, ϵ_0 the vacuum dielectric permittivity and $\epsilon''(\omega)$ the imaginary part of the medium dielectric constant. $\Theta(\omega,T)$ is the average energy of a quantum harmonic oscillator at pulsation ω and temperature T.
From equation 4.4 we note that knowing the dielectric constant, one can determine radiation of the medium in the space. Starting from this equation we can evaluate the electromagnetic field linked to the thermal radiation.
The electromagnetic problem that we have to solve, is the way to link the fluctuating currents $\vec{j}^f(\vec{r},\omega)$ to the electromagnetic field represented by the $\vec{E}(\vec{r},\omega)$ and $\vec{H}(\vec{r},\omega)$. In the hypothesis of linear, homogeneous and non-magnetic medium, following the linearity of the Maxwell's equations, we have a linear relation between the currents and the fields. The Green's formalism allows to write the correct relation. Let us consider an element of punctual current $\vec{j}^f(\vec{r'},\omega)$ at the position $\vec{r'}$, and at the pulsation ω; the electromagnetic field irradiated at position $\vec{r}$ oscillating at pulsation ω is given by:

$$\begin{aligned} \vec{E}(\vec{r},\omega) &= i\omega\mu_0 \mathbf{G}^E(\vec{r},\vec{r'},\omega)\cdot\vec{j}^f(\vec{r'},\omega) \\ \vec{H}(\vec{r},\omega) &= \mathbf{G}^H(\vec{r},\vec{r'},\omega)\cdot\vec{j}^f(\vec{r'},\omega) \end{aligned} \tag{4.5}$$

where $\mathbf{G}^E$ and $\mathbf{G}^H$ are the Green's tensor for the electric and magnetic field respectively. These tensors represent the propagation of fields with pulsation ω, from $\vec{r'}$ to $\vec{r}$. All the informations about the geometry and electromagnetic properties of the system are given by these two tensors. This definition is the most general possible for the treatment of the electromagnetic radiation problems.

Energy density above an interface

We evaluate now the electromagnetic energy density above a flat interface. We consider, here, that the space is divided in two semi-infinite parts: for $z<0$ the medium is a material characterized by its dielectric constant $\epsilon(\omega)$ and by a constant temperature $T>0$; for $z>0$ there is the vacuum ($\epsilon=1$). A point in the space is defined by $\vec{r}=(\vec{R},z)=(x,y,z)$ (fig. 4.1).
The substrate is at a temperature $T>0$. Let us indicate with $\vec{j}^f(\vec{r'},\omega)$ the

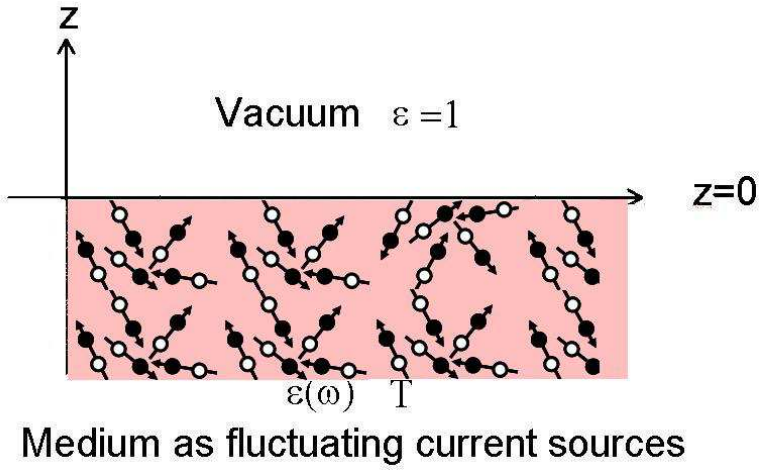

Figure 4.1: Geometry of the system analyzed.

volume current density generated at $\vec{r'}$ with the pulsation ω. These currents irradiate an electromagnetic field $\vec{E}(\vec{r},\omega)$, $\vec{H}(\vec{r},\omega)$.
We denote with $u(\vec{r},\omega,T)$ the electromagnetic energy density given by[1]:

$$u(\vec{r},\omega,T) = 2 \times \left[\frac{\epsilon_0}{2}\langle \vec{E}(\vec{r},\omega)\cdot\vec{E}(\vec{r},\omega)^*\rangle + \frac{\mu_0}{2}\langle \vec{H}(\vec{r},\omega)\cdot\vec{H}(\vec{r},\omega)^*\rangle\right] \quad (4.6)$$

where we can see two different contributions, the electric part

$$u_e(\vec{r},\omega,T) = 2 \times \frac{\epsilon_0}{2}\langle \vec{E}(\vec{r},\omega)\cdot\vec{E}(\vec{r},\omega)^*\rangle \quad (4.7)$$

and the magnetic part

$$u_m(\vec{r},\omega,T) = 2 \times \frac{\mu_0}{2}\langle \vec{H}(\vec{r},\omega)\cdot\vec{H}(\vec{r},\omega)^*\rangle. \quad (4.8)$$

The total energy density can be calculating integrating equation 4.6 over the all spectrum

$$u(\vec{r},T) = \int_0^\infty d\omega\ u(\vec{r},\omega,T). \quad (4.9)$$

According to 4.4 and 4.5 we have

$$\begin{aligned}\langle \vec{E}(\vec{r},\omega)\cdot\vec{E}(\vec{r},\omega)^*\rangle &= \mu_0^2\omega^2\int_V d^3r'\int_V d^3r''\mathbf{G}^E(\vec{r},\vec{r'},\omega)\mathbf{G}^E(\vec{r},\vec{r''},\omega)^* \\ &\times \langle j_m^f(\vec{r'},\omega)j_n^f(\vec{r''},\omega')^*\rangle \\ = \frac{2\omega^3\epsilon_0\mu_0^2}{\pi}\epsilon''(\omega)\Theta(\omega,T)\delta_{m,n} &\times \int_V d^3r'\mathbf{G}^E(\vec{r},\vec{r'},\omega)\mathbf{G}^E(\vec{r},\vec{r'},\omega)^* \quad (4.10)\end{aligned}$$

[1]The factor 2 in equation 4.6 is due to the fact we are working with analytical signals.

and

$$\begin{aligned}\langle \vec{H}(\vec{r},\omega)\cdot\vec{H}(\vec{r},\omega)^*\rangle &= \int_V d^3r' \int_V d^3r'' \mathbf{G}^H(\vec{r},\vec{r'},\omega)\mathbf{G}^H(\vec{r},\vec{r''},\omega)^* \\ &\times \langle j_m^f(\vec{r'},\omega) j_n^f(\vec{r''},\omega')^*\rangle \\ = \frac{2\omega\epsilon_0}{\pi}\epsilon''(\omega)\Theta(\omega,T)\delta_{m,n} &\times \int_V d^3r' \mathbf{G}^H(\vec{r},\vec{r'},\omega)\mathbf{G}^H(\vec{r},\vec{r'},\omega)^*. \end{aligned} \quad (4.11)$$

An exhaustive description of the solution for equations 4.10 and 4.11 it is clearly not our objective in this experimental thesis and it can be found in [75]. The solution is based on the development in plane waves of the electromagnetic field:

$$\begin{aligned}\vec{E}(\vec{r},\omega) &= \int \frac{d^3k}{(2\pi)^3}\hat{\vec{E}}(\vec{k},\omega)e^{i\vec{k}\cdot\vec{r}} \\ \vec{H}(\vec{r},\omega) &= \int \frac{d^3k}{(2\pi)^3}\hat{\vec{H}}(\vec{k},\omega)e^{i\vec{k}\cdot\vec{r}}. \end{aligned} \quad (4.12)$$

Here $\hat{\vec{E}}(\vec{k},\omega)$, $\hat{\vec{H}}(\vec{k},\omega)$ are the amplitudes of a plane wave with wave vector $\vec{k} = (\vec{K},\gamma)$. $\vec{K}$ represents the component of the wave vector parallel to the the interface while γ the component perpendicular to the interface.
$\vec{k}$, $\vec{K}$ and γ are linked together by a simple relation

$$\begin{aligned}\gamma_0^2 &= k_0^2 - K^2 \\ \gamma^2 &= k_0^2\epsilon - K^2 \end{aligned} \quad (4.13)$$

where $k_0 = \omega/c$ is the wave vector modulus of a plane wave in the vacuum. The first expression gives the wave vector component in vacuum while the second one in the medium. Looking to equations 4.12 and 4.13 we note that if $\gamma_0^2 < 0$ (respectively γ^2) the electromagnetic field is characterized by an evanescent wave in the z-direction, exponentially decaying with z. On the contrary if $\gamma_0^2 > 0$ (respectively γ^2) the electromagnetic field is characterized by a propagative wave in the z-direction.
Taking into account this description, the solution for the monochromatic energy density, calculated in the vacuum at distance z over the interface, is found to be (see ref [75] for more details)

$$\begin{aligned}u^{prop}(z,\omega,T) &= \frac{\omega^2\Theta(\omega,T)}{\pi^2c^3}\int_0^{k_0}\frac{KdK}{k_0|\gamma_0|}\frac{1}{2}\left[\left(1-|r_s|^2\right)+\left(1-|r_p|^2\right)\right] \\ u^{evan}(z,\omega,T) &= \frac{4\omega^2\Theta(\omega,T)}{\pi^2c^3}\int_{k_0}^{\infty}\frac{K^3dK}{k_0^3|\gamma_0|}\frac{1}{2}\left[Im(r_s)+Im(r_p)\right]e^{-2Im(\gamma)z} \\ u(z,\omega,T) &= u^{prop}(z,\omega,T)+u^{evan}(z,\omega,T). \end{aligned} \quad (4.14)$$

where r_s and r_p are the Fresnel reflection coefficients for a incidence plane wave polarized s or p. In equation 4.14 we can clearly see that the energy density has two contributions, one that is propagative and not attenuated with the vertical distance from the interface, and one that is evanescent and strongly attenuated with the distance. The presence of this second contribution is the most important result of the electromagnetic treatment of thermal radiation.

Radiation transfer between two surfaces

We consider now the system as shown in figure 4.2. The space is divided in three parts. The first medium, filling the space for $z < 0$, is characterized by a dielectric constant $\epsilon_1(\omega)$ and by a uniform temperature T_1. The second medium, filling the space for $z > d$, is characterized by a dielectric constant $\epsilon_2(\omega)$ and by a uniform temperature T_2. Between them we suppose there is vacuum ($\epsilon = 1$).

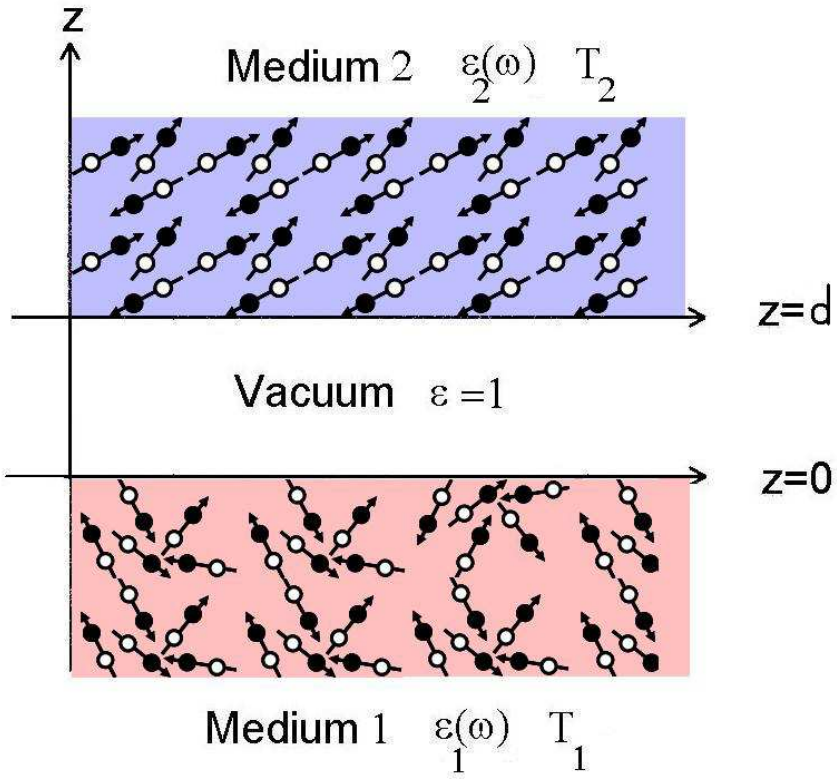

Figure 4.2: Geometry of the system analyzed.

The two media are at a temperature T_1 and T_2, then they exchange en-

ergy through thermal radiation. Fluctuating currents in medium 1 irradiate an electromagnetic field everywhere in the space and clearly also inside the medium 2, where the field is absorbed through Joule effect. The same thing happens on the other direction. A electromagnetic quantity that can describe such energy transfer is the Poynting vector $\langle \mathbf{\Pi} \rangle$. The Poyinting vector represents the energy flux crossing a surface per time.
The Poynting average value is defined to be[2]

$$\langle \vec{\Pi}(\vec{r}, \omega) \rangle = 4 \times \left[\frac{1}{2} \langle Re(\vec{E}(\vec{r}, \omega) \times \vec{H}^*(\vec{r}, \omega)) \rangle \right] \tag{4.15}$$

where $\vec{E}(\vec{r}, \omega))$ and $\vec{H}(\vec{r}, \omega))$ are the electric and magnetic fields generated by fluctuating currents.
In the particular geometry analyzed we are interested only in the z-component of the vector Π_z. Considering the two directions, the net energy exchange can be deduced from the flux difference between the two surfaces, indicated as $P(d, \omega, T_1, T_2) = \langle \Pi_z(d, \omega) \rangle - \langle \Pi_z(0, \omega) \rangle$, where the dependence by the two different temperatures T_1 and T_2 has been clearly expressed.
A useful quantity that can be defined for the analysis of the thermal exchange is the *monochromatic radiative transfer coefficient*

$$h_\omega(d, T_1) = \lim_{T_2 \to T_1} \frac{P(d, \omega, T_1, T_2)}{T_2 - T_1} \tag{4.16}$$

that integrated over the whole spectrum gives a total radiative transfer coefficient

$$h(d, T) = \int_0^\infty d\omega h_\omega(d, T), \tag{4.17}$$

so that the exchanged net energy flux per surface between two media with temperature difference ΔT is given by

$$\Delta\Phi = h(d, T)\Delta T. \tag{4.18}$$

The monochromatic radiative transfer coefficient can be evaluated following the procedure presented for the calculation of the energy density above an interface, starting by the definition of the Poynting vector as in eq. 4.15. The full solution can be found in [75]; here we report only the result. The

[2]The factor 4 in equation 4.15 is due to the fact we are working with analytical signals.

radiative coefficient for a temperature T and at a distance d is given by:

$$
\begin{aligned}
h_\omega(d,T) &= \\
= \pi\frac{\partial I^0_\omega}{\partial T}(T) &\times \left\{\int_0^{k_0}\frac{KdK}{k_0^2}\left[\frac{(1-|r^s_{31}|)^2(1-|r^s_{32}|)^2}{\left|1-r^s_{31}r^s_{32}e^{2i\gamma'_3 d}\right|^2}+\frac{(1-|r^p_{31}|)^2(1-|r^p_{32}|)^2}{\left|1-r^p_{31}r^p_{32}e^{2i\gamma'_3 d}\right|^2}\right]\right\} \\
+\pi\frac{\partial I^0_\omega}{\partial T}(T) &\times \left\{\int_{k_0}^{\infty}\frac{KdK}{k_0^2}\left[\frac{4Im(r^s_{31})Im(r^s_{32})}{\left|1-r^s_{31}r^s_{32}e^{2\gamma''_3 d}\right|^2}+\frac{4Im(r^p_{31})Im(r^p_{32})}{\left|1-r^p_{31}r^p_{32}e^{2\gamma''_3 d}\right|^2}\right]\right\}
\end{aligned}
\tag{4.19}
$$

where I^0_ω is the intensity emitted by a black body as defined in equation 4.1, $k_0 = \omega/c$ and $r^{s,p}_{31,32}$ the Fresnel reflection coefficient at the interface vacuum/medium 1 (r_{31}) and vacuum/medium 2 (r_{32}) in polarization s or p. γ'_3 and γ''_3 are the real and imaginary part of z component (γ_3) of the wave vector for a plane wave in the vacuum between the two media.
In equation 4.19 we have separated the case when γ_3 is real and when is imaginary. Looking to equation 4.13, we can note that:

- $0 \leq K \leq k_0$, γ_3 is real and the electromagnetic wave is propagating in vacuum without attenuation with the distance in z;
- $K > k_0$, γ_3 is imaginary and the electromagnetic wave is purely evanescent with strong attenuation with the distance in z.

We can see that the radiative coefficient has two contributions, one propagative and one evanescent. The propagative term is not depending by the distance and it gives the Stephan's law for the radiative transfer.
The second term is the evanescent contribution to the radiative heat transfer that is strongly dependent by the distance. This term is the major result of the electromagnetic treatment of the radiative transfer.

4.2.2 Surface waves contribution

The expression of the energy density (equation 4.14) and radiative transfer coefficient (equation 4.17) is valid for all the materials. Knowing the dielectric constant of the material, it is possible to evaluate the emitted energy above a flat surface, or the energy exchange between two flat surfaces.
From a technological point of view, it would be interesting to analyze the case of diatomic materials. Members of this family are Silicon Carbide (SiC) glass (SiO_2), Gallium Arsenide (ArGa) and doped Silicon.
The dielectric constant can be obtained by a microscopic treatment of the matter within the Lorentz model for the description of diatomic materials.
Diatomic material is characterized by two different kinds of elastic vibrations

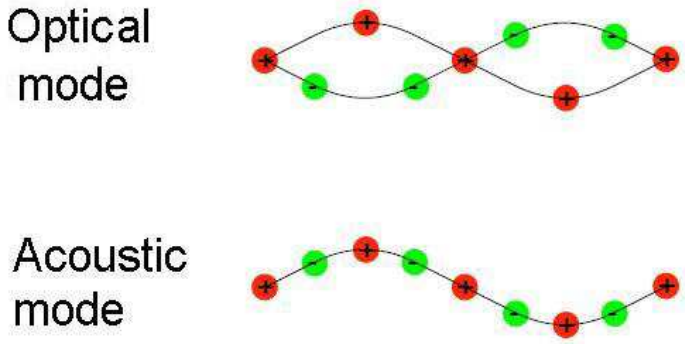

Figure 4.3: Vibrational mode of the lattice for a diatomic material

of the lattice as presented in figure 4.3.
The optical mode have a not null dipolar momentum and it can be coupled with an electric field with the appropriate frequency and wave vector; such coupling is called polariton. The behavior of diatomic material when excited by an electromagnetic field can be described by a dielectric function $\epsilon(\omega)$ calculated within the so called *oscillator model*:

$$\epsilon(\omega) = \epsilon_\infty \left[1 + \frac{\omega_L^2 - \omega_T^2}{\omega_T^2 - \omega^2 - i\Gamma\omega}\right] \tag{4.20}$$

where ϵ_∞ represents the contribution of the crystal lattice to the polarization, while ω_L and ω_T are characteristic parameters of the material in analysis, representing, respectively, the frequency of longitudinal optical phonons with zero wave vector, and the frequency of transverse optical phonons with large wave vector.
Such dielectric costant leads to a reflectivity as presented in figure 4.4.
Between ω_T and ω_L the reflectivity is closed to 1, meaning that there is no propagation of electric field inside the bulk material. In this gap we observe no coupling between elastic vibration of the lattice and electric field.
Very closed to an interface vacuum-material a diatomic material present a surface wave due to a polariton exponentially decaying with the distance from the interface. The surface polariton is characterized by a resonance in the infrared regime. Such electromagnetic wave are analytically described by the imaginary part of the dielectric function $\epsilon(\omega)$ (see fig 4.5).
Volume and surface polaritons should slightly modify the energy density above a surface and the radiative transfer coefficient.
Figure 4.6 represents the electromagnetic energy density above a flat interface

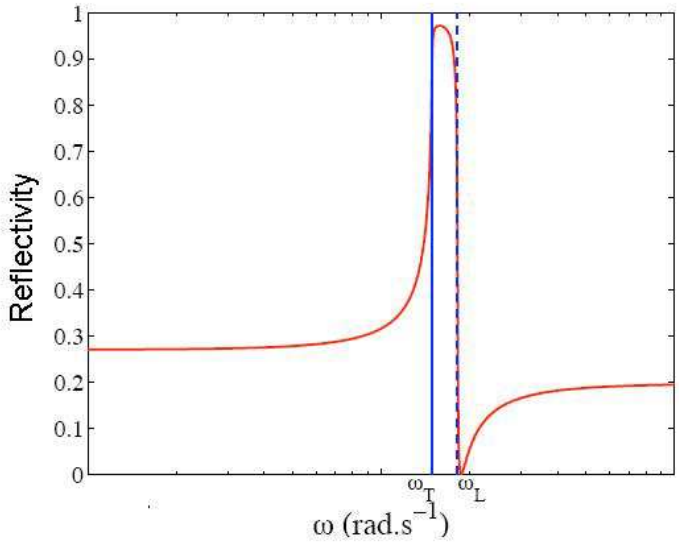

Figure 4.4: Reflectivity for a diatomic material as a function of the frequency

of SiC, at temperature $T = 300\ K$ as a function of the distance z from the interface. We can see that for distances larger then 10 μm the energy density is constant. This correspond to the far-field regime where the propagative contribution is the main term for the energy density. For distances smaller then 10 μm an enhancement of the emitted energy is observed. This is the evanescent contribution to the energy density. An asymptotic expression of equation 4.14 can be obtained for small distances:

$$u^{tot}(z,\omega,T) \approx u^{evan}(z,\omega,T) \approx \frac{1}{8\pi^2\omega z^3} Im\left(\frac{\epsilon-1}{\epsilon+1}\right)\Theta(\omega,T). \qquad (4.21)$$

It is worth to note that the nature of the energy density in the far-field is different from that in near-field. As shown in figure 4.7 the far-field regime is similar to the black body emission spectrum (modulated by the material emissivity), while the near-field is quasi-monochromatic. This is the signature of the electromagnetic surface wave resonance.
We can now analyze the radiative transfer coefficient around a temperature $T = 300\ K$ (fig. 4.8).
As for the energy density, we see an enhancement effect for separation gaps smaller then 10 μm. This corresponds, again, to the evanescent contribution. The difference between the SiC and the glass is due to the difference of the surface resonance parameters. However, independently on the material, where the evanescent contribution is dominant the radiative transfer coefficient diverges as $1/d^2$.

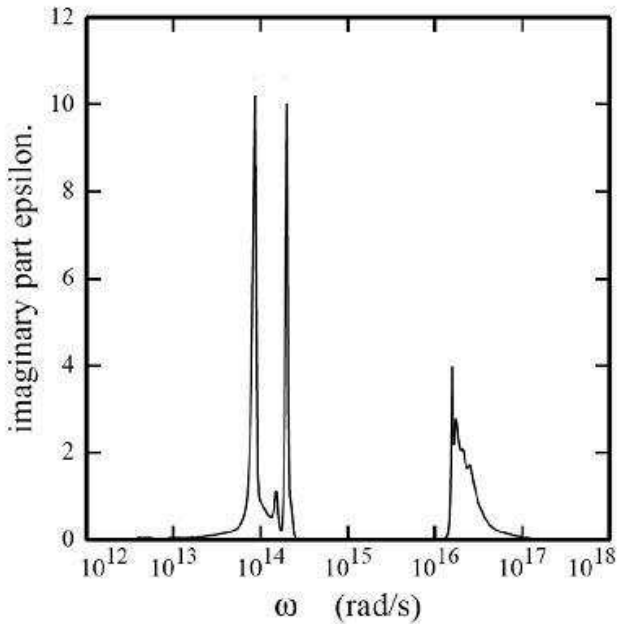

Figure 4.5: Imaginary part of the dielectric function for a diatomic material (glass in this case)

The radiative heat transfer at nanometer scale is then much more important than what predicted by the the Planck's law of radiation. For the far-field regime, where only the propagative contribution is present, the Planck's law reproduces well the radiation transfer; in near-field regime, where the evanescent contribution is dominant, the Planck's law fails. This failing is moreover quite important. At 100 nm, as shown in figure 4.8, the energy transfer is two orders of magnitude larger than the far-field value.
For the further development of nano scale devices, the radiative heat transfer has to be analyzed in the framework of the classical electrodynamic.

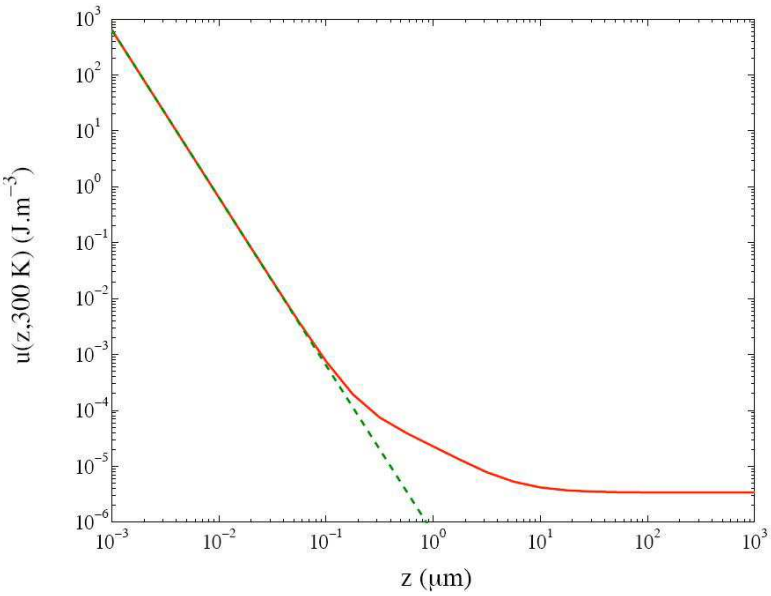

Figure 4.6: Electromagnetic energy density above a flat interface of SiC

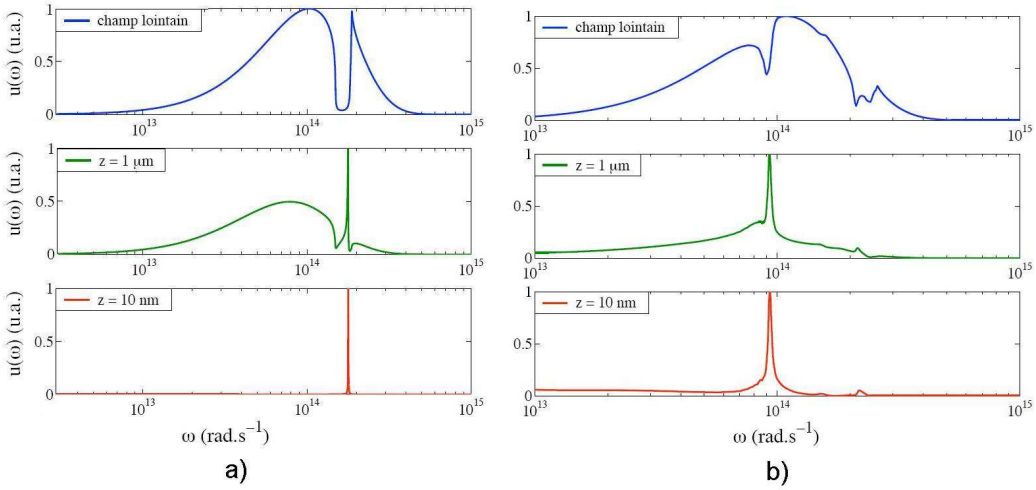

Figure 4.7: Monochromatic electromagnetic energy density above a flat interface of SiC (a) and SiO_2 (b), for different distances from the interface.

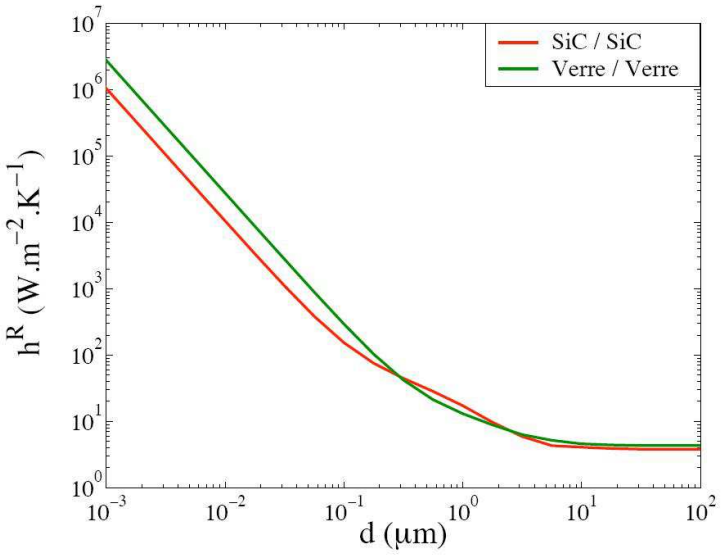

Figure 4.8: Total radiative transfer coefficient between two flat interfaces of SiC, and two interfaces of glass.

4.2.3 Derjaguin approximation for radiative heat transfer

The electromagnetic treatment of the radiative transfer coefficient describes very well the case of transfer between two plane surfaces. A model for different geometries can be evaluated following the same procedure here presented. For an asymmetric geometry an analytical solution has not been yet developed. However if we consider the case of sphere-plane geometry we could use the Derjaguin approximation [21], as already done for the formulation of the Casimir force between a sphere and a plane.
The Derjaguin approximation [21] for the radiative heat transfer consists essentially to locally describe the flux between the sphere and the plate as a flux between two parallel plates separated by a distance d using the heat transfer coefficient h(d, T) derived numerically [76, 77] (see fig 4.10). Note that $h(d, T)$ accounts for both near-field and far-field contributions [76, 78, 79]. We integrate over the whole area to obtain the theoretical conductance:

$$G_{theo}(d, T) = \int_0^R h[d(r), T] 2\pi r \; dr \tag{4.22}$$

where R is the radius of the sphere and $d(r) = d + R - \sqrt{R^2 - r^2}$ is the local distance between the plane and the sphere surface.

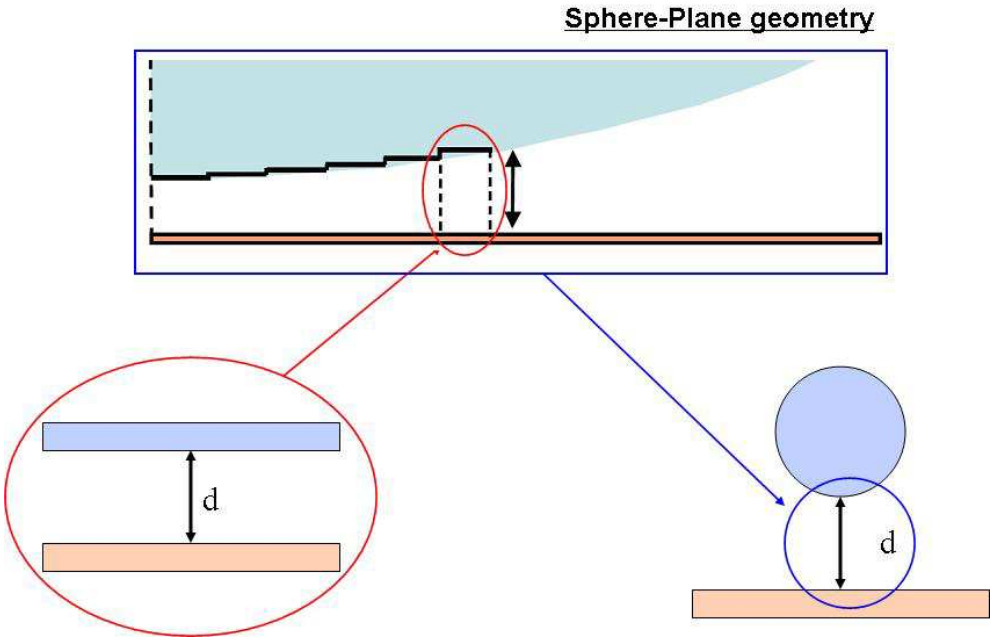

Figure 4.9: Derjaguin approximation for the radiative heat transfer.

For two infinite planes and for distances smaller than $d = 500\ nm$, the flux increases as $1/d^2$ in the short distance regime. If we retain only this asymptotic near-field contribution and integrate over the sphere surface, we find a $1/d$ behavior for the conductance. The theoretical conductance versus the sphere-plate distance is displayed in Fig. 4.10. It is clearly seen that the conductance strongly deviates from the $1/d$ law for distances larger than $10\ nm$.
This approach does not account for Mie resonances of the sphere. This is an excellent approximation so far the coherence length [80] along the surface and decay length in the medium are much smaller than the sphere radius. For wavelengths corresponding to silica resonances ($20\ \mu m$ and $8.5\ \mu m$), coherence and decay lengths are smaller than $1\ \mu m$ (fig 4.11).

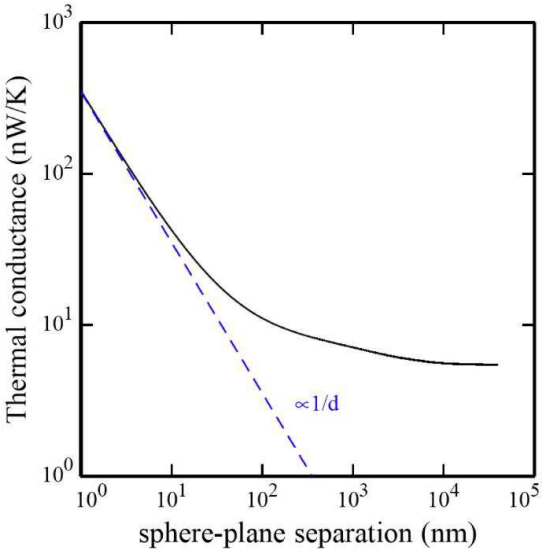

Figure 4.10: Theoretical thermal conductance between a silica sphere and a silica plane using the Derjaguin approximation. A $1/d$ regime, characteristic of the near-field contribution, is observed for distances smaller than 10 nm. The conductance tends to the far-field constant value for distances larger than 10 μm.

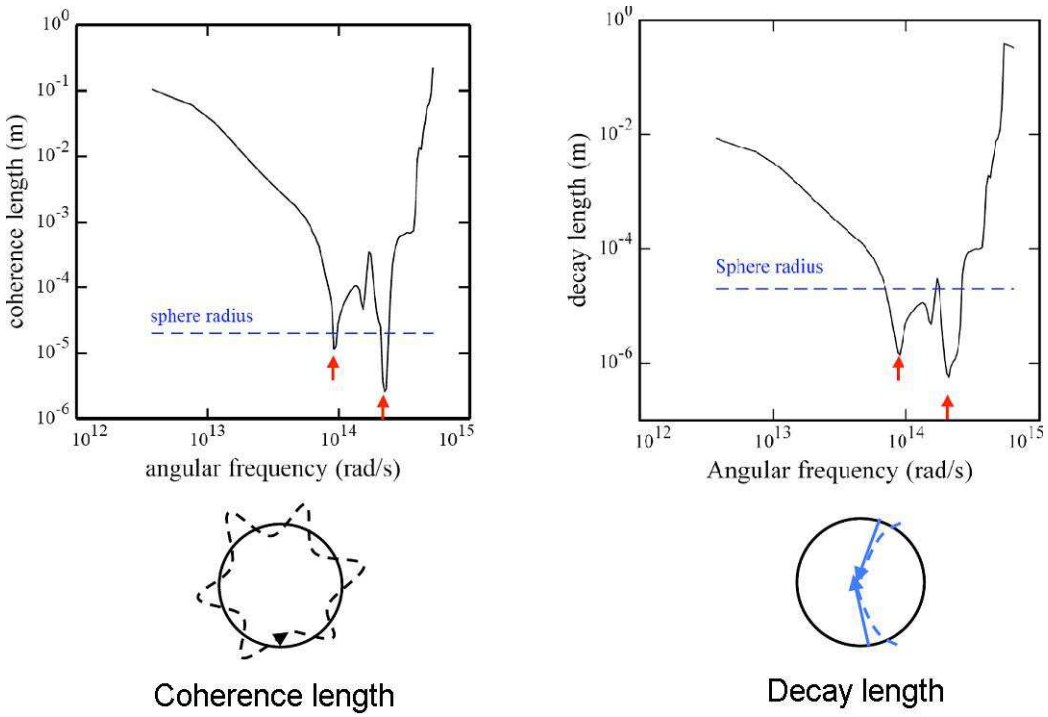

Figure 4.11: Coherence and decay length for a silica sample. The arrows are in correspondace of the surface resonance. The sphere radius is refered to the samples used during the measurements of radiative heat transfer

4.3 Experimental set-up

In figure 4.12a) it is shown a photo of the experimental set-up developed for the measurement of the near-field thermal radiation. A heated up plane sample is positioned over three piezo inertial axis motors, while the sphere sample (at T=300 K) is glued on a AFM cantilever. The plate is heated in order to produce a temperature difference ΔT between the sphere and the plate, typically on the order of 10-20 K. The temperature of the plate is measured with a type-K thermocouple.
The near-field radiative heat flux is on the order of nanoWatts so that conduction through air must be suppressed by working in a vacuum (10^{-6} $mbar$)
As fluxmeter we used the sphere glued on a bimorph cantilever based on an AFM cantilever as proposed by Barnes et al. [81, 82]. The experiments have been performed using spheres with 2 different diameters, 22 μm and 40 μm. Such fluxmeters can measure fluxes variations on the order of tens of pW. We use cantilevers commercially available from Veeco (length=320 μm, width=22 μm, thickness=0.6 μm) made of silicon nitride (thickness 525 nm) with a gold layer (60 nm) deposited on a chromium layer (15 nm).
The sphere is glued to the cantilever using a aluminium epoxy glue. This assures a good thermal contact between the sphere and the lever. The temperature of the sphere can be considered constant during the measurement; the power absorbed by the sphere is dissipated along the lever directly to the cantilever holder.
We can analyze the system in details. First of all we can assume that the system is in steady state. Indeed, the sphere becomes isothermal in a typical time 0.5 ms and the bimorph becomes isothermal in a typical time of 2 ms. All time constants in the experiment are greater than 100 ms.
We can now use an electrical analogy with thermal resistances. The thermal circuit is sketched fig. 4.13. It is composed of several resistances in series connecting the hot plate at T_p to the end of the bimorph at the ambient temperature at T_a.
The average thermal conductivity of the cantilever is $\lambda = 60\ W/(m \cdot K)$ leading to a thermal resistance $R_c = L/(\lambda \cdot w \cdot t) = 0.4 \times 10^6\ K/W$. The sphere thermal conductance is close to $R_s \approx 1/(\lambda \cdot R) = 0.04 \times 10^6\ K/W$ where R is the sphere radius.
We approximate the glue by a cylinder with length smaller than one micron and radius larger than one micron. Its thermal conductivity is $\lambda = 1.6\ W/(m \cdot K)$ leading to a thermal resistance smaller than $R_g = L/(\lambda \cdot t \cdot w) = 0.6 \times 10^6\ K/W$.
From fig. 4.10 for a distance of 100 nm the expected thermal conductance is $\approx 10\ nW/K$ leading to a thermal resistance of the gap $R_r \approx 100 \times 10^6 K/W$.

a)

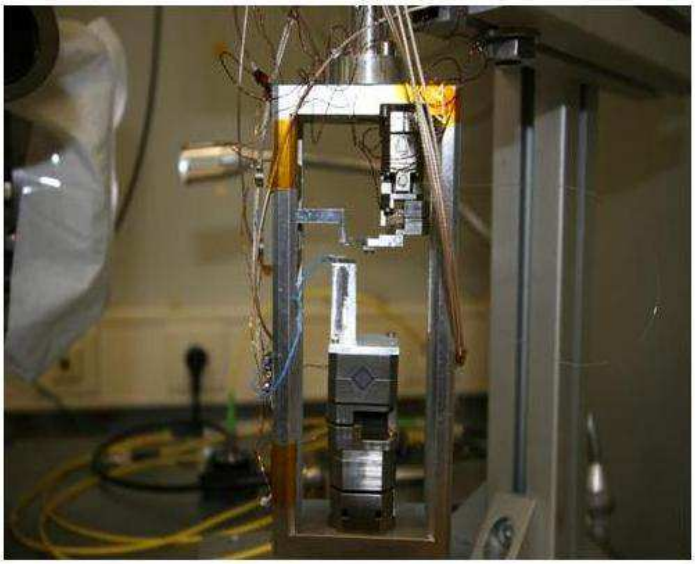

b)

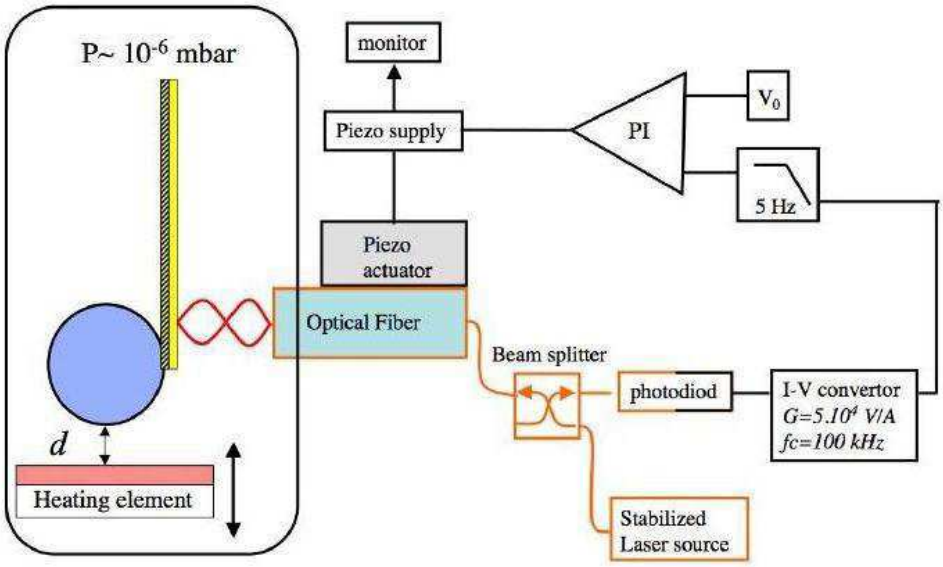

Figure 4.12: a) Photo of the experimental set-up. b) Schema of the experimental set-up. Red lines stand for light; black lines stand for electrical wires. A feedback loop keeps the distance bimorph-optical fiber constant by applying a voltage on a piezoelectric actuator holding the optical fiber. The setup is in a vacuum chamber working at $P \approx 10^{-6}\ mbar$.

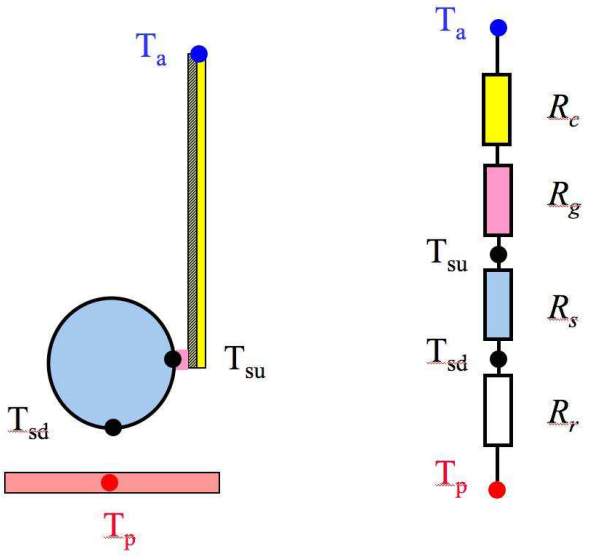

Figure 4.13: Equivalent circuit of the experiment. T_p is the hot plate temperature. The end of the bimorph is at the ambient temperature T_a. T_{sd} denote the temperature of the sphere surface. R_r denotes the radiative thermal resistance of the gap, R_s the sphere thermal resistance, R_g the thermal resistance of the glue and R_c the cantilever thermal resistance.

Despite the near-field contribution increases the conductance, the gap resistance remains the largest thermal resistance in the system. It is at least two orders of magnitude larger than other thermal resistances in the circuit. It follows that the temperature of the sphere is equal to the ambient temperature within the accuracy of the thermocouples

$$T_{sd} - T_p = \frac{R_r}{R_r + R_s + R_g + R_c}(T_a - T_p). \tag{4.23}$$

The heat absorption induces a bending of the cantilever. The cantilever bending is measured by a fiber interferometric technique as shown in fig 4.12 a) and schematically explained in chapter 2. A drawback of using an optical read-out is that part of the optical beam is absorbed and introduces a spurious flux term. It is thus fundamental to keep it constant during the measurement. A feedback loop keeps the distance between the cantilever and the optical fiber constant. In addition, a thermally stabilized laser is used in order to reduce the absorption fluctuations by the fluxmeter.
The cantilever is perpendicular to the plane (see fig. 4.12) to avoid bending due to electrostatic or Casimir forces. The displacements done with piezoelectric stages from Attocube have been calibrated using an interferometric

method as explained in [10].
All the measurements have been performed in a static mode. The Peltier heating element is actuated with a DC current, assuring a constant temperature all over the plate.
A static measurement is affected by a noise induced by the thermal drift of the differents elements. The drift of the lever respect with the fiber can be easily measured studying the evolution of the feedback voltage applied to the piezolectric stage in order to keep the distance fiber-lever constant, with the heating element put in the far-field regime and at a constant distance. Before each measurement the drift of the lever has been measured (average drift measured is $\approx$ 1.5 nm/min).
The hot plate is approached to the sphere using a PC controlled piezoelement. The approaching speed has been tuned from 15 nm/s to 60 nm/s; there is no difference between experiments made at different speeds once the thermal drift is accounted for.

4.4 Radiative heat transfer measurements

4.4.1 Fluxmeter calibration

During all the experiments the raw data consist in the bending δ of the cantilever versus the sphere-plate distance as presented in figure 4.14. The cantilever bending is detected using the feedback voltage applied to the optical fiber actuator in the constant-distance mode.
However for a consistent comparison of the experimental results with theory we need to convert such bending value in a heat flux value. In order to calibrate the cantilever response, we use the same experimental setup working in the far-field regime. The gap between the plate and the sphere is approximatively 50 μm. We measure the cantilever bending when increasing the temperature of the hot plate.
The far-field flux is determined from: $\phi = 8\pi\sigma\varepsilon R^2 T^3 \Delta T$ where σ is the Stefan-Boltzmann constant, R the sphere radius, T=300 K the mean temperature, $\varepsilon = 0.354$ the mean emissivity taken from the exact calculation between two infinite planes. ΔT is the temperature difference between the sphere and the plate. From 4.15 we have that the conversion between the bending of the lever and the absorbed flux is given by a simple linear relation; such result is indeed consistent with Barnes et al. [81, 82].
The conversion factor H can be extracted from the slope of the curve 4.15. It is found to be $H = 2.30\ nW/nm$. The total uncertainty on H is estimated to be 10% due to uncertainties on the temperature T and the total emissivity.

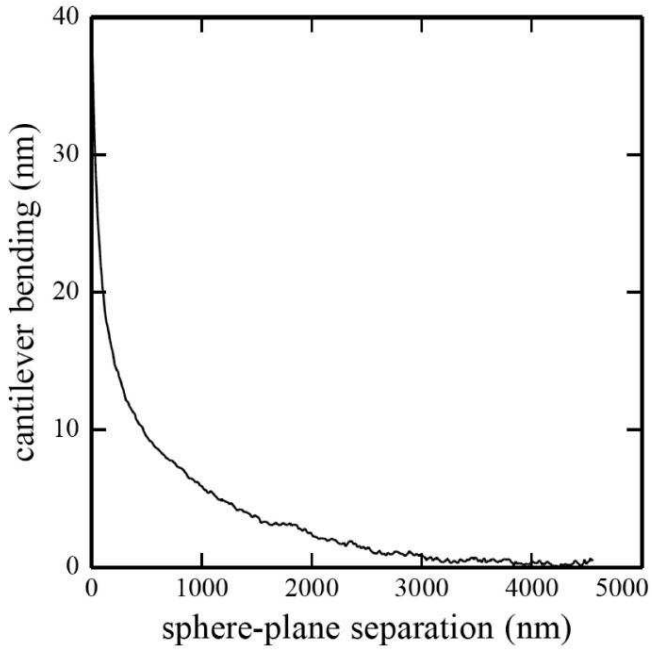

Figure 4.14: Cantilever bending versus distance sphere-plane. The zero in the z-axis has been determined for this plot by the direct contact of the sphere with the plate.

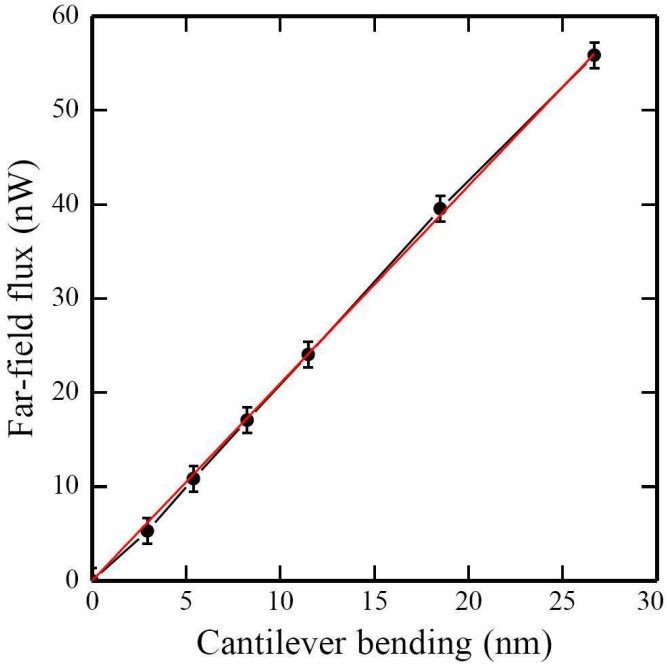

Figure 4.15: Cantilever bending versus the thermal flux when the sphere is exclusively in the far-field regime. The distance between the sphere and the plate is around 50 μm. The conversion factor H is extracted from the slope of the fit.

4.4.2 Surface roughness analysis

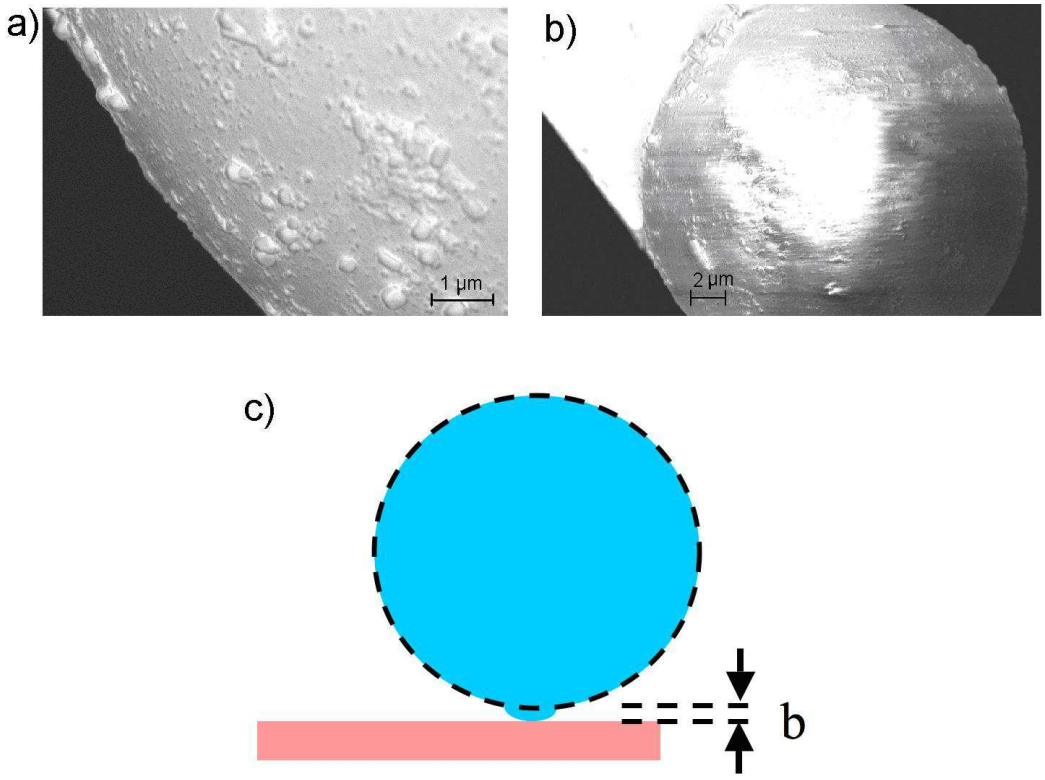

Figure 4.16: a) SEM picture of the 40 μm sphere. b) SEM picture of the 22 μm sphere. c) Definition of the fitting parameter b.

Before entering the comparison between the experimental data and the theoretical model, we analyze the origin of the distance axis in figure 4.14. The definition of the zero of distance is a crucial point when a force measurement is performed. A reliable comparison between theory and experiments can be done only if the experimental origin is consistent with the theoretical one.
If the theoretical model does not take into account the surface roughness of the samples, then the zero of the distance between the average surfaces of the samples has to be calibrated. The way of obtaining this fundamental information depends on the experimental conditions in analysis.
In the case of Casimir force measurement between metallic materials, the calibration of the zero can be obtained using the well known electrostatic

force between the two objects. Measuring the electrostatic force simultaneously with the Casimir force allows a consistent and reproducible calibration of the distance between the average surfaces [10].
For the measurement of Casimir force in viscous environment, the distance calibration can be performed using the hydrodynamic forces as reference [29, 30].
In both cases the calibration of the zero between the average surfaces is obtained using the dependency on the distance of a well known force. The evolution of the calibration force with the distance allows to obtain the zero without any direct contact between the samples.
In the case in the analysis however we cannot use such calibration method. In fact we are working with dielectric material in vacuum condition. The zero of the z-axis has to be determined by the direct contact of the sphere with plane. Then the sample surface roughness is an important parameter to take into account.
Because of the sphere roughness, in this experiment the zero obtained by the contact is actually shifted respect with the zero of the average surface that is important for the thermal transfer. For a correct comparison between theory and experiment we have consequently introduced a shift b in the definition of the theoretical thermal conductance:

$$G_{theo}(d,T) = \int_0^R h[d(r) + \mathbf{b}, T] 2\pi r \; dr. \tag{4.24}$$

4.5 Radiative heat transfer: comparison between experimental results and theoretical model

Starting form the raw data it is now possible to convert the bare bending δ of the cantilever in a value of the thermal conductance:

$$G_{exp}(d) = \frac{H}{\Delta T}\delta + G_{ff}. \tag{4.25}$$

In equation 4.25 we have added the value of the far-field conductance $G_{ff} = 8\pi\sigma\varepsilon R^2 T^3 = 5.45 \; nW/K$. In fact even if the raw data tend to zero of the deflection for distance larger then 5 μm it is worth to note that the measurement of the deflection is actually a relative measurement respect with the far-field regime.
The comparison between the theory and the experiments finally becomes a comparison between equations 4.24 and 4.25. In this comparison we have

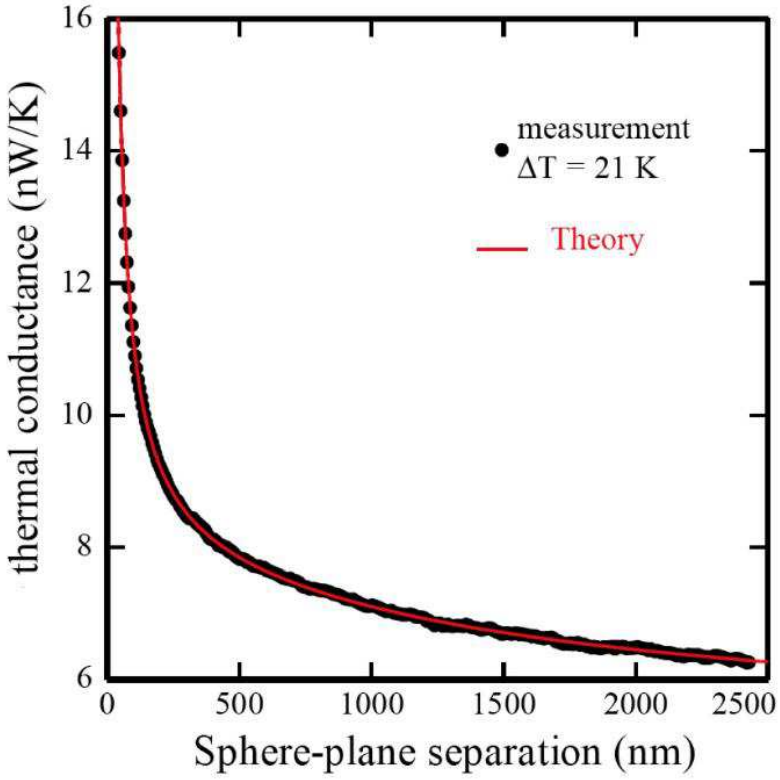

Figure 4.17: Thermal conductance between the sphere and the plate as a function of the gap distance. Black dots are experimental data and red line is the theoretical model. The temperature difference between the plate and the sphere is 21 K.

two parameters given by experimental constraints: shift value b and the conversion factor H.
The b parameter essentially shifts the zero position of the abscisses. H is a scaling factor on the ordinates. Although as seen these two parameters have been experimentally studied, we prefer to use them here as fitting parameters so that the PFA approximation is clearly addressed. Fitted values are finally very close to the measured values. This is consistent within this procedure.
Fig.4.17 shows a comparison of the data with the model for a particular approach curve. We found $H = 2.162 nW/nm$. This value is consistent with the calibration value H=2.30 nW/nm obtained with the calibration. The shift b is of the order of 50 nm which is consistent with the SEM images of the sphere surface roughness.
In Fig.4.18 a) it is shown the flux variation when decreasing the distance between the sphere and the plate for three different temperatures. We plot

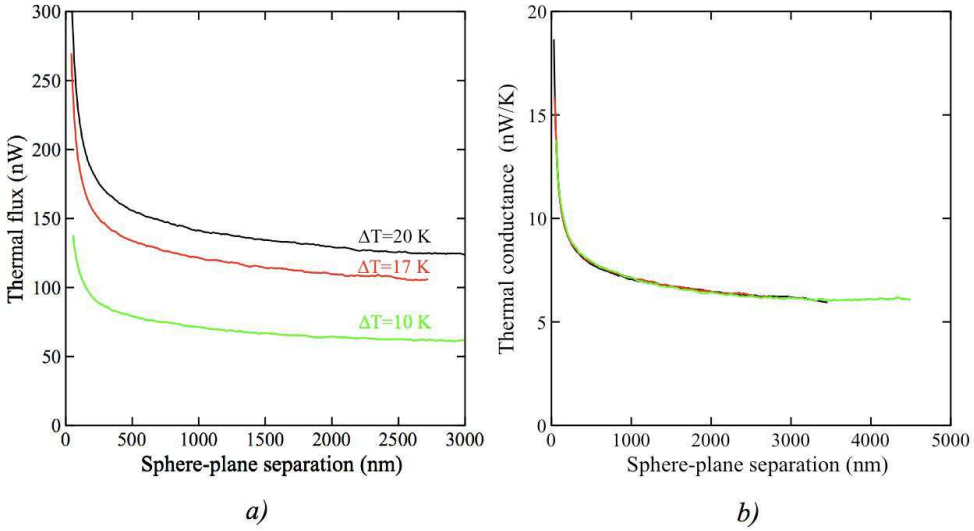

Figure 4.18: a) Flux versus distance for three temperature differences. The sphere diameter is 40 μm. b) Thermal conductance derived from three different sets of measurements. The same value of H was used for the three curves.

in Fig.4.18 b) the thermal conductance for the three temperature differences after determining the shift b. The response coefficient H used for the three curves has the same value as the same cantilever is used. It is seen that the three measurements yield the same conductance. This shows that for different temperature shifts (DT up to nearly 10 %), i.e. for different out of equilibrium situations, the curve shape is the same within the experimental error.

The key result in Fig. 4.17 is the agreement better than 4 % between the data and the theory. We emphasize that the theory reproduces correctly the non-trivial transition between the far-field and the near-field regime in the range 30 nm - 5 μm. The agreement between the theoretical conductance and the data shows that the theory based on the coupling of the electromagnetic treatment of the radiative heat transfer with the Derjaguin approximation is valid.

As a further check of the theory, we make measurements with a sphere with a different radius. Fig. 4.19 presents the data in logarithmic scales for two spheres with radii 20 μm and 11 μm. The curves are different indicating a non-trivial dependence of the conductance on the sphere radius. The red line is the result of the numerical integral using Derjaguin approximation. The dashed blue curve is the $1/d$ asymptotic dependence for the sphere-plane

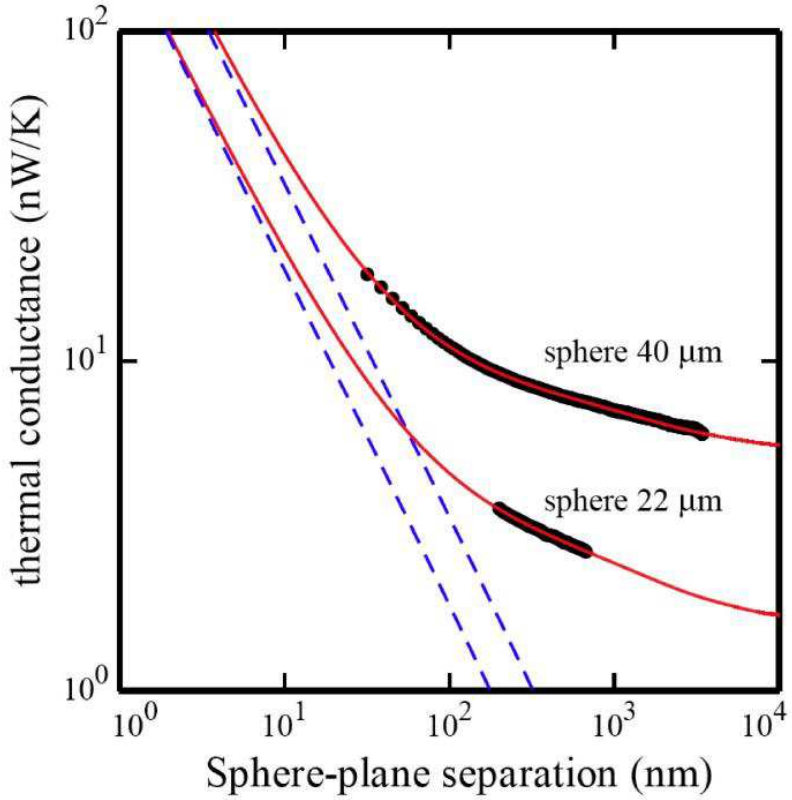

Figure 4.19: Thermal conductance between the sphere and the plate as a function of the gap for two sphere diameters (40 and 22 μm). Black dots are experimental data and red line is the theoretical model. The dashed blue line is the asymptotic contribution varying as $1/d$. This contribution is dominant for gaps smaller than 10 nm. For the 22 μm sphere the smallest separation is 150 nm due to roughness.

geometry.
We found that the data agree with the theory with a 4% accuracy in the range 50 nm - 5 μm. This agreement with theory confirms that radiative heat transfer can be significantly enhanced at distances in the nanometer regime.
The results obtained strongly support previous theoretical works and pave the way to engineering radiative heat transfer in the mesoscopic regime. Moreover we have shown that also for the radiative heat transfer the Derjaguin approximation for sphere-plane geometry leads to results consistent with the experimental evidence.
The results obtained should play a major role in the further development of

Nano Electro Mechanical Systems (NEMS). In addition other technological application can be surely envisaged as heat-assisted magnetic recording or heat- assisted lithography applications.
From a fundamental point of view, other important aspects of the radiative heat transfer at nanoscale remain to be explored: just to mention, it has been predicted that the flux can be quasi monochromatic [77, 79] and strongly depends on the matching between optical properties of both materials. The understanding of the role of non-local effects at distances smaller than 10 nm is also a subject in progress in the literature [73, 83, 84] so that further experiments are needed in this regime.

Chapter 5

Conclusions and Perspectives

Micro and Nano Electro Mechanical Systems (MEMS and NEMS) are among the best tools for the characterization and manipulation of the nanoworld. NEMS and MEMS are also among the best candidates for the characterizations of interaction forces at the nanoscale.
In this thesis we have addressed different aspects of the physics at the nanoscale using a very simple example of MEMS: a tiny silicon micro cantilever.
We can now make a summary of the most important results obtained along this work.
In chapter 2 we have analyzed the dynamics of a micro lever in a simple fluid, air in our case. In particular we have analyzed what has happened to the cantilever dynamics if the lever is vibrating closed to a solid surface. The behavior of the fluid and consequently that of the lever is modified by the presence of the surface due to the fluid confinement. The complete understanding of lever dynamics in a confined fluid is known to be a fundamental issue. Oscillating cantilevers in viscous environments are used in many applications, for example to measure the topography or the properties of biological specimens.
We have considered the problem of oscillation damping in air of a thermally actuated microlever as it gradually approaches an infinite wall in parallel geometry. As the gap d is decreased from 20 μm down to 400 nm, we observe a decreasing of the oscillation amplitude, therefore an increasing damping of the lever Brownian motion.
Experimentally we observe a linear relation between the cantilever damping factor and the cavity gap:

$$\gamma = \frac{2\eta A}{d} \tag{5.1}$$

where η is the fluid viscosity and A the cantilever surface.
We have been able to theoretically explain such behavior by solving the Navier-Stokes equation for the given geometry. The no slip boundary conditions for the fluid at the solid fluid interface, that are generally accepted for macroscopic hydrodynamics problem, do not allow to reproduce the experimental evidence. A good agreement theory-experiments can be obtained accepting the perfect slip boundary conditions for the fluid.
We have seen that, moreover, it is possible to determine a critical gap, so that for cavity size lower than this value the mechanical oscillator is in an over-damped regime. The gap value have been evaluated to be in the submicron and nanometer region. Consequently it can modify the behavior of MEMS and NEMS. These results can have important implications in the field of NEMS.
Micro and Nano mechanical oscillator have been proposed to measure the mechanical effect of light. In chapter 3 we have applied this idea to the synchrotron radiation.
We have seen that a micro oscillator, composed by silicon cantilever with a germanium microblock attached at its extremity, can be actuated by an intensity modulated X-ray beam. Coupling the optical properties of the germanium block with the mechanical properties of the cantilever we have seen how the MEMS oscillation can be tuned. When the impinging X-ray beam energy is swept trough the germanium absorption edge, we observe an increase of the oscillation amplitude consistent with the evolution of the X-ray beam absorption coefficient. This has led to a mechanical detection of the germanium EXAFS, using as *detector* the oscillation amplitude of the cantilever.
In the same chapter we have also seen how the coupling between MEMS and X-ray can be inverted. A MEMS can be used to shape an X-ray beam. Using oscillating single crystal silicon cantilever we have realized a fast X-ray chopper. The incoming X-ray beam was set to the Bragg condition for the diffraction on the silicon cantilever. The driven oscillation of cantilever modified the X-ray incidence angle changing the actual Bragg condition. The diffracted beam intensity was consequently modulated at the frequency of the cantilever oscillations.
Finally in chapter 4 we have addressed the problem of radiative heat transfer at the nanoscale. The thermal conductance is observed to increase at the nanoscale, when electromagnetic coupling occurs due to the overlapping of the evanescent waves.
The full control of the heat transfer is then crucial for a reliable development of nano systems.
From a scientific point of view the analysis of transfer at nano scale has its

own interest. It has been predicted that at the nanometer scale the thermal radiation exceed the Plank's description because of the near-field contribution of the thermal radiation. Although the presence of this anomalous thermal effect has been shown, a comparison theory-experiments was still lacking.
In chapter 4 we have presented measurement of radiative heat transfer at the nanoscale between a hot plane and a cold sphere glued to a silicon microcantilever. The agreement between the experimental results and a theoretical model was better than 4 % in the range 50 nm - 5 μm. The theoretical model has been obtained coupling the electromagnetic treatment of the thermal radiation with the Derjaguin approximation for the sphere-plane geometry.
This thesis has been dedicated to the measurement of forces and interactions at the nanoscale. MEMS have been implemented in the work as probe for the different measurements.
Interaction forces between objects at the nanoscale have been measured since the development of Atomic Force Microscopy for many years. Van der Waals forces, hydrodynamic forces and Casimir forces have been studied using micro cantilevers.
So far a good precision in the force measurements have been achieved in the sphere-plane geometry. Standard experimental set-up involves a sphere glued to a oscillating silicon cantilever approaching to a plane sample. Identical experimental set-up has been used in chapter 4 of this thesis. Using this configuration avoids parallelism difficulties of the plane-plane geometry. From an experimental point of view this configuration simplify the task: the measurement can be performed. However a major issue arises for the theory. The sphere-plane expression can be obtained only within the Derjaguin approximation. The limit of the validity of this approximation is nowadays questioned, for example in the debate of the precise measurement of the Casimir force and thermal radiative heat transfer.
The possibility to achieve a good parallelism would allow to make a comparison between theory and experience without any approximation. In chapter 2 we have seen that a comparison theory-experiments in the demanding parallel plates geometry can be done, within the 5 % of agreement, for the hydrodynamic forces induced by a fluid confinment. In that case any particular treatment of the misalignment has been accomplished. The residual misalignment of 10 $mrad$ has not affected the validity of the measurements. This has made possible thanks to the weak dependency of the hydrodynamic forces with the distance. In the case which has been analyzed it has a dependency as $1/d$.
We now consider how the other interactions vary with the distance in the demanding plane-plane geometry.

- Hydrodynamic force (perfect slip boundary conditions):

$$F = -\gamma \cdot v = -\frac{2\eta A v}{d} \Rightarrow \ F \to 1/d; \tag{5.2}$$

(see page 30)

- Electrostatic force between two conductors:

$$F = -\frac{1}{2}\frac{\varepsilon V^2 A}{d^2} \Rightarrow \ F \to 1/d^2; \tag{5.3}$$

- Radiative heat transfer between dielectric materials:

$$\phi \to 1/d^2; \tag{5.4}$$

(see page 74)

- Hydrodynamic force (no slip boundary conditions):

$$F = -\gamma \cdot v = -\frac{\eta w L^3}{d^3} \Rightarrow \ F \to 1/d^3; \tag{5.5}$$

(see page 28)

- Casimir force between two perfect mirrors ($\varepsilon = -\infty$):

$$F = \frac{\hbar c \pi^2 A}{240 d^4} \Rightarrow \ F \to 1/d^4. \tag{5.6}$$

Considering the distance dependency it is clear that, with the exception of the hydrodynamic force with perfect slip boundary conditions, the problem of the misalignment has to be taken into account.
This aspect has been the subject of the very last part of this thesis. An experimental set-up for the measurement of radiative heat transfer between flat surfaces has been realized.
A simulation has been performed before starting the measurement to understand the effect of a small misalignment between the planes on the radiative transfer. From fig. 5.1 it is evident that a control of the angle much better than 0.1 degree, *i.e* 1.7 *mrad*, is needed.
For the measurement of radiative transfer between a sphere and a plane, the sphere has been manually glued to a cantilever. In the case of plane-plane measurement the realization of the sample deserves particular attentions.
For this reason, remembering what done in chapter 3, a Focus Ion Beam has been used for the sample realization. A cubic like block has been extracted

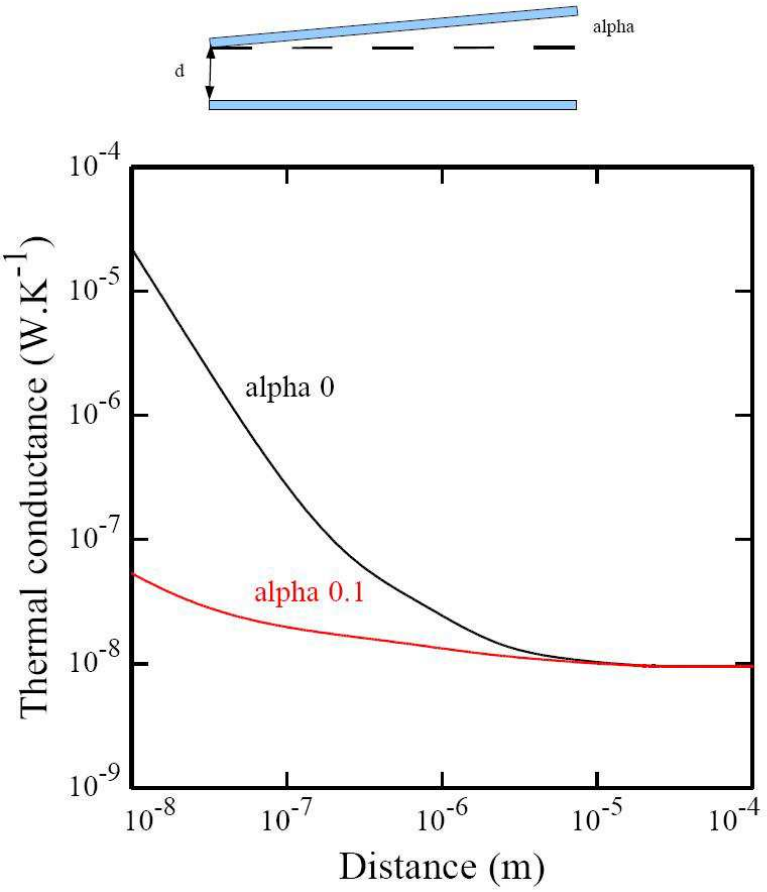

Figure 5.1: Misalignment effect on radiative heat transfer

by a flat wafer of silicon. This block has been welded to the cantilever using the FIB. The surface of the block has been polished so that the roughness was below 10 nm rms.

The two flat samples were not assembled together. They are put on different stages which have been approached towards each other. For this reason a 2 angle tilter systems have been added to the experimental set-up presented in chapter 4, allowing angular precision better than 0.1 millidegree.

The precision achieved in the angle control was in principle enough to assure a reliable comparison theory-experiments. To find minimal angular misaignement, curves of flux as function of distance have been measured varying the sample tilt (see figure 5.4).

The procedure is an iterative process; after having roughly adjusted one angle, the same thing had to be done with the other. This would allow us to find the minimum of the angles with a coarse sweep. Increasing the precision

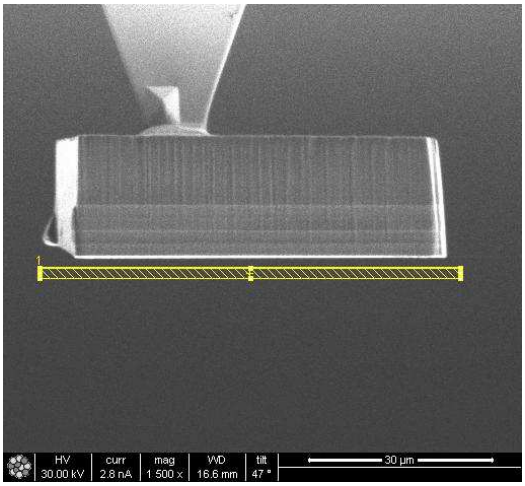

Figure 5.2: Sample realized for the measurement of radiative heat transfer between two plates. The FIB realization has been performed at the CEA/LETI-MINATEC

of the sweep would allow us to increase the precision in the zero definition. Unfortunately, the parallelism between the two surfaces has not been achieved in this first series of measurement.
In chapter 3 we have seen that diffraction of an X-ray beam is very sensitive to the incidence angle of the beam on the surface sample. We now propose the use of X-ray diffraction for the alignment of two flat surfaces.
As shown in figure 5.5 a X-ray beam can imping to the first surface at the Bragg condition angle. The diffracted beam will have the same properties of the incoming beam. Then it will imping on the second flat surface. The X-ray beam will be diffracted again only if the two surfaces are parallel. The precision of the parallelism is given by the width of the Bragg peak. As discussed in chapter 3 the width of the Bragg peak in the case of Silicon (1 0 0) for a crystal thckness $t > 20\ \mu m$ is $\approx 10^{-4}$ deg.
This technique can be implemented in a force measurement experimental set-up. Using a laboratory X-ray tube, a X-ray beam can imping on the sample that is fixed. A photodiode can be positioned on the other side of the experimental set-up. The second surface can be mounted over a tilter systems as previously presented. Only when the parallelism between the two surfaces is achieved, the photodiode will detect an outcoming X-ray beam.
The precision that can be obtained coupling the FIB realization of the sample with the angle control by means of inertial steppers should be enough to perform measurement in plane-plane geometry also for the Casimir force.
The experimental set-up here presented differs to today existing set-up for

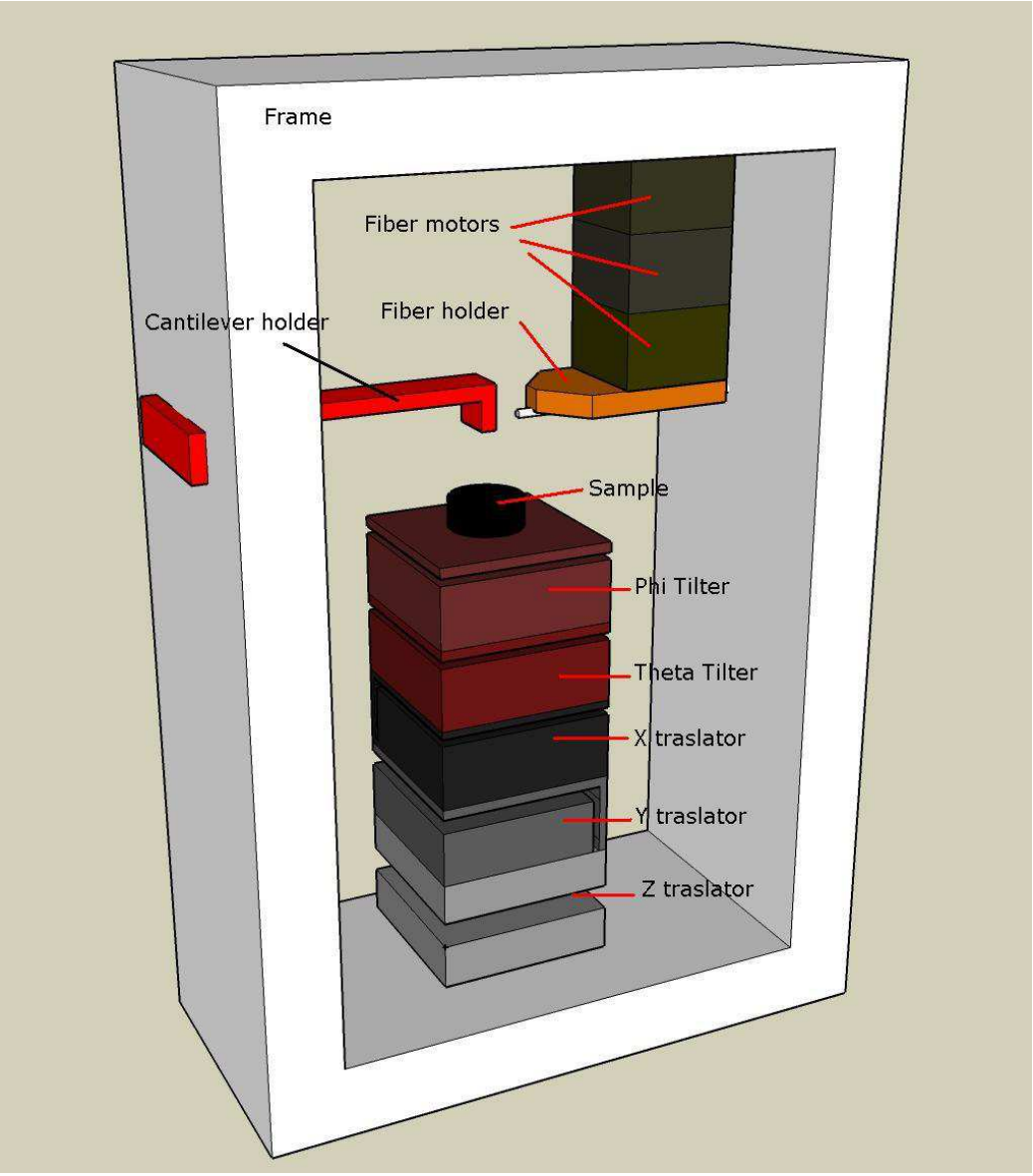

Figure 5.3: Schema of the experimental set-up realized for the measurement of radiative heat transfer between two plates

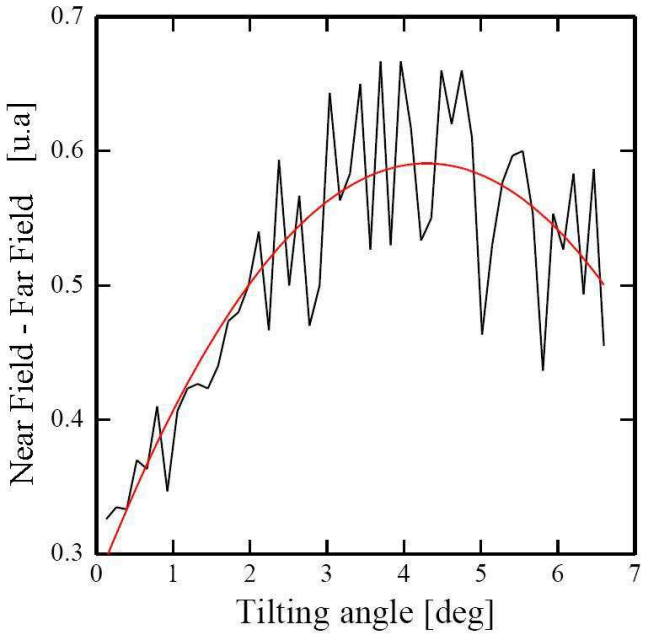

Figure 5.4: Evolution of the flux variation between the far field regime and the near field (here measured before the contact between the 2 planes) as a function of tilting angle

measurements in plane-plane geometry. The group of Valéry Nesvizhevsky at the Institut Laue Langevin (ILL) in Grenoble developed an experimental set-up for the measurement of the quantum states of neutrons in the Earth's gravitational field [85]. The set-up main elements are a mirror and a neutron absorber whose sized was around 10 cm. The two flat surface had to be parallel and perpendicular to the Earth's gravitational field. This has been obtained using a high precision torsion balance. The precision achieved in the parallism was $\approx 10^{-6}$ rad (10^{-4} deg). However in the case of Valéry Nesvizhevsky any force detection system was related to the flat surfaces as it should be in the case of interaction forces measurements.
Bressi and coworkers implemented a capacitive measurement in a force machine [86]. The precision in the parallelism was $\approx 3 \times 10^{-5}$ rad ($\approx 2 \times 10^{-3}$ deg). They measured the Casimir effect between two metallic planes with agreement between theory and experience $\approx 15\%$. This experimental set-up, even if allowed a precise measurement of the Casimir effect, it was very complicated and did not allowed the measurement of the effect with different samples or materials.
The set-up presented here should allow the measurement of interactions in

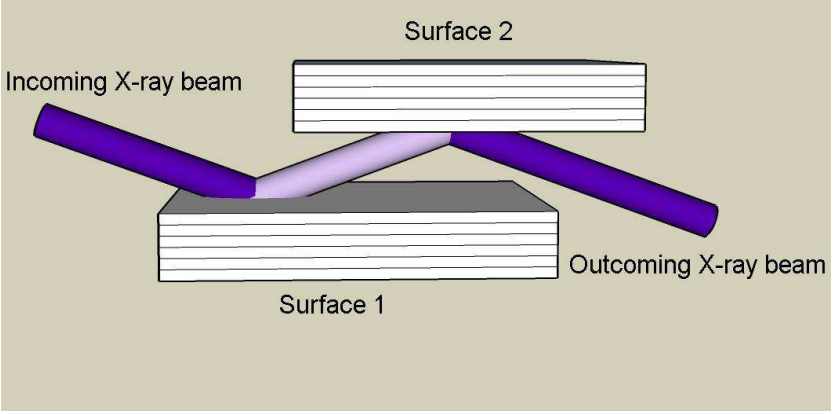

Figure 5.5: Alignement of two plane surfaces using X-ray diffraction

plane-plane geometry with the possibility to change the sample very easily. The precision in the parallelism that could be achieved should allow a very precise measurement of the plane-plane interaction forces (for the Casimir force an agreement theory-experiments much better than 15 % should be achieved). This will open new possibilities to study the effect of material and surface nanostructurization on interactions forces acting at the nanoscale.

Appendix A

Viscous cavity damping of a cantilever in a simple fluid

Viscous Cavity Damping of a Microlever in a Simple Fluid

A. Siria,[1,2] A. Drezet,[1] F. Marchi,[1,3] F. Comin,[3] S. Huant,[1] and J. Chevrier[1]

[1]*Institut Néel, CNRS and Université Joseph Fourier Grenoble, BP 166, 38042 Grenoble Cedex 9, France*

[2]*CEA/LETI-MINATEC, 17 Avenue des Martyrs, 38054 Grenoble Cedex 9, France*

[3]*ESRF, 6 rue Jules Horowitz, 38043 Grenoble Cedex 9, France*

(Received 6 February 2009; published 24 June 2009)

We consider the problem of oscillation damping in air of a thermally actuated microlever as it gradually approaches an infinite wall in parallel geometry. As the gap is decreased from 20 μm down to 400 nm, we observe the increasing damping of the lever Brownian motion in the fluid laminar regime. This manifests itself as a linear decrease in the lever quality factor accompanied by a dramatic softening of its resonance, and eventually leads to the freezing of the CL oscillation. We are able to quantitatively explain this behavior by analytically solving the Navier-Stokes equation with perfect slip boundary conditions. Our findings may have implications for microfluidics and micro- and nanoelectromechanical applications.

DOI: 10.1103/PhysRevLett.102.254503 PACS numbers: 47.61.Fg, 07.79.Lh, 47.15.Rq, 85.85.+j

Micro- and nanoscale mechanical levers are increasingly used as sensors and actuators in a large variety of fundamental studies and applications. Mass detection at the zeptogram scale [1], subattonewton force detection [2], and optical cooling of microlevers [3] are among the most spectacular achievements of oscillating cantilevers (CLs). These realizations mainly rely upon the extraordinary high quality factors (Q) of oscillating CLs in vacuum and/or cryogenic temperatures where values exceeding 100 000 are attainable. Clearly, maintaining such performances in air or in a liquid is a very challenging issue as oscillation damping in the surrounding fluid dramatically degrades Q. This has been partially circumvented by using ultrasmall self-sensing nanoelectromechanical systems (NEMS, i.e., actuated mechanical devices made from submicron mechanical components facing each other) operating in ambient conditions of temperature and pressure [4].

However, oscillating CLs are also used in viscous environments on many occasions [5–8]. In atomic force microscopy (AFM), for example, a resonant CL is used to measure surface topography and physicochemical properties of various materials not only in air but also in liquids [9] for, e.g., visualizing dynamic biomolecular processes at video rate [10]. The interaction between an AFM CL and a surrounding liquid has been used for a distance calibration in a Casimir force measurement [11] and has led very recently to the spectacular demonstration of a repulsive Casimir force [12]. Therefore, the need for a quantitative study of the CL behavior in viscous micro- and nanoscale environments is increasing. In this Letter, we report such a quantitative study and show, down to the submicron scale and in the demanding plane-plane geometry, how confinement and boundary conditions at the solid-fluid interfaces conspire to change the coupling to thermal bath and how this can freeze out the lever oscillation.

When a CL beam vibrates in a viscous fluid, the fluid offers resistance to the beam displacement [13,14]. If the CL is vibrating close to a solid surface, the behavior of the fluid and, consequently, that of the lever are modified by the surface due to confinement. The Navier-Stokes (NS) equations give a complete description of the fluid behavior, taking into account the particular environment under analysis. However, an analytical solution of NS equations is possible only for a restricted number of geometries, and comparison of theory with experimentally relevant configurations is in general a complex matter or is even lacking, especially at the deep micron and submicron scales [15–20] where boundary conditions at the fluid-solid interfaces are strongly modified [21–24]. In this Letter, we focus on the dynamical behavior of a microlever close to a planar rigid surface in the air. Provided that adapted boundary conditions are used, the NS equations can be solved analytically for this plane-plane model geometry that mimics a basic part of a MEMS (the counterpart of a NEMS in the micron range) device operating in the air.

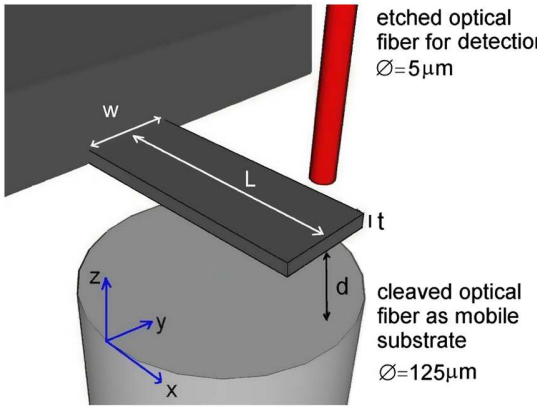

FIG. 1 (color online). Scheme of the experimental setup (not to scale). The analyzed mechanical system is a standard AFM CL. A cleaved optical fiber (bottom) is used as mobile substrate forming a cavity with the CL. An etched optical fiber (top) is used for the interferometric detection of the CL Brownian motion. The main geometrical parameters used in the text are identified; the z origin is taken on the flat cleaved-fiber surface.

This, combined with the use of the fluctuation-dissipation theorem and of an experimental arrangement specially designed to gain access to the intrinsic behavior of the CL, enables us to make a quantitative comparison between theory and experiment in a wide range of cavity lengths down to a few hundred nanometers.

Our setup is shown schematically in Fig. 1. Its first specification is that the CL—a commercial thin silicon AFM CL [25] for liquid imaging with dimensions $L \times w \times t = 107 \times 30 \times 0.18\ \mu\text{m}^3$—is actuated by the stochastic thermal noise only. This induces sub-Angstrom oscillations at the CL resonance frequency [$\omega_0/(2\pi) \simeq 49.5$ kHz], thereby allowing us to consider the fluid in the cavity in the laminar regime. Second, the planar rigid surface facing the CL to form a parallel-plate cavity is made of a cleaved optical fiber with a diameter of 125 μm that is mounted over a three-axis inertial motor so as to be able to adjust the cavity gap. This positioning system offers a large displacement range (8 mm each axis full range) with a good accuracy (40 nm per step). Finally, the CL Brownian motion is measured by means of a noninvasive interferometric detection based on the use of a very thin optical fiber facing the CL at a 2 μm distance. This fiber has been chemically etched so as to reduce its diameter to 5 μm. This corresponds basically to the fiber core diameter plus a residual amount of the optical cladding for better light guidance. The large ratio in excess of 600 between the areas of the cleaved and detection fibers ensures that only the cleaved one induces air confinement, not the etched one, which is used for detection purpose only. Therefore, no additional uncontrolled confinement and damping are produced by the detection fiber.

An AFM CL vibrating in a viscous fluid may be viewed as a driven and damped 1D harmonic oscillator whose equation of motion reads

$$m\ddot{z}(t) + \gamma\dot{z}(t) + kz(t) = F_{\text{ext}}, \tag{1}$$

where m, $z(t)$, k are the CL effective mass, time-dependent position, and stiffness, respectively, γ is the damping factor, and F_{ext} the external (i.e., thermal) driving force. According to the fluctuation-dissipation theorem, the thermal Brownian motion of the CL at temperature T is accounted for by a frequency independent force power spectrum defined as $S_F(\omega) = 2k_BT\gamma$ [k_B is the Boltzmann constant, and ω the pulsation linked to the frequency $f = \omega/(2\pi)$]. Starting from Eq. (1) we obtain the CL displacement power spectrum as $S_z(\omega) = S_F(\omega)|\chi(\omega)|^2$, where the CL transfer function $\chi(\omega)$ is given by

$$\chi(\omega) = \frac{1}{m(\omega_0^2 - \omega^2) - i\gamma\omega} \tag{2}$$

with $\omega_0 = \sqrt{\frac{k}{m}}$. In the limit of small damping, i.e., $\frac{\gamma}{m} \ll \omega_0$, $S_z(\omega)$ has a resonance at ω_0. In Fig. 2, the experimental Brownian oscillation power spectrum $2S_z(\omega)$ is presented as a function of frequency f for different cavity gaps d. It is clearly seen that the resonance peak dramatically broadens and softens to lower frequencies with decreasing gap. Within the experimental accuracy, we find that the area under the resonance curves in Fig. 2 remains constant and equals to the thermal energy. This shows that the CL damping increases with decreasing gap.

Now, we turn to a quantitative analysis of the experiment. The fluid responsible for the CL damping is the air confined between the CL and the mobile fiber. The dynamic of such an incompressible fluid is described by the NS equations

$$\rho\left[\frac{\partial\vec{v}}{\partial t} + \vec{v}\cdot\nabla\vec{v}\right] = \eta\nabla^2\vec{v} - \vec{\nabla}p, \tag{3}$$

where $\vec{v}$ is the fluid velocity, ρ its density, η its dynamical viscosity, and p the gas pressure. In the laminar regime, i.e., in the limit of small Reynolds numbers, Eq. (3) simplifies to $\eta\nabla^2\vec{v} \simeq \vec{\nabla}p$. In order to solve the NS equations, one needs to know the specific boundary conditions existing at the fluid-solid interfaces (for simplicity we assume the cavity plates to be infinitely extended). While for macroscopic hydrodynamic applications one usually accepts that fluids do not slip against solid walls, this is generally not true for microfluidic problems involving MEMS or NEMS [21]. A critical parameter in this respect is the Knudsen number [21] $K_n = \bar{\lambda}/d$ which depends on the gas mean free path $\bar{\lambda}$. For air at ambient conditions $\bar{\lambda} \simeq 60$ nm, which leads here to $K_n \sim 0.001$–0.06. In this range of K_n values, it is already known that fluid slip can occur over a solid interface [21–23]. In particular, partial fluid slip has been recently observed in the plane-sphere geometry in air using an AFM in dynamic mode [24]. However, none of the previous works investigated the regime of Brownian oscillations with typical CL amplitudes $\delta z \sim 0.05$ nm much smaller than $\bar{\lambda}$ (i.e., $\bar{\lambda}/\delta z \sim 10^3$). In such a regime, boundary conditions are expected to be even more strongly modified [21] compared with the macroscopic

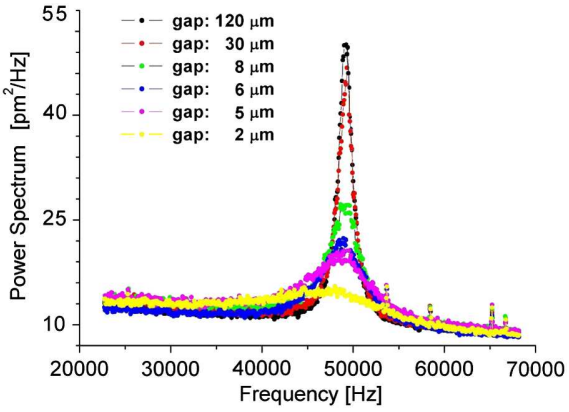

FIG. 2 (color online). The experimental Brownian oscillation power spectrum of the microlever for different cavity gaps.

regime, although it is not yet known how much they are modified. Here, we make the hypothesis of perfect slip, historically anticipated by Navier [26], for which friction along the solid interface is prohibited, and show that we can obtain a consistent quantitative description of our experimental data. This hypothesis results in a velocity gradient along the z direction which leads to a Stokes friction coefficient:

$$\gamma = \frac{2\eta A}{d}, \tag{4}$$

where $A = wL$ is the cantilever surface. The usual no-slip condition at the fluid-solid interface would predict $\gamma \simeq \eta w L^3/d^3$, in clear disagreement with the experiment (see below). As a direct consequence, Eq. (4) leads to a much smaller decay of the friction force with d than usually predicted.

Quantitative information on the damping factor is obtained from the analysis of the CL quality factor. Both quantities are linked together by the relation $Q = \frac{k}{\omega_0 \gamma}$, which becomes for small gaps

$$Q = \frac{k}{2\omega_0 \eta A} d. \tag{5}$$

Equation (5) predicts a linear dependence of Q on d that can be compared with experiments.

Figure 3 depicts the quality factor as function of the cavity gap. Two different regimes can be distinguished. For large gaps above 40 μm, the quality factor remains constant. This is the unconfined fluid regime where no additional damping can take place with decreasing gap. For smaller gaps, however, the quality factor tends to decrease with a decreasing gap. We will focus below on the small gap regime where the hypothesis of infinite planes is physically justified. Since the AFM CL has a surface 10 times smaller than the substrate fiber; the gap limit for the hypothesis of infinite planes to remain physically sound can be estimated by taking the apparent CL surface as a reference, i.e., $d_{\text{lim.}} \approx 15$ μm.

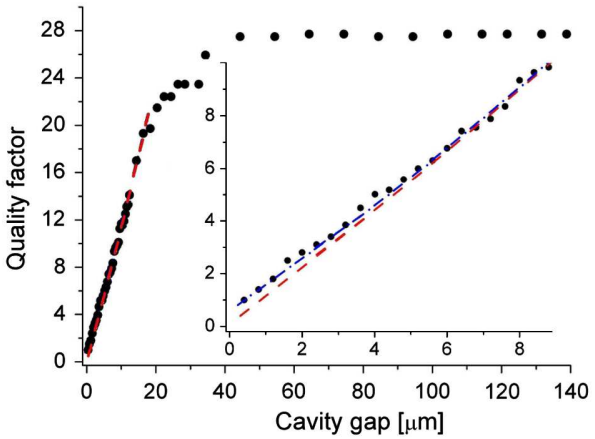

FIG. 3 (color online). The quality factor as a function of the cavity gap. The black dots are the experimental points. The insert depicts a zoom of the small gap range. In both cases, the red dashed curves exhibit the theoretical prediction based on Eq. (5), i.e., the prediction of the NS equation in the perfect parallel-plate geometry. The blue dash-dotted line in the insert shows the prediction of the NS model, taking into account a residual angular misalignment of the cavity as discussed in the text.

As shown in the inset of Fig. 3 the experimental results and the theoretical prediction of Eq. (5), with no adjustable parameter [27], coincide to within 5% for gaps larger than 5 μm, but for smaller separations, the disagreement worsens to reach 100% at the smallest gap, 400 nm. We interpret this difference with a residual small angular misalignment of the two facing parallel plates. For small misalignment, the problem can be treated within an approximation similar to the proximity force approximation used, for instance, in the Casimir force formulation in the sphere-plane geometry [28]. In this approximation, the corrected damping factor becomes

$$\gamma = \int_0^L \int_0^w 2\eta \frac{dx\,dy}{d_0 + x\tan\alpha + y\tan\beta}, \tag{6}$$

where d_0 is the shortest distance from the inclined CL to the substrate, and α and β are the lateral tilt angles of the CL with the mobile surface in the x and y directions, respectively. The best fit between experiment and theory is obtained for $\alpha \approx \beta \approx 10$ mrad. Considering these misalignment angles, the good agreement between theory and experiment can now be extended down to the smallest gap range that we have measured, as can be seen in Fig. 3. Over the entire range 400 nm–15 μm, the remaining disagreement is $\approx$5% only [29].

We now discuss the frequency softening of the CL oscillation, the other salient experimental fact revealed by Fig. 2. In the limit of large damping, i.e., the approximation $\frac{\gamma}{m} \ll \omega_0$ no longer holds, the power spectrum of Eq. (2) has a downshifted resonance pulsation ω' given by

$$\omega' = \sqrt{\omega_0^2 - \frac{1}{2}\left(\frac{\gamma}{m}\right)^2}. \tag{7}$$

Figure 4 shows that the resonance frequency shift $(\omega' - \omega_0)/(2\pi)$ can be extremely large. One step farther below 400 nm, a complete freezing of the CL oscillation would have been observed. This was precluded by the residual angular misalignment discussed above. Taking into account the misalignment obtained from Fig. 3, we can quantitatively model the data in Fig. 4 without any adjustable parameter whatsoever. Therefore, besides the CL width that governs the Q factor behavior at large scale (Fig. 3), another shorter characteristic length is here emphasized in the submicron range, i.e., $d_{\text{crit.}} = \frac{\sqrt{2}\eta}{m}\frac{A}{\omega_0}$ (around 500 nm in our case), which is the gap width canceling the resonance frequency in Eq. (7). This charac-

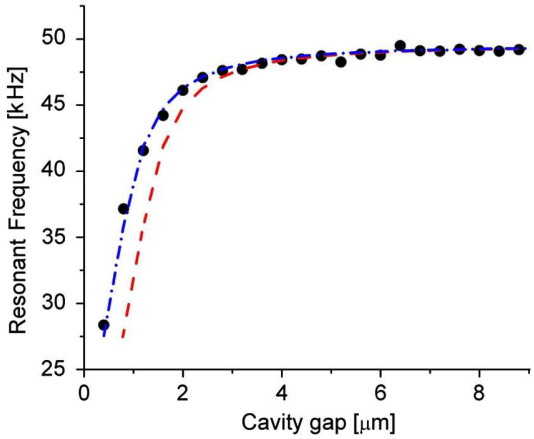

FIG. 4 (color online). The resonance frequency as function of the cavity gap in the small gap regime. As in Fig. 3, the red dashed (blue dash-dotted) curve is the prediction of the NS model for the perfectly aligned (slightly misaligned) cavity.

teristic length is determined by the CL dynamics and the fluid viscosity.

In conclusion, we have presented high sensitivity measurements of the damping of a thermally driven CL in a simple fluid confined in a microcavity formed by this CL facing an infinite wall. As the cavity length decreases, the fluid confinement induces a dramatic damping of the CL Brownian motion which can lead to its complete freezing at small gaps. A consequence of our work is that micro- or nano-oscillators can either present high Q factors or be overdamped systems depending on their actual geometry, resonance frequency, oscillator substrate gap, and, of course, ambient viscosity. These findings may impact the design of modern NEMS and microfluidic devices since the $1/d$ dependence strongly reduces dissipation even for separations d as large as thousands of mean free path $\bar{\lambda}$ (see Fig. 3). This $1/d$ behavior can be furthermore described by solving the Navier-Stokes equation with perfect solid-fluid slip boundary conditions. The agreement between experiment and our model is found over a broad range of cavity lengths, including the submicron range. Interesting extensions of the present work include the study of parameters affecting boundary conditions, such as external actuation of CLs (to obtain large oscillation amplitude) [30], nanostructuration [4], and surface chemical properties [8].

We are grateful to Giovanni Ghigliotti for helpful discussions. Our thin etched optical fiber has been prepared by Jean-Francois Motte. This research was partly supported by a "Carnot-NEMS" collaborative grant between CEA-LETI and Institut Néel.

[1] Y. T. Yang *et al.*, Nano Lett. **6**, 583 (2006).
[2] H. J. Mamina and D. Rugar, Appl. Phys. Lett. **79**, 3358 (2001).
[3] K. Karrai, Nature (London) **444**, 41 (2006); C. Metzger *et al.*, Phys. Rev. Lett. **101**, 133903 (2008); G. Jourdan, F. Comin, and J. Chevrier, Phys. Rev. Lett. **101**, 133904 (2008).
[4] Mo Li *et al.*, Nature Nanotech. **2**, 114 (2007).
[5] C. Cottin-Bizonne *et al.*, Phys. Rev. Lett. **94**, 056102 (2005).
[6] W. Y. Shih *et al.*, J. Appl. Phys. **89**, 1497 (2001).
[7] P. K. Hansma *et al.*, Appl. Phys. Lett. **64**, 1738 (1994).
[8] A. Maali *et al.*, Phys. Rev. Lett. **96**, 086105 (2006).
[9] A. Raman *et al.*, Nanotoday **3**, 20 (2008).
[10] T. Ando *et al.*, Prog. Surf. Sci. **83**, 337 (2008).
[11] J. N. Munday *et al.*, Phys. Rev. A **78**, 032109 (2008).
[12] J. N. Munday, F. Capasso, and A. Parsegian, Nature (London) **457**, 170 (2009).
[13] L. Bellon, J. Appl. Phys. **104**, 104906 (2008).
[14] R. B. Bhiladvala and Z. J. Wang, Phys. Rev. E **69**, 036307 (2004).
[15] C. P. Green and J. E. Sader, J. Appl. Phys. **98**, 114 913 (2005).
[16] T. Naik *et al.*, Sens. Actuators A: Phys. **102**, 240 (2003).
[17] M. R. Paul and M. C. Cross, Phys. Rev. Lett. **92**, 235501 (2004).
[18] J. Dorignac *et al.*, Phys. Rev. Lett. **96**, 186105 (2006).
[19] S. Basak *et al.*, J. Appl. Phys. **99**, 114 906 (2006).
[20] R. C. Tung *et al.*, J. Appl. Phys. **104**, 114 905 (2008).
[21] P. Tabeling, *Introduction to Microfluidics* (Oxford University Press, Oxford, 2006).
[22] D. Y. C. Chan, and R. G. Horn, J. Chem. Phys. **83**, 5311 (1985).
[23] O. I. Vinogradova, Langmuir **11**, 2213 (1995).
[24] A. Maali and B. Bhushan, Phys. Rev. E **78**, 027302 (2008).
[25] The CL tip has been removed by focused-ion-beam milling.
[26] S. Goldstein, Annu. Rev. Fluid Mech. **1**, 1 (1969).
[27] The CL dimensions have been measured by electron microscopy. The air viscosity was taken as $\eta \simeq 1.8 \times 10^{-5}$ kg/ms. The CL stiffness $k = 0.0396$ N/m has been experimentally determined from Fig. 2 using the energy equipartition theorem.
[28] B. V. Derjaguin *et al.*, Q. Rev. Chem. Soc. **10**, 295 (1956).
[29] Following Ref. [8], the ultrasmall CL oscillation precludes any mass addition to the lever, in contrast with Ref. [16] where this effect is dominant for actuated macroscopic levers.
[30] R. A. Bidkar *et al.*, Appl. Phys. Lett. **94**, 163 117 (2009).

Appendix B

X-ray pushing of a mechanical microswing

Nanotechnology **19** (2008) 445501 (5pp) doi:10.1088/0957-4484/19/44/445501

X-ray pushing of a mechanical microswing

A Siria[1,2], M S Rodrigues[3], O Dhez[3], W Schwartz[1,2], G Torricelli[4], S LeDenmat[3], N Rochat[2], G Auvert[2,5], O Bikondoa[3], T H Metzger[3], D Wermeille[3], R Felici[3], F Comin[3] and J Chevrier[1]

[1] Institut Néel, CNRS-Université Joseph Fourier Grenoble, BP 166, F-38042 Grenoble Cedex 9, France
[2] CEA-LETI, 17 Avenue des Martyrs, F-38054 Grenoble Cedex 9, France
[3] ESRF, 6 rue Jules Horowitz, F-38043 Grenoble Cedex 9, France
[4] Department of Physics and Astronomy, University of Leicester, University Road, Leicester LE1 7RH, UK
[5] STMicroelectronics, 850 rue Jean Monnet, F-38926 Crolles, France

Received 28 May 2008, in final form 18 August 2008
Published 26 September 2008
Online at stacks.iop.org/Nano/19/445501

Abstract
We report here for the first time the combination of x-ray synchrotron light and a micro-electro-mechanical system (MEMS). We show how it is possible to modulate in real time a MEMS mass distribution to induce a nanometric and tunable mechanical oscillation. The quantitative experimental demonstration we present here uses periodic thermal dilatation of a Ge microcrystal attached to a Si microlever, induced by controlled absorption of an intensity modulated x-ray microbeam. The mechanism proposed can be envisaged either for the detection of small heat flux or for the actuation of a mechanical system.

(Some figures in this article are in colour only in the electronic version)

Nanoelectromechanical systems (NEMS) are among the best candidates to measure interactions and accelerations at the nanoscale [1–6], especially when resonating oscillators are used with high quality factor [7–9]. Indeed NEMS and MEMS have been used for the detection of the mechanical effects of light and radiation pressure [10] and thermal switching effects in a lever [11] have been shown as actuation mechanisms for mechanical systems. We show here, for the first time, the interaction between a mechanical system and x-rays. To demonstrate this interaction efficiency we show how mechanical nanodisplacements of a MEMS are triggered using modulated x-ray microbeams. The MEMS is a microswing constituted by a Ge microcrystal attached to a Si microcantilever. The interaction is mediated by Ge absorption of the intensity modulated x-ray microbeam impinging on the microcrystal. We show then that radiation pressure or thermal-strain-induced effects are not effective enough to induce the observed oscillation amplitude in our experiments. The measured oscillation amplitudes can be understood by the changes of the mass distribution at the nanoscale induced by controlled thermal dilation. The small but finite thermal expansion of the Ge microcrystal is large enough to force a nanodisplacement of the Ge microcrystal's center of mass (COM). This mechanism is based on the small temperature variation induced by a local heating absorption (20 K mW^{-1}) and, as a consequence, this strategy can be used as a local thermal flux sensor. Moreover this mechanism represents a new actuation scheme for NEMS and MEMS and we show how this effect can be potentially scaled down to offer an actuation mechanism on the nanoscale.

The experimental set-up is presented in figure 1. The microswing position is measured through the interference between the light reflected from the back of the lever and from a cleaved fiber end. This experimental set-up has been shown to produce a sub-Ångström precision in position measurements [5, 6, 11]. SEM images of the microswings used are shown in figures 1(b) and (c). The first Ge microcrystal in figure 1(b) has been directly cut from a Ge wafer by a focused ion beam (FIB). In order to fabricate the micro-oscillator, a cubic-like germanium crystal has been etched from a germanium wafer using the FIB Strata400 from FEI. The cube was welded to the cantilever, in a symmetrical position, using localized FIB deposition of metal. The cubic Ge crystal is 43 μm thick. The lever is a standard silicon AFM cantilever whose dimensions are 350 × 35 × 2 μm^3. This lever has no metallic coating. The second Ge microcrystal is about 23 μm thick (figure 1(c)). It has been manually glued on the side of the cantilever in a very asymmetrical position. For asymmetrically mounted crystals, two types of levers have been used: one bare and another with a metallic coating.

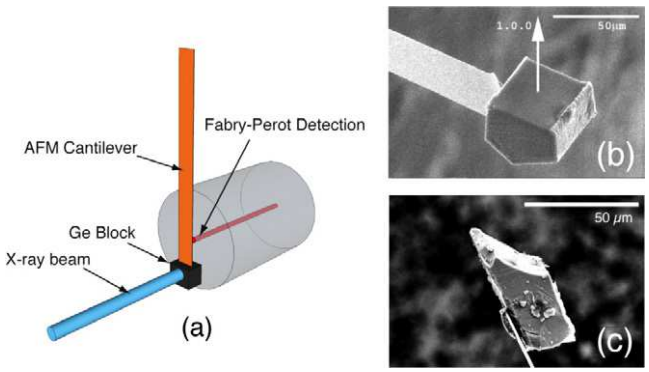

Figure 1. (a) Experimental set-up. The small cylinder (blue ray) is the x-ray beam on the Ge microcrystal at the Si lever end. The big (gray) cylinder represents the optical fiber and the inner (red) ray is the laser beam used to detect the lever position with sub-Ångström precision. ((b) and (c)) SEM images of the Ge cubes glued on the Si levers. In (b) the cut and soldered Ge crystal, using a focused ion beam, has been positioned at the end of the lever in a symmetrical position. In (c) a Ge crystal has been manually glued on the side in a very asymmetrical position.

The experiments were performed at the European Synchrotron Radiation Facility (ESRF). The beamlines involved were the anomalous scattering beamline (ID01) and surface science x-ray diffraction (SXRD) beamline (ID03). In ID01 the radiation from the undulators can be tuned from 2.5 to 40 keV with a Si(111) double-crystal monochromator. Focusing is achieved by using beryllium compound refractive lenses (CRLs) [12]. The effective focus size is $\approx 4 \times 6\ \mu m^2$ with $\approx 10^{10}$ photons s^{-1} on the focal spot. At the SXRD beamline the photons were tuned at the Ge K edge using a liquid-nitrogen-cooled monolithic double-crystal Si(111) monochromator. The beam was focused on the sample by a Kirkpatrick–Baez (KB) mirror system located 43 m from the photon source. The beam size at the sample, 1 m from the KB system, is $\approx 3 \times 5\ \mu m^2$ with $\approx 10^{12}$ photons s^{-1} on the focal spot.

Table 1. Comparison between the calculated resonant frequency and the measured value for the resonant peaks presented in figure 2.

Mechanical system	Simulated resonant frequency (Hz)	Measured resonant frequency (Hz)
2 (a)	2110	2140
2 (b)	3560	3750
2 ((c)–(d))	1410	1270

Figure 2 presents the mechanical response measured around the first resonance frequency ω_0 for different geometries and experimental set-ups. In table 1 a comparison between the simulated resonant frequency values and the measured ones is presented. The calculated values are obtained using the hypothesis of a simple 1D harmonic oscillator.

In figure 2 the intensity of the x-ray beam impacting on the Ge crystal is modulated at a frequency ω sweeping through the lever resonant frequency ω_0. For x-ray energies below the absorption edge, the lever is already forced to oscillate with amplitudes larger than the thermally induced noise. For energies above the absorption edge we observe an increase of oscillation amplitude for all geometries. The amount of this increase as a function of geometry, microswing characteristic and the position of the Ge microcrystal is the basis of our findings.

Figure 3 reports the mechanical response of the cantilever at resonance, when the x-ray energy is scanned through the germanium K-edge energy. The mechanical response of the microswing matches well the XAS reference spectrum of germanium [13]. The two curves have been normalized below the edge and in the continuum atomic part above the edge.

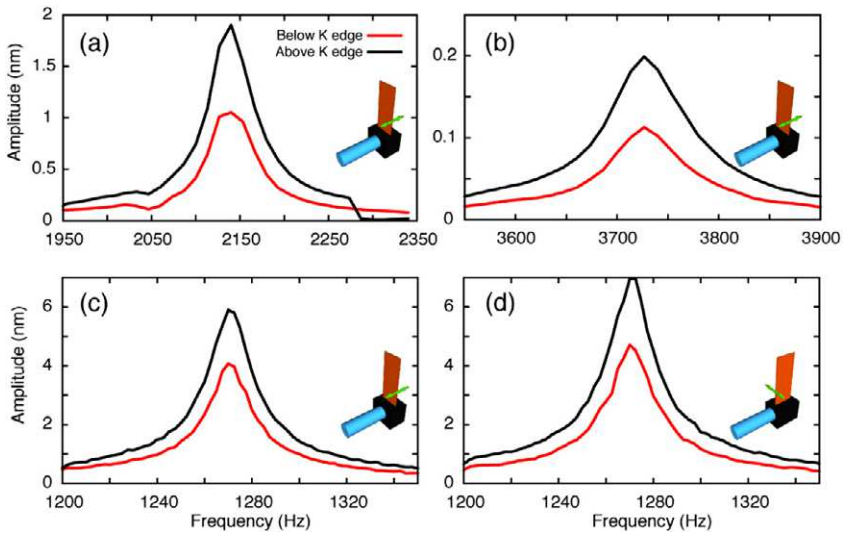

Figure 2. Measured resonance curve of the first oscillating mode for all levers. In gray (red) the x-ray beam energy is set below the K1s edge ($E_{ph} = 11.07$ keV), while in black it is set at the K1s edge ($E_{ph} = 11.103$ keV). (a) Uncoated cantilever ($k = 0.025$ N m^{-1}, $Q = 86$, $I_0 = 7.4 \times 10^{10}$ ph s^{-1}) with Ge block glued on the side and x-ray beam parallel to the oscillation direction. (b) Coated cantilever ($k = 0.027$ N m^{-1}, $Q = 60$, $I_0 = 3.5 \times 10^{10}$ ph s^{-1}) with Ge block glued on the side and x-ray beam parallel to the oscillation direction. (c) Uncoated cantilever ($k = 0.135$ N m^{-1}, $Q = 75$, $I_0 = 2.4 \times 10^{12}$ ph s^{-1}) with Ge block glued below and x-ray beam parallel to the oscillation direction. (d) Same as in (c) with x-ray beam perpendicular to the oscillation direction.

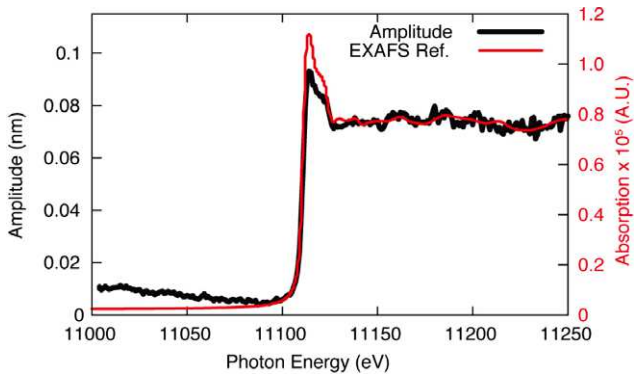

Figure 3. Cantilever oscillation amplitude as a function of beam energy. We show (in black) our experimental data with superposed (and in red) the handbook reference EXAFS spectrum at the Ge K edge.

Even though a mechanical detection of EXAFS has already been shown [14], this is the first time utilizing an MEMS. On the basis of the experimental evidence presented in figure 2, we can identify the oscillation driving force. Radiation pressure can be ruled out, as the oscillation is the same whatever the direction of the beam (figures 2(c) and (d)) with respect to the oscillation direction.

From figures 2 and 3 it is evident that the oscillation amplitude is a function of the absorption cross section. Indeed, its spectrum follows well the absorption coefficient for bulk germanium. We then explored the hypothesis that the absorbed energy is promptly turned into heat, leading to a temperature increase dependent on how the heat is evacuated.

As a first approximation, the number of photons that contributes to a temperature increase is the difference between the number of absorbed photons and fluorescence photons that escape from the sample considering that the fluorescence emission can be photoelectrically reabsorbed. The overall number of photons I_h that induce the temperature increase is then

$$I_h = I_0(1 - T_{\mathrm{Ge}}^{\mathrm{E}})(1 - w_{\mathrm{Ge}}^{\mathrm{E}} T_{w_{\mathrm{Ge}}}^{E_{\mathrm{f}}}) \tag{1}$$

where I_0 is the incoming intensity, $T_{\mathrm{Ge}}^{\mathrm{E}}$ the Ge transmission coefficient, a function of the photon energy and sample thickness, and $w_{\mathrm{Ge}}^{\mathrm{E}}$ the fluorescence yield. $T_{w_{\mathrm{Ge}}}^{E_{\mathrm{f}}}$ is the rate of fluorescence at energy E_{f} which escapes from the sample. This last coefficient is dependent on sample thickness.

At energies below the Ge K edge, the main process is the Auger electron production [15]. Most of the absorbed photons then contribute to the heating because of the short mean free path (a few nanometers) of the Auger electrons and their cascades. At energies higher than the Ge K edge the absorbed photons generate fluorescence, Coster–Kronig and Auger electrons.

The decreased amplitude of the XAFS peak and oscillations after the K edge with respect to the reference spectra are due to this intrinsic self-absorption effect. In table 2 the absorbed photon flux I_h is calculated for two lever/crystal configurations, for two x-ray beam directions, and for coated and uncoated levers. The ratio of the measured oscillation amplitudes $x(\omega_0)$ above and below the K-edge energy is consistent with the ratio of absorbed photons. The temperature increase ΔT can be calculated taking into account the overall energy deposited in the crystal and the heat flow through the lever (cooling by radiation and convection is negligible here). The absorbed power W is then

$$W = C\dot{T}(t) + G(T(t) - T_0) \tag{2}$$

$$T(t) = T_0 + \frac{W}{G}\left(1 - \mathrm{e}^{-\frac{G}{C}t}\right) \tag{3}$$

where T_0 is the ambient temperature and $T(t)$ the block temperature as a function of time. $\Delta T(\omega)$ is then

$$\Delta T(\omega) = \frac{W}{G}\frac{1}{(1 + \omega\tau)} \tag{4}$$

$$\tau = \frac{C}{G} \tag{5}$$

ω is the beam chopper frequency and τ is the ratio between the thermal capacity of the Ge block and the thermal conductivity of the Si lever. For the uncoated and coated levers of figures 2(a) and (b) the experimental conditions are nearly identical whereas the oscillation amplitude is 10 times larger in 2(a) than in 2(b). This difference can be described using those last equations. The presence of the metallic coating increases the thermal conductivity G of the system and therefore induces a consequent decrease of ΔT compared to the uncoated lever.

However, this description cannot explain the difference of the amplitude of oscillation between figures 2(a) and (c). The oscillation amplitude in figure 2(c) is 3 times larger than in 2(c) against a photon flux 40 times bigger and an absorption rate 25% higher because of the difference in Ge crystal dimensions. The difference in the mechanical properties of the cantilever (2(a) $k = 0.025$ N m^{-1}, 2(c) $k = 0.135$ N m^{-1}) cannot explain such a large discrepancy. However, the position of the Ge crystal and this symmetry with respect to the lever has not been considered. This remark is essential to the conclusion of this paper. We show that the thermally induced change in the distance between the Ge crystal COM and the lever axis controls the system dynamics.

The thermally induced change in the COM position is determined by

$$\Delta l(\omega) = l_0 \alpha \Delta T(\omega) \tag{6}$$

where l_0 is the distance between the block COM and the lever axis and α the linear thermal expansion coefficient.

For a simple 1D mechanical oscillator the oscillation amplitude is given by

$$\begin{aligned} x(\omega) &= x_i(\omega)\sqrt{|\psi(\omega)|^2} \\ &= x_i(\omega)\sqrt{\frac{\omega_0^2 Q^2}{(Q^2/\omega_0^2)(\omega^2 - \omega_0^2)^2 + \omega^2}} \end{aligned} \tag{7}$$

where $\psi(\omega)$ is the oscillator transfer function. Here, $x_i(\omega)$ corresponds to $\Delta l(\omega)$.

Considering the MEMS as the whole system constituted by the cantilever and the Ge microcrystal, the induced increase in the Ge crystal size can be read as an induced change in the mass distribution of the mechanical system.

Table 2. Correspondence between absorbed photon and oscillation amplitude for different levers and geometries. The top part presents the comparison for a coated and an uncoated lever with an asymmetrical geometry like in figure 1(c). The x-ray beam is here parallel to the direction of oscillation. The second part presents the comparison for an uncoated lever with a symmetric geometry. The x-ray beam is here either parallel or perpendicular to the direction of oscillation.

$l_0 = 23\ \mu$m					Uncoated	Coated
$E_{\rm ph}$	$T_{\rm Ge}$	$w_{\rm Ge}$	$T_{w_{\rm Ge}}$	I_h	$x(\omega_0)$ (nm)	$x(\omega_0)$ (nm)
11.07	0.72	0	—	0.28 I_0	1.053	0.113
11.103	0.083	0.535	0.83	0.51 I_0	1.902	0.199
			Ratio	1.82	1.81	1.76
$l_0 = 43\ \mu$m					Para.	Perp.
$E_{\rm ph}$	$T_{\rm Ge}$	$w_{\rm Ge}$	$T_{w_{\rm Ge}}$	I_h	$x(\omega_0)$	$x(\omega_0)$
11.07	0.54	0	—	0.47 I_0	4.066	4.713
11.103	0.009	0.535	0.33	0.63 I_0	5.898	6.959
			Ratio	1.34	1.47	1.48

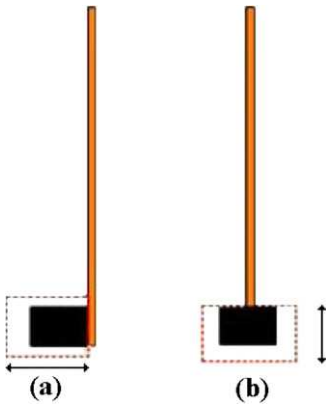

Figure 4. Schema of the actuation mechanism. In (a) is presented a very asymmetric configuration and in (b) a symmetric geometry. The dotted squares represent the Ge crystal thermal expansion and the black arrows indicate the direction of the effective displacement of the Ge crystal COM.

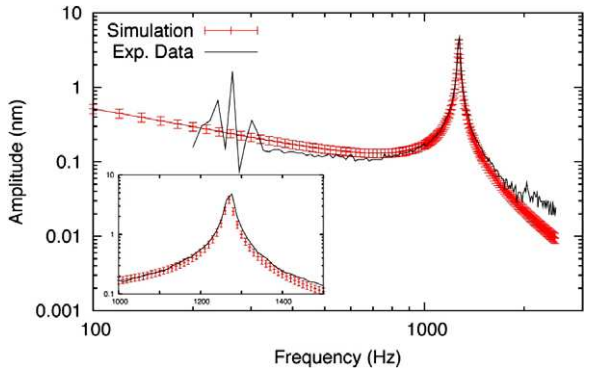

Figure 5. Response function of the lever shown in figure 1(b). The (black) curve presented is the measured amplitude of the lever oscillation as the beam intensity is modulated from 100 to 2500 Hz. The superposed (red) curve is the calculated expression using experimental parameters. The error bar on the theoretical (red) curve has been determined using Brownian motion. The theoretical (red) curve calculation involves the misalignment of the Ge microcrystal on the Si lever as the single adjustable parameter. In the inset a zoom on the resonant peak is presented.

In the hypothesis of uniform temperature in the Ge block the displacement of the COM with respect to the lever axis is easily calculated using equation (6). As is described in figure 4, when the Ge cube is glued on the side of the lever, the thermal expansion induces a COM displacement along the cantilever oscillation direction. This is no longer true when the block is welded below the lever in a symmetric configuration; in this case the effective COM displacement along the lever oscillation direction is negligible. As a consequence, from the expression presented in equation (7), the oscillation amplitude in the asymmetric configuration is expected to be much more important than in the symmetric one. The use of two Ge crystals mounted in different positions is then crucial to validate the actuation mechanism based on COM-induced nanodisplacement.

For the system in figure 1(c), $l_0 = 13\ \mu$m, close to half the Ge crystal thickness. For an intensity $I_0 = 7.4\times10^{10}$ ph s^{-1} the temperature increase is found to be $\Delta T(\omega_0) = 0.24$ K. Using $\alpha_{\rm Ge} = 5.9 \times 10^{-6}$ K^{-1}, according to equation (6), the induced COM displacement is $\Delta l(\omega_0) = 19$ pm. Using equation (7), with the measured quality factor of 86 and the amplitude at resonance of 1.9 nm, the COM displacement is found to be $\Delta l(\omega_0) = 22$ pm, which is consistent with the value calculated from equation (6). The error bar on the measured lever position is determined by the thermal fluctuations of the lever position and is $x_i(k_{\rm B}T) = 1.6$ pm.

The system in figure 1(b) presents a much more symmetrical geometry. The l_0 value in this case must be smaller than the one in the case of figure 1(c), but it is not easily measurable. A rough estimate of the residual misalignment between the COM of the Ge microcrystal and the Si lever axis is the uncertainty in the FIB positioning device, which is about 1 μm.

The distance l_0 that best fits the data while all other parameters are known is 1.5 μm, which is indeed close to the precision of the FIB motor. The comparison between the model (equation (7)) and the measured oscillation is presented in figure 5 as the excitation frequency is swept from 100 to 2500 Hz. The agreement further establishes that the thermally forced displacement of the COM is at the origin of the observed lever oscillation equipped with the Ge crystal. Results for all configurations are then consistently explained using this single actuation mechanism. The MEMS actuation mechanism shown here can be extended to NEMS actuation. Considering

an Si lever of $1 \times 0.1 \times 0.1\ \mu m^3$ and a Ge block of $100 \times 100 \times 100\ nm^3$ with a thermal conductivity of $G = 3.7 \times 10^{-8}\ W\ K^{-1}$ and thermal capacity of $C = 1.7 \times 10^{-15}\ J\ K^{-1}$ [16] leads, according to equation (4), to a substantial temperature increase at a frequency in the MHz regime, typical for the resonance of such an NEMS. If a 1 μW laser beam is absorbed in this Ge block, the induced thermal expansion will be several pm. As NEMS with lateral sizes close to 100 nm can exhibit quality factors of 1000, a forced COM oscillation with an amplitude of several pm can result at resonance in a nanometric NEMS oscillation amplitude. This is far larger than the thermally induced fluctuations of the NEMS position. This strategy of NEMS excitation can be compared to photothermal actuation based on thermally induced strain [17–23]. The essential difference is in the origin of the NEMS displacement. This origin is, in the mechanism that we propose, a strain-free thermally induced change in mass spatial distribution in an asymmetric structure.

We have demonstrated that the COM displacement mechanism is a very sensitive method to detect local temperature variation induced by low heating absorption. In the case of a highly asymmetric geometry we have shown it to be sensitive to an absorbed power of 10 μW while the detection limit, given by the thermal noise ($k_B T$), is below 1 μW. This set-up is then a very good candidate for measuring low thermal flux in the near-field condition with high accuracy [24].

Furthermore the use of MEMS as Si single-crystal micro-oscillators can provide x-ray choppers at high frequencies. Using diffraction, an Si single-crystal MEMS appears to be a good candidate for the high frequency manipulation of x-ray microbeams. This could offer new tools either to change the phase x-ray wavefront, or to produce a rapidly modulated intensity of x-ray beams that are so important in real-time studies of fast dynamical processes in chemistry and in biology [25].

References

[1] Li M, Tang H X and Roukes M L 2007 *Nature Nanotechnol.* **2** 114–20
[2] Ekinci K L, Huang X M H and Roukes M L 2004 *Appl. Phys. Lett.* **84** 4469–71
[3] Yang Y T *et al* 2006 *Nano Lett.* **6** 583–6
[4] Mamin H J and Rugar D 2001 *Appl. Phys. Lett.* **79** 3358–60
[5] Cleland A N and Roukes M L 1998 *Nature* **392** 160–2
[6] Rugar D, Budakian R, Mamin H J and Chui W 2004 *Nature* **430** 329–32
[7] Burg T P *et al* 2007 *Nature* **446** 1066–9
[8] Verbridge S S *et al* 2006 *J. Appl. Phys.* **99** 124304
[9] Zwickl B M *et al* 2007 arXiv:0711.2263v1
[10] Arcizet O *et al* 2006 *Nature* **444** 71–4
[11] Metzger C H and Karrai K 2004 *Nature* **432** 1002–5
[12] Snigirev A, Kohn V, Snigireva I and Lengerer B 1996 *Nature* **384** 49–51
[13] EXAFS-Data-Base-(Standards) (www.nsls.bnl.gov/beamlines/x18b/data.htm)
[14] Masujima T *et al* 1989 *Rev. Sci. Instrum.* **60** 2522–4
[15] Krause M O 1979 *J. Phys. Chem. Ref. Data* **8** 307–27
[16] Li D *et al* 2003 *Appl. Phys. Lett.* **83** 2934–6
[17] Lavrik N V and Datskos P G 2003 *Appl. Phys. Lett.* **82** 2697–9
[18] Sampathkumar A, Murray T W and Ekinci K L 2006 *Appl. Phys. Lett.* **88** 2231041–3
[19] Koenig D R, Metzger C, Camerer S and Kotthaus J P 2006 *Nanotechnology* **17** 5260–3
[20] Zhu Y, Corigliano A and Espinosa H D 2006 *J. Micromech. Microeng.* **16** 242–53
[21] Geisberger A A, Sarkar M, Ellis M and Skidmore G 2003 *J. Microelectromech. Syst.* **12** 513–23
[22] Que L, Park J S and Gianchandani Y B 2001 *J. Microelectromech. Syst.* **10** 247–54
[23] Park J S, Chu L L, Oliver A and Gianchandani Y B 2001 *J. Microelectromech. Syst.* **10** 255–62
[24] Mulet *et al* 2001 *Appl. Phys. Lett.* **78** 2931–3
[25] Wulff M *et al* 1997 *Nucl. Instrum. Methods Phys. Res.* A **398** 69–84

Appendix C

A MEMS based high frequency X-ray chopper

Nanotechnology **20** (2009) 175501 (4pp) doi:10.1088/0957-4484/20/17/175501

A MEMS-based high frequency x-ray chopper

A Siria[1,2], O Dhez[3], W Schwartz[1,2], G Torricelli[4], F Comin[3] and J Chevrier[1]

[1] Institut Néel, CNRS-Université Joseph Fourier Grenoble, BP 166, F-38042 Grenoble Cedex 9, France
[2] CEA/LETI-MINATEC, 17 Avenue des Martyrs, F-38054 Grenoble Cedex 9, France
[3] ESRF, 6 rue Jules Horowitz, F-38043 Grenoble Cedex 9, France
[4] Department of Physics and Astronomy, University of Leicester, University Road, Leicester LE1 7RH, UK

Received 18 November 2008, in final form 30 January 2009
Published 3 April 2009
Online at stacks.iop.org/Nano/20/175501

Abstract
Time-resolved x-ray experiments require intensity modulation at high frequencies (advanced rotating choppers have nowadays reached the kHz range). We here demonstrate that a silicon microlever oscillating at 13 kHz with nanometric amplitude can be used as a high frequency x-ray chopper. We claim that using micro-and nanoelectromechanical systems (MEMS and NEMS), it will be possible to achieve higher frequencies in excess of hundreds of megahertz. Working at such a frequency can open a wealth of possibilities in chemistry, biology and physics time-resolved experiments.

(Some figures in this article are in colour only in the electronic version)

Nowadays many experiments in physics, biology, chemistry and material science require irradiation of a sample by a short burst of x-ray radiation to study in detail the time response of the sample under a particular excitation [1–3]. X-ray techniques are extremely important to investigate the chemistry and structure of materials [4, 5]. In a typical experiment the system to be analyzed is excited by a short x-ray burst and information about the response is obtained by studying the fluorescence emitted during the system's de-excitation [6, 7].

In a pump–probe experiment, the sample is pumped into a metastable state by laser excitation and a delayed x-ray pulse is used to monitor the time evolution of the system [8–10]. A common aspect of these two kinds of experiment is the required duration of the x-ray pulse. Since the timescale involved can be smaller than a microsecond, x-ray pulses with durations less than a microsecond are then required [11–13]. Short-duration x-ray bursts are typically produced when a continuous x-ray beam passes through a mechanical shutter that is open for a short time [14]. The major limitations of rotating mechanical shutters are the size and the operational environment required. They actually need to work under vacuum conditions, especially if a very short x-ray pulse has to be realized.

The interactions between x-ray techniques and MEMS technology have been recently shown in work where a modulated x-ray beam has been used to excite a mechanical system around its first-order resonance [15]. At variance we show here how the inverse mechanism can be used to modulate an x-ray beam. The simplest MEMS that can be imagined is a single-crystal silicon cantilever. We used the controlled oscillations of this tiny single crystal to get periodically in and out of the Bragg conditions. This is the basic principle of this high frequency mechanical x-ray chopper.

Figure 1 shows schematically the experimental set-up. The mechanical system used during the experiment is a standard Si(100) AFM cantilever with dimensions $300 \times 35 \times 2\ \mu m^3$. The cantilever displacement is measured by the interference between the light reflected from the end of a cleaved optic fiber and the beam reflected by the back of the lever. This interferometric technique has been shown to lead to sub-ångström precision in position measurement [15–18].

The experiment has been performed at the European Synchrotron Radiation Facility. The beamline involved was the surface x-ray diffraction (SXRD) beamline (ID03). The incoming x-ray beam set at 18.98 keV is impinging on the cantilever at rest at the Bragg condition and the x-ray photodetector is positioned at the correspondent 2Θ angle. At the SXRD beamline the beam was monochromatized by a liquid-nitrogen-cooled monolithic Si(111) double crystal,

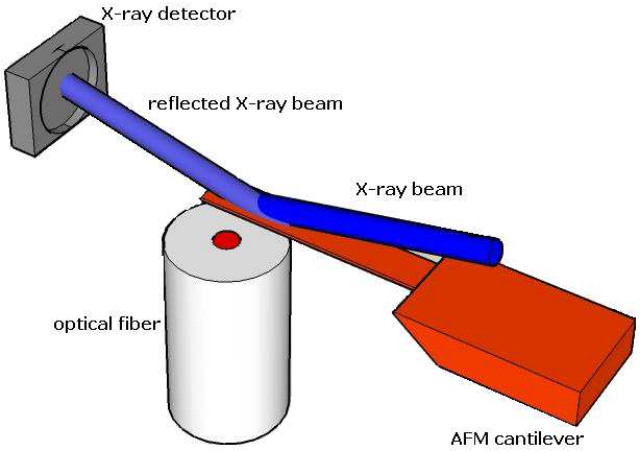

Figure 1. Experimental set-up. The AFM cantilever used to stop or transmit the dark blue x-ray beam impacting around the Bragg angle is represented in orange. The reflection of the x-ray beam is detected with a photodiode. The white cylinder represents the optical fiber for the interferometric detection of the lever position with sub-ångström precision.

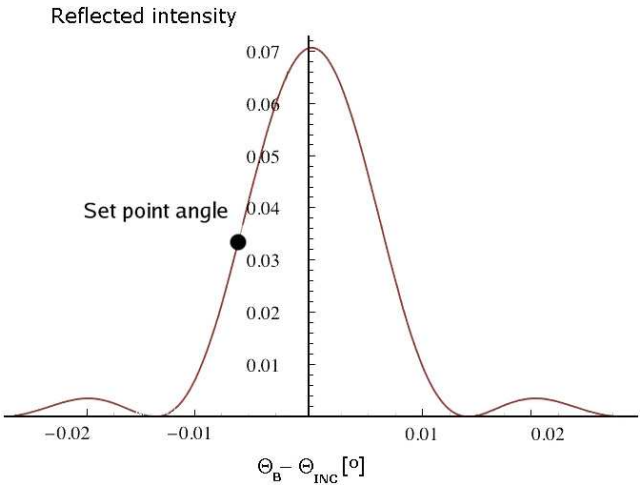

Figure 2. Theoretical Si(400) Bragg profile for a 2 μm thick perfect Si crystal in the kinematic approximation. The black dot indicates the flex point used as the reference position of the silicon cantilever.

resulting in an energy resolution $\frac{\Delta E}{E} \approx 10^{-4}$. To maintain the collimation of the source no focusing system has been used. The beam delivered by the monochromator, at the sample located 44 m from the source, has a size of $\approx 50 \times 50\ \mu\text{m}^2$ with $\approx 10^{10}$ photons s^{-1} and a divergence of the order of $\approx 10\ \mu$rad, a few 10^{-4} degrees.

When the cantilever is at rest in Bragg conditions, the photodiode detects a constant flux of photons. When the AFM lever is periodically excited by a piezoelectric ceramic, the x-ray incidence angle is consequently modified by the lever motion. If the lever oscillation amplitude is larger than the Bragg peak width, the cantilever will periodically sweep through the Bragg conditions. A periodically modulated current will be measured at the output of the photodiode.

The chopper uses the diffraction properties of a silicon crystal. The average angle is set around the Bragg angle. Working at higher energies will impose more grazing angles of incidence. When grazing incidence is getting closer to the critical incidence angle the chopper will behave as a mirror and one could better envisage passing at higher-order reflections, with the consequent loss of efficiency.

During this experiment the x-ray spot size is larger than the cantilever width. The intensity diffracted in the photodiode is consequently lower than the incoming one. Cantilevers of larger width will permit us to handle larger beams without changing the essentials of the experiment. For even larger beams it will be necessary to pass to pixellated systems as will be discussed in the conclusions.

Figure 2 presents the theoretical Bragg peak for a Si(400) reflection, calculated in the hypothesis of a perfect 2 μm thick single crystal in the kinematic approximation [19, 20]. It is worth noting that, due to the small thickness of the cantilever Si single crystal (2 μm, much smaller than the extinction length), the Bragg (400) reflection is very broad. In our case the Bragg width is $\approx$100 times larger than the incoming x-ray beam divergence. The oscillating cantilever will operate then as a rotating mirror chopper on the incoming beam.

Considering the shape of the Bragg peak, the x-ray intensity modulation is maximum when the set-point angle of the x-rays on the lever is set in correspondence of the flex point of the Bragg peak (see the black point in figure 2); in this condition, moreover, the diffracted signal, when the cantilever is oscillating with modulation ω, is modulated at ω and not at 2ω, as it would be if the set-point is at the maximum of the curve.

The amplitude of the photon flux oscillation is thus directly constrained by the oscillation amplitude of the cantilever.

As a first step in the analysis we use the so-called single-mode approximation of the AFM lever behavior. The lever can be approximated with a 1D harmonic oscillator whose response to a modulated applied force is characterized by its transfer function:

$$x(\omega) = \frac{F(\omega)}{m} \frac{1}{\sqrt{(\omega_0^2 - \omega^2)^2 + \gamma^2\omega^2}} \tag{1}$$

$$\tan\alpha = \frac{\gamma\omega}{\omega_0^2 - \omega^2} \tag{2}$$

where ω is the applied force frequency, ω_0 the oscillator resonant frequency and γ the system damping factor. Equation (1) gives the lever oscillation amplitude when a modulated force $F(\omega)$ is applied; equation (2) gives the phase lag of the cantilever oscillation with respect to the applied force. In figure 3(a) is shown the cantilever oscillation amplitude (black) and phase lag (red) as a function of frequency when the mechanical system is mechanically excited at resonance. This is measured using the optical fiber as shown in figure 1.

Figure 3(b) shows the current (amplitude and phase) at the output of the x-ray photodiode as a function of the frequency. For the specific chosen case the current has the same functional shape of the cantilever mechanical response presented in 3(a).

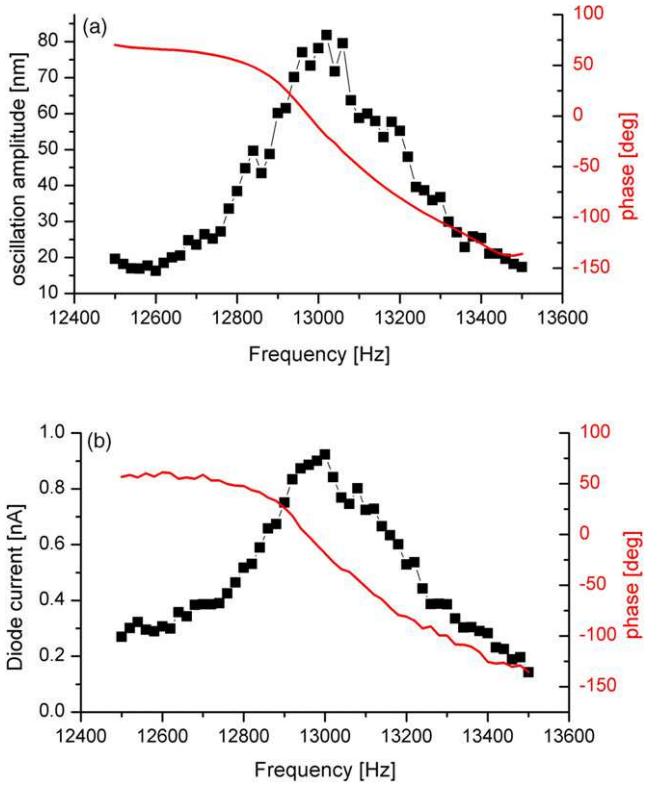

Figure 3. (a) Optically measured mechanical response of the AFM cantilever when it is mechanically excited around its first resonant frequency of 13 kHz. (b) Diode photocurrent measured by the photodiode at the 2θ Bragg position. In (a) and (b) the black (dotted) curve represents the oscillation amplitude and the red (line) curve represents the phase lag.

Figure 4 presents the photodiode output as a function of the excitation frequency for different excitation amplitudes. The nonlinear behavior for the largest cantilever excitation amplitude is due to the cantilever bending induced by the oscillation. In other words, at any given time the x-ray beam does not find a specific incidence angle but an angle gradient over the cantilever.

The AFM cantilever can be quantitatively described with a vibrating beam whose dynamical deflection is well described by the Euler–Bernoulli equation [21, 22]:

$$\rho(x)\frac{\partial^2 U(x,t)}{\partial t^2} + EI\frac{\partial^4 U(x,t)}{\partial x^4} = f(x,t) \tag{3}$$

where $U(x,t)$ is the cantilever profile as a function of time and position, $\rho(x)$ is the material density, E the Young's modulus and $I = \frac{t^3 w}{12}$ the inertia momentum of the cantilever. The general solution for the nth mode profile is the well-known equation

$$U_n(x) = C[(\cos(k_n \cdot x) - \cosh(k_n \cdot x))] + G[(\sin(k_n \cdot x) - \sinh(k_n \cdot x))] \tag{4}$$

where the nth mode vector k_n is linked with the nth mode resonant frequency by the relation $k_n^4 = \frac{\rho}{EI}\omega_n^2$. Applying the boundary condition, the relation between coefficients C and G

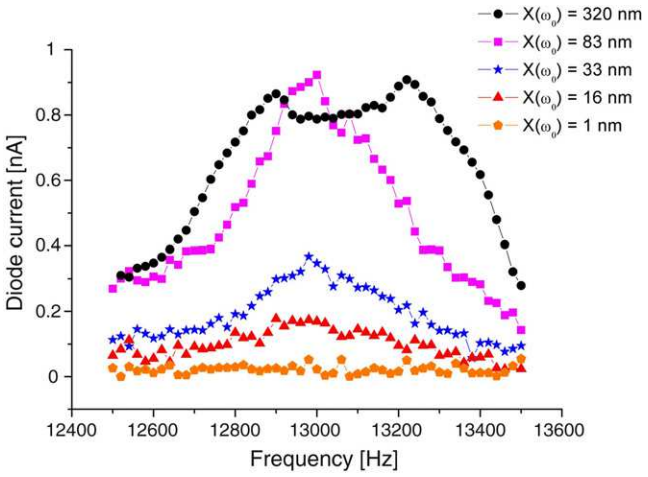

Figure 4. Measured photodiode signal as a function of the lever's excitation frequency. The different curves refer to different excitation amplitudes as specified by the color code.

is found to be

$$\frac{C}{G} = -\frac{\cos(k_n \cdot L) + \cosh(k_n \cdot L)}{\sin(k_n \cdot L) + \sinh(k_n \cdot L)}. \tag{5}$$

The angular shift $\Delta\Theta(x)$ induced by the lever deformation at a position x on the lever is

$$\Delta\Theta(x) = \arctan\left(\frac{\partial U_0(x)}{\partial x}\right) \tag{6}$$

where $U_0(x)$ is the cantilever first-mode profile. The calculated diffracted flux of photons is then obtained integrating the Bragg peak profile $B(\Theta(x))$ over all the x-ray effective beam spot size:

$$I_{\text{calc}} = \int_0^{L_B} B\left[\Theta_{\text{SP}} + \arctan\left(\frac{\partial U_0(x)}{\partial x}\right)\right] \mathrm{d}x \tag{7}$$

where Θ_{SP} is the set-point angle as defined in figure 2. The origin, that is the zero position, is experimentally for this specific case the clamped part of the lever. L_B is the irradiated portion of the lever, smaller than the full lever length.

The expression $B(\Theta(x))$ used for this calculation leads to the rocking curve for (400) reflection of a perfect silicon single crystal with 2 μm thickness in the kinematic approximation [19, 20]. This theoretical rocking curve is presented in figure 2.

The theoretical estimation of the diffracted signal emitted by the Si lever when it is oscillated can be obtained from equation (7). Considering the periodic motion of the cantilever around the set-point angle, the expected modulation of the diffracted beam is given by

$$\Delta I_{\text{mod}} = \int_0^{L_B} B\left[\Theta_{\text{SP}} + \arctan\left(\frac{\partial U_0(x)}{\partial x}\right)\right] \mathrm{d}x - \int_0^{L_B} B\left[\Theta_{\text{SP}} - \arctan\left(\frac{\partial U_0(x)}{\partial x}\right)\right] \mathrm{d}x. \tag{8}$$

ΔI_{mod} represents the change in intensity between the two extreme positions of the oscillating lever.

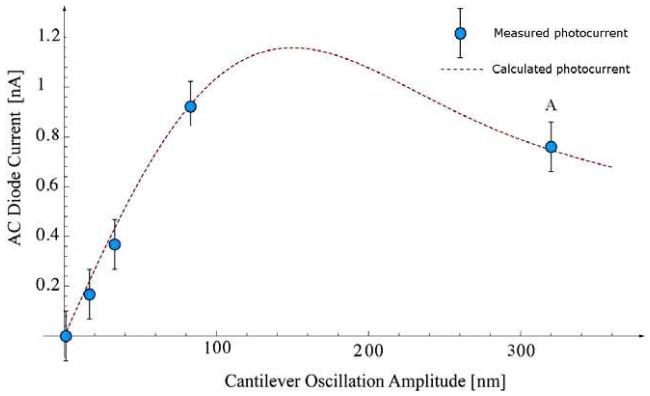

Figure 5. Photodiode signal as a function of different cantilever excitation amplitudes. The continuous curve is from equation (8) (normalized), while the points represent the experimental data with their errors.

In figure 5 we present the photodiode current as a function of the cantilever oscillation amplitude. This photodiode current measures the full amplitude variation of x-ray intensity produced by the oscillating cantilever excited at resonance. This photodiode current is, in fact, the output of the lock-in amplifier that demodulates the instantaneous current variation at the lever resonance frequency.

The mechanical oscillation amplitude is separately measured at the free end through interferometric detection. The blue points represent the photocurrent amplitude measured at the resonant frequency (intersection of the different curves with the green dotted straight line in figure 4); the continuous curve is a normalized theoretical prediction from equation (8).

It is interesting to note the shape of the black curve in figure 4, representing the measured diffracted amplitude for the largest cantilever oscillation amplitude (≈320 nm). This peculiar shape presents two measured symmetric maxima as a function of cantilever oscillation frequency.

This shape is easily explained considering that at resonance the oscillation amplitude reaches the maximum, which, given the functional shape of figure 5, gives indeed a local minimum in the lock-in output.

The functional shape of the curves (experimental and theoretical) in figure 5, reflects the fact that the modulation of the diffracted signal increases when the mechanical oscillation of the AFM cantilever extends from the set-point at the flex (see the definition of flex point in figure 2) to include the maximum of the Bragg peak and beyond. For increasing deflections, however, the *active* footprint actually diffracting the beam is progressively decreasing, leading to the slow decay of the modulated intensity.

In conclusion, we have shown that an x-ray beam can be modulated in intensity by an oscillating AFM lever. The curved shape of the lever has been shown to be a limit for intensity modulation in this set-up. Rigid silicon single-crystal tiles inserted in the MEMS would not present this limitation and would maximize the diffracted intensity. In this experiment the x-ray beam has been chopped at 13 kHz. This moderate operating frequency is related to the resonance frequency of the AFM lever in this proof-of-concept experiment. The resonance frequency can be easily increased to values much higher than 100 kHz by using other types of cantilevers. A specific set-up based on MEMS could certainly be designed so that efficient x-ray choppers could operate at frequencies in the megahertz regime. Considering a simple torsional rigid membrane, an ultrafast burst can be realized. A single-crystal silicon square membrane of $10 \times 10 \times 2\ \mu m^3$ can easily achieve a resonant frequency of several hundred megahertz.

The burst duration is defined as the time that the membrane takes to cover the Bragg peak, which is a time much shorter than the full time for a complete oscillation. If the MEMS system is combined with a multilayer deposition technology, the effective reflectivity can be improved and a Bragg peak hundred times sharper than what have been shown in this paper can be produced. A nanometric MEMS oscillation at the resonant frequency (e.g. 400 MHz as shown for an MEMS in [23]) is then translated into a less than a picosecond burst. Furthermore, as already mentioned, the rigid geometry will remove the efficiency limitation discussed in this paper and the chopped beam will be characterized by a pulse with the same shape of the Bragg peak.

Therefore the combination of MEMS and NEMS technologies with an intense x-ray microbeam can potentially open up a wealth of new experiments based on x-ray examination of time-dependent processes requiring high repetition speed.

References

[1] Larson B C, Tischler J Z and Mills D M 1986 *J. Mater. Res.* **1** 144–54
[2] Chen P, Tomov I V and Rentzepis P M 1996 *J. Chem. Phys.* **104** 10001–7
[3] Rischel C *et al* 1997 *Nature* **390** 490–2
[4] Srajer V *et al* 1996 *Science* **274** 1726–9
[5] Schoenlein R W *et al* 1996 *Science* **274** 236–8
[6] Van Bokhoven J A, Lee T L, Dreakopoulos M, Lamberti C, Thiess S and Zegenhagen J 2008 *Nat. Mater.* **7** 551–5
[7] Cheng L, Fenter P, Bedzyk M J and Sturchio N C 2003 *Phys. Rev. Lett.* **90** 255503–7
[8] Ayanagi H, Kolobov A and Tanaka K 1998 *J. Synchrotron Radiat.* **5** 1001–3
[9] Ingold G, Abela R, Beand P, Johnson S L and Stanb U 2008 *Z. Kristallogr.* **223** 292–306
[10] Plech A, Kataidis V, Istonim K and Wulff M 2007 *J. Synchrotron Radiat.* **14** 288–94
[11] Rentzepis P M and Helliwell J R (ed) 1997 *Time-Resolved Diffraction* (Oxford: Oxford University Press)
[12] Bergsma J P *et al* 1986 *J. Chem. Phys.* **84** 6151–60
[13] Wark J 1996 *Contemp. Phys.* **37** 205–18
[14] Le Grand A D *et al* 1989 *Nucl. Instrum. Methods Phys. Res.* A **275** 442–6
[15] Siria A *et al* 2008 *Nanotechnology* **19** 445501
[16] Cleland A N and Roukes M L 1998 *Nature* **392** 160–2
[17] Rugar D, Budakian R, Mamin H J and Chui W 2004 *Nature* **430** 329–32
[18] Metzger C H and Karrai K 2004 *Nature* **432** 1002–5
[19] Zachariasen W H 1945 *Theory of X-Ray Diffraction in Crystals* (New York: Dover)
[20] Fingerland A 1971 *Acta Crystallogr.* A **27** 280–4
[21] Witmer E A 1991–1992 Elementary Bernoulli–Euler beam theory *MIT Unified Engineering Course Notes* pp 5-114–64
[22] Mendels D A *et al* 2006 *J. Micromech. Microeng.* A **27** 280–4
[23] Bhushan B 2007 *Springer Handbook of Nanotechnology* (Berlin: Springer) pp 424–7

Appendix D

Radiative heat transfer at the nanoscale

nature photonics

LETTERS

PUBLISHED ONLINE: 23 AUGUST 2009 | DOI: 10.1038/NPHOTON.2009.144

Radiative heat transfer at the nanoscale

Emmanuel Rousseau[1‡], Alessandro Siria[2,3‡], Guillaume Jourdan[3], Sebastian Volz[5†], Fabio Comin[4], Joël Chevrier[2] and Jean-Jacques Greffet[1*]

Heat can be exchanged between two surfaces through emission and absorption of thermal radiation. It has been predicted theoretically that for distances smaller than the peak wavelength of the blackbody spectrum, radiative heat transfer can be increased by the contribution of evanescent waves[1–8]. This contribution can be viewed as energy tunnelling through the gap between the surfaces. Although these effects have already been observed[9–14], a detailed quantitative comparison between theory and experiments in the nanometre regime is still lacking. Here, we report an experimental setup that allows measurement of conductance for gaps varying between 30 nm and 2.5 μm. Our measurements pave the way for the design of submicrometre nanoscale heaters that could be used for heat-assisted magnetic recording or heat-assisted lithography.

In the late 1960s, an anomalous radiative heat transfer between flat metallic surfaces was reported by Domoto at cryogenic temperatures[15] and by Hargreaves at room temperature[9]. In both cases, an increase of the flux was measured for separation gaps in the micrometre range. A theoretical explanation was given by Polder and Van Hove[1] in the framework of stochastic electrodynamics introduced by Rytov[2] a few years previously. Further theoretical studies are summarized in two recent reviews[5,7]. The theory accounts for both quantum and thermodynamic fluctuations and has been successfully applied to model Casimir forces[16]. Although quantum fluctuations yield a force that agrees quantitatively with theory, thermodynamic fluctuations are difficult to observe when measuring forces[17–19]. Instead, heat transfer is only due to thermodynamic fluctuations. The first attempt to quantitatively detect heat transfer for submicrometre gaps was reported by Xu and colleagues[20], but was inconclusive. More recently, the Oldenburg group[10,11] has demonstrated unambiguously a heat transfer that increases as the distance decreases in the submicrometre range. They studied heat transfer between a gold-coated scanning tunnelling microscope and a plate of gold or GaN. Unfortunately, the geometry of the experiment was too complex to allow a quantitative comparison with theory. It was predicted that heat transfer between dielectric surfaces is more efficient because of surface-phonon polariton contributions[21]. The first measurements between two dielectric materials were reported by the MIT group[13,14]. They measured heat transfer between a sphere and a plate, both made of silica, over a range of 30 nm and 10 μm. The comparison of these results with theoretical calculations based either on the Derjaguin approximation[22] or on sphere–sphere geometry[23] led these authors to the conclusion that the Derjaguin approximation is not valid for near-field radiative heat transfer.

To avoid parallelism difficulties in the plane–plane geometry, we used a sphere–plane geometry, as for recent Casimir force measurements[17–19,24] and near-field heat transfer experiments[13,14]. The distance-dependent thermal conductance is given by $G(d,T) = \varphi(d)/\Delta T$, where $\varphi(d)$ is the thermal flux through the gap d and ΔT is the temperature difference between the sphere and the plate. The plate was heated to produce a temperature difference ΔT between the sphere and the plate, typically on the order of 10–20 K. Although the radiative resistance of the gap decreased significantly in the near field, it remained much larger than all the other thermal resistances at all distances explored (30 nm–2.5 μm). Thus, the temperature difference across the gap could be considered to be constant as distance varied (quantitative details are given in the Supplementary Information). The temperatures were measured with a type-K thermocouple. The near-field radiative heat flux was of the order of nanowatts, so conduction through air had to be suppressed by working in a vacuum (10^{-6} mbar). It was also necessary to use a very sensitive fluxmeter. Following the procedure in ref. 13, we glued the sphere onto a bimorph cantilever based on an atomic force microscope cantilever as proposed by Barnes and colleagues[25,26]. Such fluxmeters can measure fluxes variations in the order of tens of picowatts. We used commercially available cantilevers from Veeco (length = 320 μm, width = 22 μm, thickness = 0.6 μm) made of silicon nitride (thickness 525 nm) with a gold layer (60 nm) deposited on a chromium layer (15 nm). The cantilever bending was measured using a fibre interferometric technique (Fig. 1). A drawback of using an optical readout is that part of the optical beam is absorbed and introduces a spurious flux term. It is therefore fundamental to keep it constant during measurement. A feedback loop keeps the distance between the cantilever and the optical fibre constant. In addition, a thermally stabilized laser is used to reduce the absorption fluctuations by the fluxmeter. The cantilever is perpendicular to the plane (Fig. 1) to avoid bending due to electrostatic or Casimir forces. The displacements carried out with the piezoelectric stages from Attocube were calibrated using an interferometric method. The z-displacement steps were 7 nm.

The raw data were gathered by measuring the bending δ of the cantilever in relation to the sphere–plate distance. From Barnes and colleagues[25,26], the bimorph deformation δ is assumed proportional to the flux. H is denoted as the proportionality factor. Cantilever bending was detected using the feedback voltage applied to the optical-fibre actuator in constant-distance mode. The contact between the plate and the sphere defined the zero of the z-axis. Note that for distances larger than 10 μm, the thermal conductance tends to its far-field value $G_{\mathrm{ff}} = 2\pi R^2 4\sigma\varepsilon(T)T^3$, where R is the sphere radius, σ the Stefan constant and $\varepsilon(T) = 0.354$ is the silica emissivity evaluated using optical data from ref. 27. We found G_{ff} to be equal to 5.45 nW K^{-1}. The proportionality

[1]Laboratoire Charles Fabry, Institut d Optique, CNRS, Univ Paris-sud, Campus Polytechnique, RD 128, 91127 Palaiseau, France, [2]Institut Néel – CNRS and Université Joseph Fourier, 38042 Grenoble, France, [3]CEA/LETI MINATEC/DIHS/LCMS, 17 rue des Martyrs, 38054 Grenoble cedex 9, France, [4]ESRF, 6 rue Horowitz 38042 Grenoble Cedex, France, [5]Laboratoire EM2C-CNRS UPR 288, École Centrale Paris, Grande voie des vignes 92295 Châtenay-Malabry France; †Present address: LIMMS, UMI CNRS 2820-IIS, Center for International Research on MicroMechatronics, CIRMM, Institute of Industrial Science, University of Tokyo, 4-6-1 Komaba, Meguro-ku, Tokyo 153-8505, Japan; ‡These authors contributed equally to this work.
*e-mail: jean-jacques.greffet@institutoptique.fr

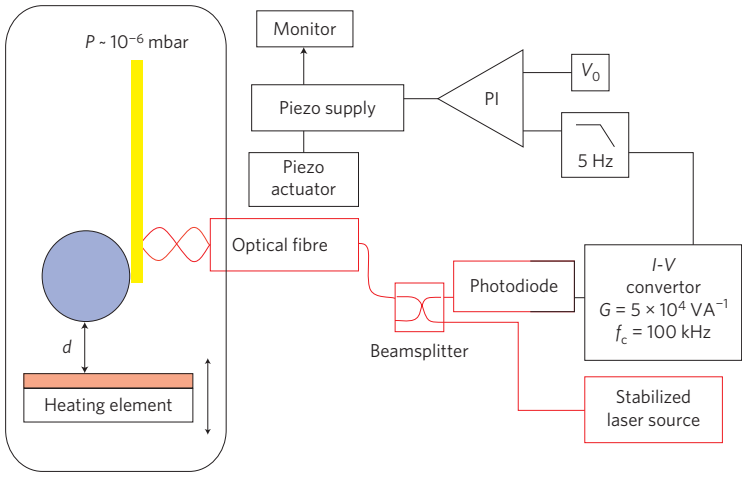

Figure 1 | Experimental setup. (Red lines are used for the optical part and black lines for the electrical part of the setup.) Reflection of the laser beam on the cantilever produces an interference pattern. A feedback loop keeps the bimorph–optical fibre distance constant by applying a voltage to a piezoelectric actuator holding the optical fibre. The feedback loop and the thermally stabilized laser maintain spurious heating from the laser constant, and ensure that flux variations are only due to the conductance variations as the separation d is changed, with constant temperature difference ΔT between the sphere and the plate. The plate is heated and mounted on a piezoelectric actuator. The measured signal is the voltage applied to the fibre-actuator supply.

factor can be measured independently. We found H to be 2.30 nW nm^{-1}, with an accuracy of 2%. The conductance is the sum of the far-field contribution $G_{\rm ff}$ and the near-field contribution $H\delta(d)/\Delta T$

$$G_{\rm exp}(d) = G_{\rm ff} + \frac{H}{\Delta T}\delta(d) \qquad (1)$$

The theoretical model of the near-field heat transfer is now discussed. The flux between the sphere and the plate is locally described as a flux between two parallel plates separated by a distance d using the heat transfer coefficient $h(d,T)$ derived numerically[7,21]. This is known as the Derjaguin approximation[22] (Fig. 2a). We integrate over the whole area to obtain the theoretical conductance:

$$G_{\rm theo}(d,T) = \int_0^R h[\tilde{d}(r),T]2\pi r\,{\rm d}r \qquad (2)$$

where R is the radius of the sphere and $\tilde{d}(r) = d + R - \sqrt{R^2 - r^2}$ is the local distance between the plane and the sphere surface (Fig. 2a). For two infinite planes and for distances smaller than $d = 500$ nm, the flux increases as $1/d^2$ in the short distance regime. If we retain only this asymptotic near-field contribution and neglect the other contributions to $h(d,T)$, integration over the sphere surface yields a $1/d$ behaviour for the conductance. This approximation has been used in refs 13 and 14. It is also the standard approach for computing the Casimir force[17–19,24] owing to its rapid decay ($1/d^4$) with distance. Here, we show that it is necessary to include all contributions when dealing with radiative heat transfer. The theoretical conductance versus the sphere–plate distance is displayed in Fig. 2b. It is clearly seen that the conductance strongly deviates from the $1/d$ law for distances larger than 10 nm. Finally, note that this approach does not account for Mie resonances of the sphere. This is an excellent approximation, because in the domain where heat transfer is large, the medium is lossy, so coherence length[28] along the surface and the decay length in the medium are much smaller than the sphere radius. For wavelengths corresponding to silica resonances[27] (21 μm and 9 μm), coherence and decay lengths are smaller than 1 μm.

The data can now be compared with the model. Although the distance d is calibrated and the zero is given by the contact, we

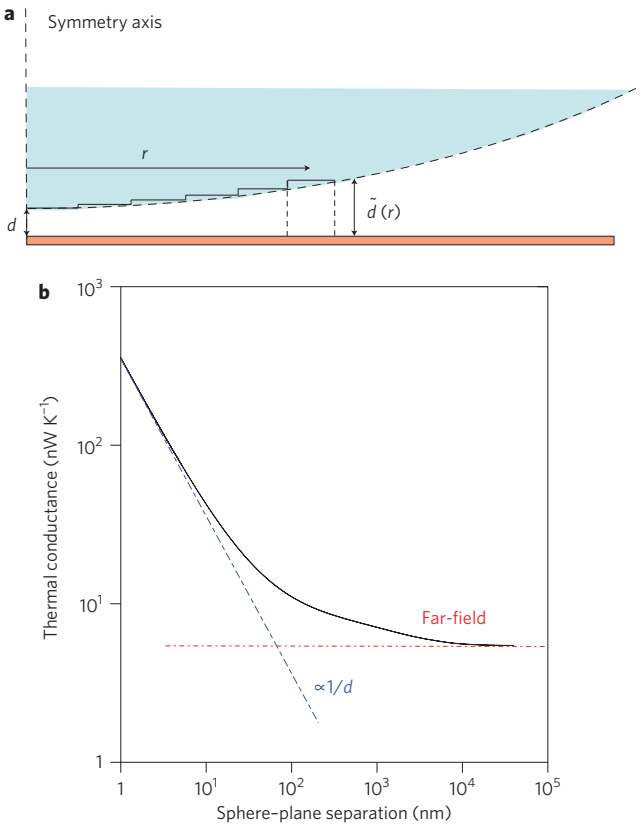

Figure 2 | The Derjaguin approximation. a, The flux between the sphere and the plane is obtained by integrating the local contributions using the heat transfer coefficient $h(d,T)$ for two parallel planes. **b**, Theoretical thermal conductance between a silica sphere with radius $R = 20$ μm and a silica plane using the Derjaguin approximation. A $1/d$ regime, characteristic of the near-field contribution, is observed for distances smaller than 10 nm. The conductance tends to the far-field constant value for distances larger than 10 μm. Although the sphere is made on sodalime glass and the plate on borosilicate glass, we assume that optical properties for both materials are close to the optical properties of amorphous silica. Both materials contain more than 70% silica. Optical data for silica are taken from ref. 27.

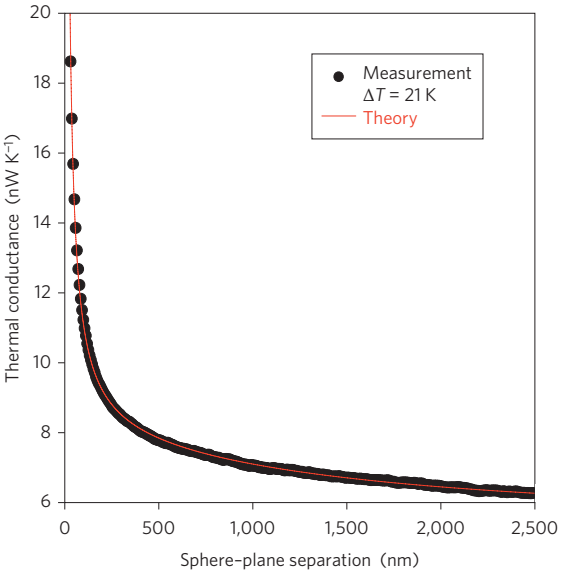

Figure 3 | Thermal conductance between the sphere with diameter 40 μm and the plate as a function of gap distance. The black dots represent experimental data and the red line the theoretical model. The temperature difference between the plate and the sphere is 21 K. The distance shift used in the comparison is $b = 31.8$ nm and the cantilever response coefficient used in the comparison is $H = 2.162$ nW nm^{-1}.

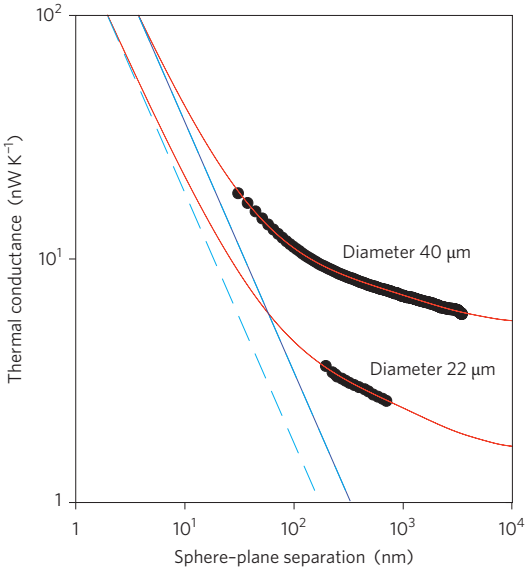

Figure 4 | Thermal conductance between the sphere and the plate as a function of the gap for two sphere diameters (40 and 22 μm). The black dots represent experimental data and the red line is the theoretical model. The dashed blue line is the asymptotic contribution varying as $1/d$. This contribution is dominant for gaps smaller than 10 nm. For the 22-μm-diameter sphere, the smallest separation is 150 nm owing to roughness.

have found that the experimental data for different approach curves are shifted. A microscope image of the sphere shows a characteristic roughness of ~40 nm, which is consistent with the shifts observed between different curves. To account for this roughness, we introduce a shift b when comparing the experimental data of each approach curve with the theoretical conductance:

$$G_{\mathrm{theo}}(d+b,T) = G_{\mathrm{ff}} + H\delta(d)/\Delta T \qquad (3)$$

Figure 3 shows a comparison of the data with the model for a particular approach curve. Because the noise on the cantilever bending measurements was below 0.1 nm, we prefer to consider H as a fitting parameter so that the calculated curve shape and the one given by experimental data can be best compared. The scaling factor found following this method is $H = 2.162 \pm 0.005$ nW nm^{-1}. This value is consistent with the calibration value $H = 2.30$ nW nm^{-1} found for another cantilever of the same batch but with different exact dimensions. Indeed, the cantilever length dispersion is 10%, yielding an H dispersion of 30%.

It is seen in Fig. 3 that the sphere–plane conductance increases from 6 to 18 nW K^{-1} in the range 30 nm to 2.5 μm. In this range, the coefficient $h(d,T)$ increases by a factor of 407 from 7.22 to 2,938 W m^{-2} K^{-1}. We emphasize that the theory reproduces correctly the non-trivial transition between the far- and near-field regime in the range 30 nm to 2.5 μm. The agreement between the theoretical conductance and the data shows that the Derjaguin approximation is valid, in contrast with the conclusions of refs 13 and 14. As a further check of the theory, we made measurements with a sphere of different radius. Figure 4 presents the data in logarithmic scales for two spheres of diameters 40 and 22 μm. It is seen that the curves are different, indicating a non-trivial dependence of the conductance on the sphere radius. The red line is the result of the numerical integral using the Derjaguin approximation. The dashed blue curve is the $1/d$ asymptotic dependence for the sphere–plane geometry.

In summary, we have reported experimental measurements of the radiative conductance in the near-field regime. We found that the data agree with the theory in the range 2.5 μm to 30 nm. This agreement with theory confirms that radiative heat transfer can be significantly enhanced at distances in the nanometre regime. Our results strongly support previous theoretical works and pave the way to engineering radiative heat transfer in the mesoscopic regime. Possible applications include nano-electro-mechanical systems, heat-assisted magnetic recording[29] or heat-assisted lithography. Further aspects of radiative heat transfer at the nanoscale remain to be explored. For example, it has been predicted that the flux can be quasi-monochromatic[21,30] and strongly depends on the matching between the optical properties of both materials. The understanding of the role of non-local effects at distances smaller than 10 nm is also a subject under examination in the literature[8,10,31], so further experiments are needed in this field.

Received 13 May 2009; accepted 25 July 2009;
published online 23 August 2009

References

1. Polder, D. & Van Hove, M. Theory of radiative heat transfer between closely spaced bodies. *Phys. Rev. B* **4,** 3303–3314 (1971).
2. Rytov, S. M., Kratsov, Yu. A. & Tatarskii, V. I. *Principles of Statistical Radiophysics* **3,** Ch. 3 (Springer-Verlag, 1987).
3. Loomis J. J. & Maris, H. J. Theory of heat transfer by evanescent electromagnetic waves. *Phys. Rev. B* **50,** 18517–18524 (1994).
4. Pendry, J. B. Radiative exchange of heat between nanostructures. *J. Phys.: Condens. Matter* **11,** 6621–6633 (1999).
5. Volokitin, A. I. & Persson, B. N. J. Near-field radiative heat transfer and noncontact friction. *Rev. Mod. Phys.* **79,** 1291–1329 (2007).
6. Dorofeyev, I. A. Rate of energy dissipation of the thermal fluctuation field of the sample at the tip of a tunneling microscope. *Tech. Phys. Lett.* **23,** 109–111 (1997).
7. Joulain, K., Mulet, J.-P., Marquier, F., Carminati, R. & Greffet, J.-J. Surface electromagnetic waves thermally excited: radiative heat transfer, coherence properties and Casimir forces revisited in the near field. *Surf. Sci. Rep.* **57,** 59–112 (2005).
8. Biehs, S. A. Thermal heat radiation, near-field energy density and near-field radiative heat transfer of coated materials. *Eur. Phys. J. B* **58,** 423–431 (2007).
9. Hargreaves, C. M. Anomalous radiative transfer between closely-spaced bodies. *Phys. Lett. A* **30,** 491–492 (1969).
10. Kittel, A. *et al.* Near-field heat transfer in a scanning thermal microscope. *Phys. Rev. Lett.* **95,** 224301 (2005).

11. Wischnath, U. F., Welker, J., Munzel, M. & Kittel, A. The near-field scanning thermal microscope. *Rev. Sci. Instrum.* **79,** 073708 (2008).
12. DiMatteo, R. S. *et al.* Enhanced photogeneration of carriers in a semiconductor via coupling across a nonisothermal nanoscale vacuum gap. *Appl. Phys. Lett.* **79,** 1894–1896 (2001).
13. Narayanaswamy, A. & Chen, G. Near-field radiative heat transfer between a sphere and a substrate. *Phys. Rev. B* **78,** 115303 (2008).
14. Shen, S., Narayanaswamy, A. & Chen, G. Surface phonon polaritons mediated energy transfer between nanoscale gaps. *Nano Lett.* doi: 10.1021/nl901208v (2009).
15. Domoto, G. A., Boehm, R. F. & Tien, C. L. Experimental investigation of radiative transfer between metallic surfaces at cryogenic temperatures. *J. Heat Transfer* **92,** 412 (1970).
16. Lifshitz, E. M. The theory of molecular attractive forces between solids. *Zh. Eksp. Teor. Fiz.* **29,** 94–110 (1955) [*Sov. Phys. JETP* **2,** 73 (1956)].
17. Jourdan, G., Lambrecht, A., Comin, F. & Chevrier, J. Quantitative non-contact dynamic Casimir force measurements. *J. Eur. Phys. Lett.* **85,** 31001 (2009).
18. Mohideen, U. & Roy, A. Precision measurement of the Casimir force from 0.1 to 0.9 μm. *Phys. Rev. Lett.* **81,** 4549–4552 (1998).
19. Lamoreaux, S. K. Demonstration of the Casimir force in the 0.6 to 6 μm range. *Phys. Rev. Lett.* **78,** 5–8 (1997).
20. Xu, J. B., Luger, K., Moller, R., Dransfeld, K. & Wilson, I. H. Heat transfer between two metallic surfaces at small distances. *J. Appl. Phys.* **76,** 7209–7216 (1994).
21. Mulet, J. P., Joulain, K., Carminati, R. & Greffet, J. J. Enhanced radiative heat transfer at nanometric distances. *Microscale Thermophys. Eng.* **6,** 209–222 (2002).
22. Derjaguin, B. V., Abrikosova, I. I. & Lifshitz, E. M. Direct measurement of molecular attraction between solids separated by a narrow gap. *Quart. Rev. Chem. Soc.* **10,** 295–329 (1956).
23. Narayanaswamy, A. & Chen, G. Thermal near-field radiative transfer between two spheres. *Phys. Rev. B* **77,** 075125 (2008).
24. Jourdan, G. Vers un microscope de force de Casimir. PhD thesis, Université Joseph Fourier (2007).
25. Lai, J., Perazzo, T., Shi, Z. & Majumdar, A. Optimization and performance of high-resolution micro-optomechanical thermal sensors. *Sens. Actuat A* **58,** 113–119 (1997).
26. Barnes, J. R. *et al.* A femtojoule calorimeter using micromechanical sensors. *Rev. Sci. Instrum.* **65,** 3793–3796 (1994); Erratum: *Rev. Sci. Instrum.* **66,** 3083 (1994).
27. Palik, E. D. *Handbook of Optical Constants of Solids* Vol. 1, 749 (Academic Press, 1985).
28. Henkel, C., Joulain, K., Carminati, R. & Greffet, J. J. Spatial coherence of thermal near fields. *Opt. Commun.* **186,** 57–67 (2000).
29. Challener, W. A. *et al.* Heat-assisted magnetic recording by a near-field transducer with efficient optical energy transfer. *Nature Photon.* **3,** 220–224 (2009).
30. Mulet, J. P., Joulain, K., Carminati, R. & Greffet, J. J. Nanoscale radiative heat transfer between a small particle and a plane surface. *Appl. Phys. Lett.* **78,** 2931–2933 (2001).
31. Chapuis, P. O., Volz, S., Henkel, C., Joulain, K. & Greffet, J. J. Effects of spatial dispersion in near-field radiative heat transfer between two parallel metallic surfaces. *Phys. Rev. B* **77,** 035431 (2008).

Acknowledgements

The authors acknowledge the support of Agence Nationale de la Recherche through Monaco projects and Léti-Carnot Institute. J.-J.G. and E.R. thank P.O. Chapuis for fruitful discussions. J.C. and A.S. thank S. Huant for support and fruitful discussions.

Additional information

Supplementary information accompanies this paper at www.nature.com/naturephotonics. Reprints and permission information is available online at http://npg.nature.com/reprintsandpermissions/. Correspondence and requests for materials should be addressed to J.-J.G.

nature photonics

SUPPLEMENTARY INFORMATION

DOI: 10.1038/NPHOTON.2009.144

Supplementary materials :

Flux and Thermal conductance for three temperature differences :

For the sphere with radius 40 µm, we plot in Fig S1-a the flux variation when decreasing the distance between the sphere and the plate for three different temperatures. We plot in Fig S1-b the thermal conductance for the three temperature differences derived from a fit of H and b using eq. (3). The coefficient H used for the three curves has the same value as the same cantilever is used. It is seen that the three measurements yield the same conductance.

Roughness of the sphere:

In the comparison between the data and the theory, we have included a shift. FigS2a illustrates the definition of the parameter b. Fig. S2 b is a scanning electron microscope view of the 22 µm sphere. The roughness of the sphere is seen. These images allows to estimate the roughness of the spheres. We found 150 nm for the 22 µm sphere and 40 nm for the 40 µm sphere. This is consistent with the values found when fitting the experimental data.

Comparison of thermal resistances.

In this section, we analyse the thermal resistances on the experimental setup. The key conclusion is that the thermal resistance of the gap is always the larger resistance so that the temperature difference across the gap does not vary when the gap is reduced. First of all, we can assume the system to be in steady state. Indeed, the sphere becomes isothermal in a typical time 0.5 ms and the bimorph becomes isothermal in a typical time of 2 ms whereas all other time constants in the experiment are larger than 100 ms. We can now use an electrical analogy with thermal resistances. The thermal circuit is sketched in Fig. S3. It is composed of several resistances in series connecting the hot plate at T_p to the end of the bimorph at the ambient temperature at T_a.

The average thermal conductivity of the cantilever is λ=60 W/(m.K) leading to a thermal resistance $R_c=L/\lambda tw = 0.4\ 10^6$ *K/W. (L=320 µm, t=0.6 µm, w=22 µm).* The sphere thermal conductance is close to

DOI: 10.1038/NPHOTON.2009.144

$R_s=1/(\lambda R)=40\ 10^3\ K/W$ where R is the sphere radius. We approximate the glue by a cylinder with length smaller than one micron and radius larger than one micron. Its thermal conductivity is λ=1.6 W/(m.K) leading to a thermal resistance smaller than $R_g=L/\lambda tw = 0.6\ 10^6\ K/W$. This calculation clearly overestimates the thermal resistance of the glue.

The thermal conductance varies from 6 nW/K in the far-field to 18 nW/K at 50 nanometers. So thermal resistance vary from $R_r=160\ 10^6\ K/W$ in the far-field to $R_r=53\ 10^6\ K/W$ at 50 nanometers. Despite the near-field increase, the gap resistance remains the largest resistance. It is at least two orders of magnitude larger than other thermal resistances in the circuit. It follows that the temperature of the sphere is equal to the ambiant temperature within the accuracy of the thermocouples.

$$T_{sd} - T_p = \frac{R_r}{R_r + R_s + R_g + R_c}(T_a - T_p)$$

Cantilever calibration

In order to calibrate the cantilever response, we have used the same experimental setup working in the far-field regime. The gap between the plate and the sphere was approximatively 50 μm. We measured the cantilever bending when increasing the temperature of the hot plate. The temperatures of the plate and the bimorph were measured with a type-K thermocouple. The far-field flux was found from: $\varphi = 8\pi\sigma\varepsilon(T)R^2T^3\Delta T$ where σ is the Stefan-Boltzmann constant, R the sphere radius, $T=300K$ the mean temperature, $\varepsilon(T)=0.354$ the mean emissivity derived from the exact calculation between two infinite planes. ΔT is the temperature difference between the sphere and the plate. The conversion factor H can be extracted from the slope of the curve FIG S4. It is found to be H=2.30 ±0.05 nW/nm. The total uncertainty on H is estimated to be 10% due to uncertainties on the temperature T and the total emissivity $\varepsilon(T)$. The former is measured using a type-K thermocouple, the latter is estimated from $h_{ff}/4\sigma T^3$ where σ is the Stefan-Boltzmann constant, T the room temperature and h_{ff} is the far-field value of the heat transfer coefficient between two infinite planes computed using optical properties of glass from ref 27. The proportionality factor value depends on each cantilever. The cantilever used for the data presented in Fig.

3 has not been calibrated. $H/\Delta T$ was obtained by fitting the data according to equation (3). Using ΔT=10,17,21 K, we found H=2.17; 2.16; 2.14. The dispersion on these values is consistent with the thermocouple accuracy.

Supplementary figure caption :

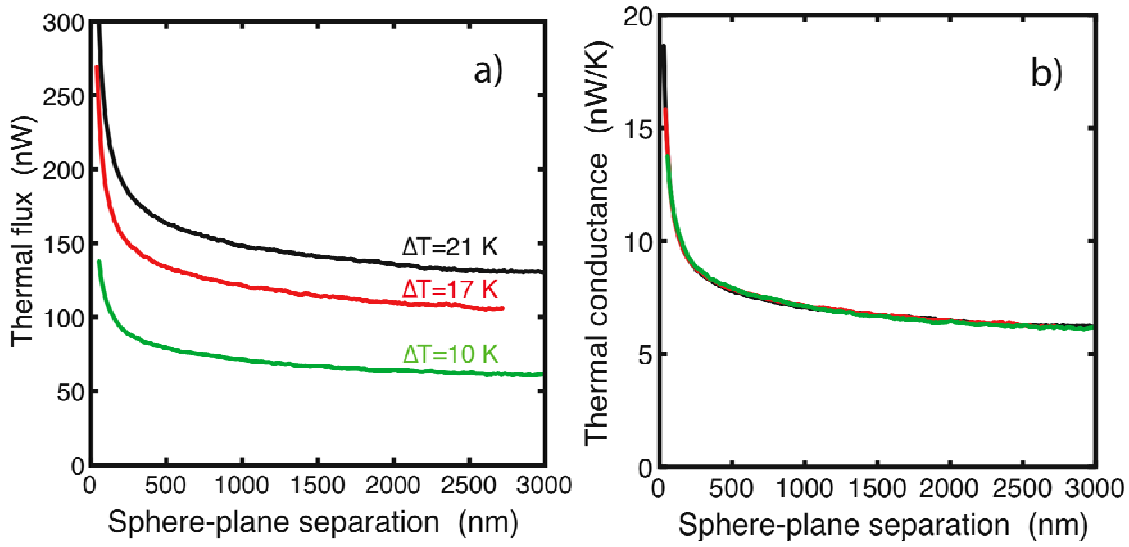

FIG.S1: a) : **Flux versus distance for three temperature differences**. The sphere diameter is 40 μm. **b)**: **Thermal conductance derived using eq (3) from three different sets of measurements**. The same value of H was used for the three curves.

DOI: 10.1038/NPHOTON.2009.144

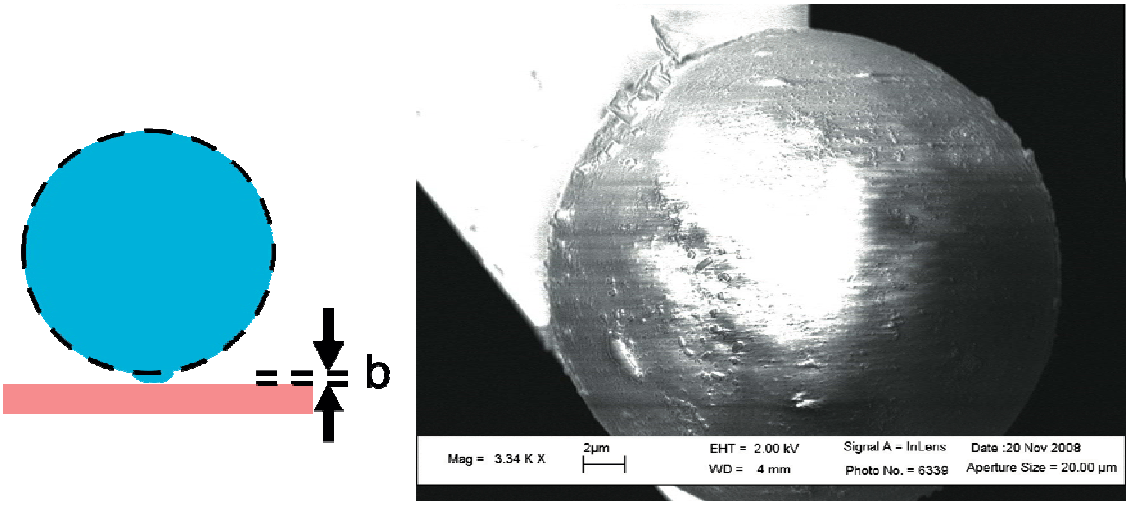

a) b)

FIG.S2: a) Definition of the fitting parameter b.

b) : **SEM picture of the sphere**. The sphere diameter is 22 μm.The roughness is typically 150 nm for the 20 μm (diameter) sphere and 50 nm for the 40 μm (diameter) sphere.

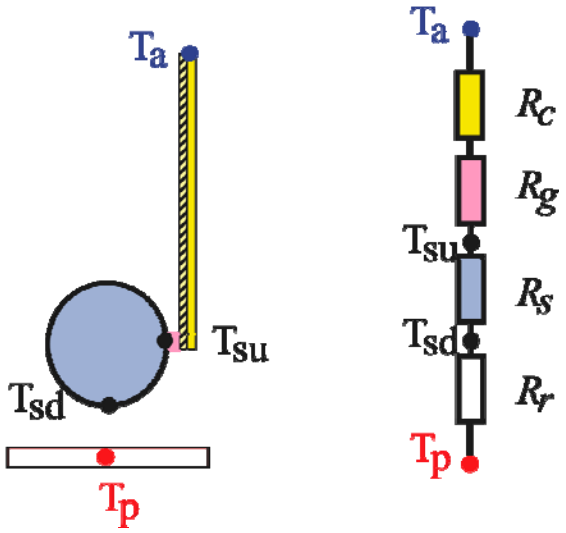

FIG.S3 : **Thermal equivalent circuit of the experiment**. T_p is the hot plate temperature. The end of the bimorph is at the ambient temperature T_a. T_{sd} denote the temperature of the sphere surface. R_r denotes the radiative thermal resistance of the gap, R_s the sphere thermal resistance, R_g the thermal resistance of the glue and R_c the cantilever thermal resistance.

DOI: 10.1038/NPHOTON.2009.144

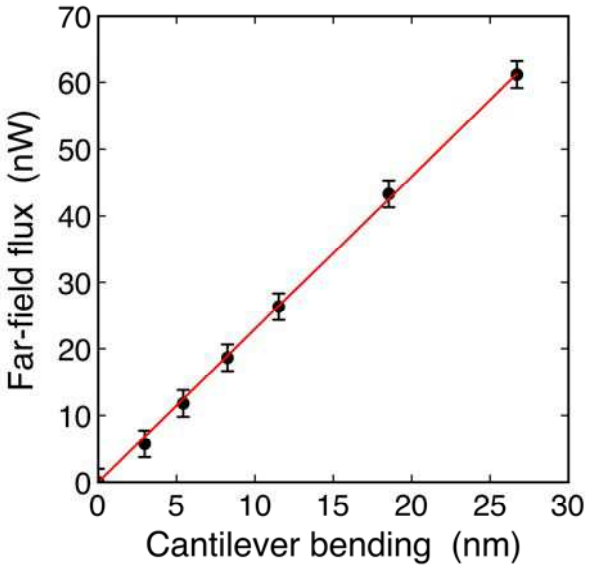

FIG.S4 : **Fluxmeter calibration**. This figure presents the cantilever bending versus the thermal flux when the sphere is in the far-field regime. The distance between the sphere and the plate is around 50 μm. The conversion factor H is extracted from the slope of the fit. Its value is 2.30 ±0.05 nW/nm. The bars in this curve are due to the thermocouple reader precision.

Bibliography

[1] D. Rugar, R. Budakian, H. J. Mamin and W. Chui, *Nature* **430**, 329-332 (2004)

[2] H. J. Mamin and D. Rugar, Appl. Phys. Lett. **79**, 3358 (2001)

[3] Y. T. Yang, C. Callegari, X. L. Feng, K. L. Ekinci, and M. L. Roukes, Nano Lett. **6**, 583 (2006)

[4] M. Li, H. X. Tang and M. L. Roukes, *Nature Nanotechnology* **2**, 114-120 (2007)

[5] A. N. Cleland and M. L. Roukes, *Nature* **392**, 160-162 (1998)

[6] T. P. Burg, M. Godin, S. M. Knudsen, W. Shen, G. Carlson, J. S. Foster, K. Babcock and S. M. Manalis, *Nature* **446**, 1066-1069 (2007)

[7] S. S. Verbridge, J.M. Parpia, R. B. Reichenbach, L. M. bellan and H. G. Craighead, *J. Appl. Phys* **99**, 124304 (2006)

[8] B. M. Zwickl *et al.*, *arXiv:0711.2263v1* (2007)

[9] Torricelli, G. *Caractrisation des Interactions entre une Microsphre et une Surface Mtalliques aux Echelles Nanomtriques*, Ph.D. Thesis, 2005

[10] Jourdan, G. *Vers un microscope a force de Casimir*, Ph.D. Thesis, 2007

[11] Jourdan, G., Lambrecht, A., Comin, F., Chevrier. *Eur. Phys. Lett.* **85**, 31001 (2009)

[12] Mohideen, U., Roy A. *Phys. Rev. Lett.* **81**, 4549-4552 (1998).

[13] Lamoreaux, S.K. *Phy. Rev. Lett.* **78**, 5-8 (1997)

[14] C.H. Metzger and K. Karrai, Nature (London) **432**, 1002 (2004)

[15] S. Gigan, H.R. Boehm, M. Paternostro, F. Blaser, G. Langer, J.B. Hertzberg, K.C. Schwab, D. Bauerle, M. Aspelmeyer, and A. Zeilinger, Nature (London) **444**, 67 (2006)

[16] O. Arcizet, P.-F. Cohadon, T. Briant, M. Pinard, A. Heidmann, Nature (London) **444**, 71 (2006)

[17] D. Kleckner and D. Bouwmeester, Nature (London) **444**, 75 (2006).

[18] C. Metzger, M. Ludwig, C. Neuenhahn, A. Ortlieb, I. Favero, K. Karrai, and F. Marquardt, Phys. Rev. Lett. **101** 133903 (2008)

[19] G. Jourdan, F. Comin, and J. Chevrier, Phys. Rev. Lett. **101** 133904 (2008)

[20] O. Arcizet, P.-F. Cohadon, T. Briant, M. Pinard and A. Heidmann, *Nature* **444**, 71-74 (2006)

[21] B.V. Derjaguin, I.I. Abrikosova, and E.M. Lifshitz, Q. Rev. Chem. Soc. **10**, 295 (1956)

[22] Mo Li, H.X. Tang, and M.L. Roukes, Nature Nanotech. **2**, 114 (2007)

[23] C. Cottin-Bizonne, B. Cross, A. Steinberger, and E. Charlaix, Phys. Rev. Lett. **94**, 056102 (2005)

[24] W.Y. Shih, X. Li, H. Gu, W.-H. Shih, and I.A. Aksay, J. Appl. Phys. **89**, 1497 (2001)

[25] P. K. Hansma, J. P. Cleveland, M. Radmacher, D. A. Walters, P. E. Hillner, M. Bezanilla, M. Fritz, D. Vie, H. G. Hansma, C. B. Prater, J. Massie, L. Fukunaga, J. Gurley, and V. Elings, Appl. Phys. Lett. **64**, 1738 (1994)

[26] A. Maali, T. Cohen-Bouhacina, G. Couturuer, and J.-P. Aimé, Phys. Rev. Lett. **96**, 086105 (2006)

[27] A. Raman, J. Melcher, and R. Tung, Nanotoday **3**, 20 (2008)

[28] D.J. Muller, Biochemistry **47**, 7986 (2008)

[29] J.N. Munday and F. Capasso, Phys. Rev. A **75**, 060102 (2007)

[30] J.N. Munday, F. Capasso, A. Parsegian, and S.M. Bezrukov, Phys. Rev. A **78**, 032109 (2008)

[31] J.N. Munday, F. Capasso, and A. Parsegian, Nature (London) 457, 170 (2009)

[32] L. Bellon, J. Appl. Phys. **104**, 104906 (2008)

[33] R.B. Bhiladvala and Z.J. Wang, Phys. Rev. E **69**, 036307 (2004)

[34] C.P. Green and J.E. Sader, J. Appl. Phys. **98**, 114913 (2005)

[35] T. Naik, E.K. Longmire, and S.C. Mantell, Sensor and Actuators A: Physical **102**, 240 (2003)

[36] M.R. Paul and M.C. Cross, Phys. Rev. Lett. **92**, 235501 (2004)

[37] J. Dorignac, A. Kalinowski, S. Erramilli, and P. Mohanty, Phys. Rev. Lett. **96**, 186105 (2006)

[38] S. Basak, A. Raman, and S.V. Garimella, J. Appl. Phys. **99**, 114906 (2006)

[39] R.C. Tung, A. Jana, and A. Raman, J. Appl. Phys. **104**, 114905 (2008)

[40] D. Y. C. Chan and R. G. Horn, J. Chem. Phys. **83**, 5311 (1985)

[41] O. I. Vinogradova, Langmuir **11**, 2213 (1995)

[42] Witmer E. A., Elementary Bernoulli-Euler Beam Theory, MIT Unified Engineering Course Notes: pp. 5-114 to 5-164 (1991-1992).

[43] Mendels D. A, *et al.*, *J. micromech. microeng.* **A27**, 280-284 (2006)

[44] P. Tabeling, *Introduction to microfluidics* (Oxford University Press), USA, 2006

[45] Larson B. C., Tischler J. Z. and Mills D. M. *J. Mater. Res.* **1**, 144-154 (1986).

[46] Chen P., Tomov I. V. and Rentzepis P. M., *J. Chem. Phys.* **104** , 10001-10007 (1996).

[47] Rischel C. Uschmann I., Albouy P. A., Geindre J. P., Audebert P., Gauthier J. C., Fröster E., Mrtin J. L., Antonetti A., Rousse A., *Nature* **390**, 490-492 (1997).

[48] Srajer V., Teng T., Ursby T., Pradervand C. Ren Z., Adachi S., Schildkamp W., Bourgeois D., Wulff M., Moffat K., *Science* **274**, 1726-1729 (1996).

[49] Schoenlein R. W., Leemans W. P., Chin A. H., Volfbeyn P., Glover T. E., Balling P., Zolotorev M., Jim K.J., Chattopadhyay S., Shank V., *Science* **274**, 236-238 (1996).

[50] Van Bokhoven J. A., Lee T. L., Dreakopoulos M., Lamberti C., Thiess S. and Zegenhagen J. *Nature Mat.* **7**, 551-555 (2008)

[51] Cheng L., Fenter P., Bedzyk M. J.and Sturchio N. C. *Phys. Rev. Lett.* **90**, 255503-255507 (2003).

[52] Ayanagi H., Kolobov A. and Tanaka K., *J. Synchrotron Rad.* **5**, 1001-1003 (1998).

[53] Ingold G., Abela R., Beand P., Johnson S. L. and Stanb U., *Z. Kristallogr.* **223**, 292-306 (2008).

[54] Plech A. Kataidis V., Istonim K. and Wulff M. *J. Synchrotron Rad.* **14**, 288-294 (2007).

[55] Rentzepis P. M. and Helliwell J. R. (eds) Time-Resolved Diffraction (Oxford Univ. Press, (1997).

[56] Bergsma J. P., Coladonato M. H., Edelsten P. M., Kahn J. D., Wilson K. R., Fredkin D. R., *J. Chem. Phys* **84**, 6151-6160 (1986).

[57] Wark J., *Contemp. Phys.* **37**, 205-218 (1996).

[58] Le Grand A. D. *et al.*, *Nuclear Instruments and Methods in Physics Research A* **275** 442-446 (1989).

[59] A. Snigirev, V. Kohn, I. Snigireva and B. Lengerer, *Nature* **384**, 49-51 (1996)

[60] M. O. Krause, *J. Phys. Chem. Ref. Data* **8**, 307-327 (1979)

[61] *EXAFS-Data-Base-(Standards)* **www.nsls.bnl.gov/beamlines/x18b/data.htm**

[62] T. Masujima, H. Kawata, M. Kataoka, H. Shiwaku, H. Yoshida, *Rev. Sci. Instrum* **60**, 2522-2524 (1989)

[63] Zachariasen W. H., Theory of X-Ray diffraction in crystals, Dover Publications, Inc. (1945).

[64] Fingerland A., *Acta Crystall A-Crys* **A27**, 280-284 (1971).

[65] D. Li, Y. Wu, P. Kim, L. Shi, *Appl. Phys. Lett.* **83**, 2934-2936 (2003)

[66] M. Wulff, *Nuclear Instruments and Methods in Physics Research A* **398**, 69-84 (1997)

[67] Bhushan B., Springer Handboof of Nanotechnology, Springer ed. 424-427 (2007)

[68] Hargreaves, C.M.*Phys. Lett. A* **30** , 491-492 (1969)

[69] Polder D., Van Hove M. *Phys. Rev. B* **4**, 3303-3314 (1971).

[70] Rytov, S.M., Kratsov, Yu.A., Tatarskii, V.I. *Principles of statistical Radiophysics*, **vol 3**, Springer-Verlag, New-York, 1987 (Chapter 3).

[71] Lifshitz, E. M. *Zh. Eksp. Teor. Fiz.* **29**, 94 (1955) [Sov. Phys. JETP 2, 73 (1956)]

[72] Xu, J.B., Luger, K., Moller R., Dransfeld, K., Wilson, *J. Appl. Phys.* **76**, 7209-7216 (1994)

[73] Kittel, A., Müller-Hirsch, W., Parisi, J., Biehs, S.A., Reddig, D., Holthaus., M. *Phys. Rev. Lett.* **95**, 224301 (2005)

[74] Wischnath, U. F. , Welker, J. , Munzel, M., Kittel, A. *Rev. Sci. Instrum.* **79**, 073708 (2008).

[75] Mulet, J.-P. Modelisation du rayonement thermique par une approche électromagnetique. Rôle des ondes de surface dans le tranfert d'énergie aux courtes echelles et dans les forces de Casimir. PhD Thesis (2003)

[76] Joulain, K., Mulet, J.-P., Marquier, F., Carminati, R., Greffet, J.-J. *Surf. Sci. Rep.* **57**, 59-112 (2005)

[77] Mulet, J.P., Joulain, K., Carminati, R., Greffet, J.J. *Microscale Thermophysical Engineering* **6**, 209-222 (2002).

[78] Volokitin, A.I., Persson, B.N.J. *Rev. Mod. Phys.* **79**, 1291-1329 (2007).

[79] Mulet, J.P., Joulain, K., Carminati, R., Greffet, J.J. *Appl. Phys. Lett.* **78**, 2931-2933 (2001).

[80] Henkel, C., Joulain, K., Carminati, R., Greffet, J.J. *Opt. Commun.* **186**, 57-67 (2000).

[81] Lai, J., Perazzo, T., Shi, Z., Majumdar, A. *Sensors & Actuators: A. Physical* **58**, 113-119 (1997).

[82] Barnes, J. R., Stephenson, R. J., Woodburn, C. N., Shea, S. J. O., Welland, M.E., Rayment, T., Gimzewski, J. K., Gerber, Ch. *Rev. Sci. Instrum.* **65**, 3793-3796 (1994).
Erratum: *Rev. Sci. Instrum.* **66**, 3083 (1994).

[83] Biehs, S.A. *The European Physical Journal B* **58**, 423-431 (2007)

[84] Chapuis, P.O., Volz, S., Henkel, C., Joulain, K., Greffet, J.J. *Phys.Rev. B* **77**, 035431 (2008)

[85] V. V. Nesvizhevsky, H. G. Boerner, A. K. Petukhov, H. Abele, S. Baessler, F. J. Ruess, T Stoferle, A. Westphal, A. M. Gagarski, G. A. Petrov and A. V. Strelkov, *Nature*, **415**, 297-300 (2002)

[86] Bressi G., Carugno G., Onofrio R., Ruoso G., *Phys. Rev. Lett.* **88**, 041804 (2002)

Résumé

Les Micro et Nano Electro Mechanical Systems (MEMS et NEMS) font partis des meilleurs candidats pour les mesures d'interactions á l'échelle nanométrique. La résolution en force de l'ordre de l'attonewton a été exploitée avec succès aussi bien pour mesurer le poids de molécules uniques que pour la mesure du spin d'un électron unique.
Les NEMS et les MEMS sont généralement des systèmes fabriqués à partir de composants sub-microniques l'un en face de l'autre. Lorsque leur distance atteint l'échelle sub-micronique, phénoménes généralement négligés, doivent être pris en compte lors d'applications microscopiques. Les interactions mécaniques entre deux surfaces séparées de moins d'un micron sont régies par des forces qui, dans des systèmes macroscopiques, sont souvent négligeables.
Dans ce travail de thèse, nous étudions les forces d'interaction entre surfaces séparées par une distance allant de quelques nanomètres à plusieurs micromètres.
Premièrement nous traiterons du problème des forces hydrodynamiques agissant sur des micro-structures oscillantes en environnement visqueux. Nous montrerons que l'effet d'amortissement d'un fluide confiné dépend de la taille du confinement. Nous étudierons comment cet effet de confinement peut modifier les propriétés de cet oscillateur mécanique.
Dans un second temps nous poserons le problème des forces optiques agissant sur les micro-oscillateurs mécaniques. Par l'utilisation de l'absorption et de la diffraction des faisceaux de rayons X nous verrons que les effets habituellement observés en lumière visible le sont aussi par rayons X. Nous montrerons que les MEMS et potentiellement les NEMS sont des systèmes adéquates pour le développement de nouveaux outils pour les techniques de la lumière Synchrotron. Enfin nous étudierons la radiation thermique entre deux surfaces à une distance micronique et sub-micronique où la contribution des composantes champs proche ne peuvent plus être négligées. Nous présenterons les mesures de radiation thermique entre deux surfaces de verres amenant une comparaison avec la théorie de la radiation thermique basée sur l'électrodynamique stochastique.

Résumé

Micro and Nano Electro Mechanical Systems (MEMS and NEMS) are among the best candidates for the measurement of interactions at the nanoscale. Resolution in force in the range of attonewton has been successfully exploited for the weighting of single molecules or the measurement of the spin of a single electron.
NEMS and MEMS are generally mechanical devices made from submicron components facing each other. When the distance between the components reaches the sub-micron scale, phenomena generally neglected during macroscopic applications have to be taken into account. For example, the interaction mechanisms between the two surfaces moving at sub-micron separations are mediated by forces that, in macroscopic devices, are often irrelevant.
In this thesis work we study interaction forces between surfaces when the the gap separating them is in the range from tens of nanometers up to several micrometers.
First we address the problem of hydrodynamic forces acting on micro-structures oscillating in viscous environment. We show that the effect damping of a confined fluid is depending by the gap size of the confinement cavity. We study how this confinement effect can modify the properties of the mechanical oscillator.
Second we address the problem of optical forces acting on micro mechanical oscillators. Using absorption and diffraction of X-ray beams we will see that effects usually observed using visible light can also be observed using X-rays. We show that Micro and possibly Nano Electro Mechanical System can be suitable for developing new tools in the domain of Synchrotron light techniques.
Finally we study the thermal radiation between surfaces when the gap is the micron and sub-micron scale where the contribution of near field components cannot be neglected. We show measurement of thermal radiation between surfaces of glass providing a comparison with the theory of thermal radiation based on stochastic electrodynamics.